University of California
Santa Barbara

Ab Initio Statistical Mechanics of Halide Perovskites

A dissertation submitted in partial satisfaction
of the requirements for the degree

Doctor of Philosophy
in
Materials

by

Jonathon Scott Bechtel

Committee in charge:

Professor Anton Van der Ven, Co-Chair
Professor Ram Seshadri, Co-Chair
Professor Michael Chabinyc
Professor Samantha Daly

March 2019

The dissertation of Jonathon Scott Bechtel is approved.

Professor Michael Chabinyc

Professor Samantha Daly

Professor Ram Seshadri, Committee Co-Chair

Professor Anton Van der Ven, Committee Co-Chair

December 2018

Ab Initio Statistical Mechanics of Halide Perovskites

by

Jonathon Scott Bechtel

Acknowledgements

The work in this dissertation would not have been possible without many scientific collaborations and support from my friends and family. In particular, I thank my advisor Prof. Anton Van der Ven for encouraging me to tackle hard problems and for teaching me to appreciate the beauty of thermodynamics. Also, I thank my co-advisor Prof. Ram Seshadri for emphasizing the importance of well-designed figures and presentations. I also thank Dr. John Thomas who is an unparalleled resource on any mathematical aspect of materials science. I thank all of the graduate students and post-docs of the Van der Ven and Seshadri groups for many stimulating discussions.

I also thank my friends in graduate school who were as quick to support me through stressful times as they were to celebrate the good times. I thank my Mom and Dad for their unwavering support, and I thank Dr. Charlotte Mason whose love and encouragement contributed immeasurably to the completion of this dissertation.

Lastly, I gratefully acknowledge funding from National Science Foundation Grant DMR-1410242 and Grant OAC-1642433, as well as computational resources provided by the National Energy Research Scientific Computing Center (NERSC), supported by the Office of Science and U.S. Department of Energy, under Contract DE-AC02-05CH11231, in addition to support from the Center for Scientific Computing from the CNSI, MRL: an NSF MRSEC (DMR-1720256).

Curriculum Vitæ

Jonathon Scott Bechtel

EDUCATION

University of California, Santa Barbara September 2013 – December 2018
Ph.D. Materials

University of Pittsburgh August 2009 – May 2013
B.Sc. Applied Mathematics and Chemistry
Summa cum Laude

RESEARCH

University of California, Santa Barbara September 2013 – December 2018
Graduate Student Researcher
Van der Ven Group

University of Pittsburgh September 2012 – May 2013
Undergraduate Researcher
Hutchison Group

University of Connecticut June 2012 – August 2012
Research Experience for Undergraduates
Agrios Group

CONFERENCES

2. APS March Meeting, Los Angeles, CA, March 2018
   "Coupling between Octahedral Tilting, A-site Displacements, and Strain in Inorganic Halide Perovskites"
1. APS March Meeting, New Orleans, LA, March 2017
   "Effective Hamiltonians to Describe Octahedral Tilt Instabilities in Halide Perovskites"

FIRST AUTHOR PUBLICATIONS

5. Bechtel, J. S., Thomas, J. C. and Van der Ven, A. (2018, in preparation). Machine-learning parameterization of a vibrational Hamiltonian for octahedral tilting transitions in halide perovskites.
4. Bechtel, J. S., Natarajan, A. R., Thomas, J. C. and Van der Ven, A. (2018, in preparation). Machine-learning the potential energy landscape of halide perovskites.
3. Bechtel, J. S., and Van der Ven, A. (2018). First-principles thermodynamics study of phase stability in inorganic halide perovskite solid solutions. Physical Review Materials, 2(4)

2. Bechtel, J. S., and Van der Ven, A. (2018). Octahedral tilting instabilities in inorganic halide perovskites. Physical Review Materials, 2(2).

1. Bechtel, J. S., Seshadri, R. and Van der Ven, A. (2016). Energy landscape of molecular motion in cubic methylammonium lead iodide from first-principles. The Journal of Physical Chemistry C, 120(23).

CONTRIBUTING AUTHOR PUBLICATIONS

5. Thomas, J. C., Bechtel, J. S., and Van der Ven, A. (2018). Hamiltonians and order parameters for crystals of orientable molecules. Physical Review B, 98(2).

4. Fabini, D. H., Labram, J. G., Lehner, A. J., Bechtel, J. S., Evans, H. A., Van der Ven, A., Wudl, F., Chabinyc, M. L., and Seshadri, R. (2016). Main-Group Halide Semiconductors Derived from Perovskite: Distinguishing Chemical, Structural, and Electronic Aspects. Inorganic Chemistry, 56(1).

3. Fabini, D. H., Laurita, G., Bechtel, J. S., Stoumpos, C. C., Evans, H. A., Kontos, A. G., Raptis, Y. S., Falaras, P., Van der Ven, A., Kanatzidis, M.G., and Seshadri, R. (2016). Dynamic Stereochemical Activity of the Sn2+ Lone Pair in Perovskite CsSnBr3. Journal of the American Chemical Society, 138(36).

2. Kanal, I. Y., Bechtel, J. S., and Hutchison, G. R. (2014). Sequence Matters: Determining the Sequence Effect of Electronic Structure Properties in π-Conjugated Polymers. In Sequence-Controlled Polymers: Synthesis, Self-Assembly, and Properties (pp. 379-393). American Chemical Society.

1. Kanal, I. Y., Owens, S. G., Bechtel, J. S., and Hutchison, G. R. (2013). Efficient computational screening of organic polymer photovoltaics. The Journal of Physical Chemistry Letters, 4(10).

Abstract

Ab Initio Statistical Mechanics of Halide Perovskites

by

Jonathon Scott Bechtel

Halide perovskite materials have emerged as a potentially disruptive technology in the field of photovoltaics with devices exceeding 20% power conversion efficiencies. Crystallizing in the ABX_3 perovskite structure, these materials incorporate main-group cations (Pb^{2+}, Sn^{2+}, Ge^{2+}) on the B-site, halide anions (Br^-, Cl^-, I^-) on the X-site and large monovalent cations (Cs^+, $CH_3NH_3{}^3$, and other organic molecules) on the A-site. Record-breaking materials are achieved by tuning the band gap through halide substitution on the X-site and by increasing structural stability through the use of mixtures of organic cations and inorganic alkali metals on the A-site. In addition to configurational degrees of freedom associated with different alloying strategies, vibrational contributions to the free energy play a large role in the phase evolution of these materials and result in structural phase transitions due to octahedral tilting of the metal-halide sublattice. The phase evolution can be further complicated by the presence of order-disorder transitions due to orientational degrees of freedom of the molecular A-cations. Anharmonic dynamic fluctuations on all three sublattices give rise to a highly polarizable and deformable lattice which plays a role in the remarkable optoelectronic properties observed in halide perovskites.

In this thesis we examine the role of orientational, vibrational, and configurational degrees of freedom in the phase evolution of halide perovskite materials using first-principles electronic structure calculations. In particular, density functional theory calculations reveal anisotropic molecular motion in hybrid perovskite $CH_3NH_3PbI_3$ as well as a highly

anharmonic energy landscape due to octahedral tilting displacement modes across all inorganic halide perovskites.

To link first principles calculations to finite-temperature thermodynamics we make use of cluster expansion effective Hamiltonians applied to both configurational and vibrational degrees of freedom in conjunction with Monte Carlo simulations. In particular, we predict temperature-composition phase diagrams for halide substitution in six Cs-based perovskite binary alloy systems where solid solutions are suppressed by the size-mismatch of end-members. Additionally, we employ machine learning methods to parameterize an anharmonic vibrational cluster expansion enabling both ab initio prediction of finite temperature phase transitions as well as a unique opportunity to investigate local structure at high temperatures from first principles.

Contents

Chapter 1

Introduction

1.1 Motivation

Since their first use in a photovoltaic device in 2009 [1], halide perovskite materials have rapidly emerged as a promising material system for not only light harvesting, but also as active materials in LEDs and other optoelectronic devices. The intense focus on this class of materials from the scientific community has led to thousands of publications over the past decade, and has pushed device efficiencies from around 3% in 2009 [1] to over 22% certified power conversion efficiency demonstrated in 2017. [2] In contrast to conventional semiconducting materials for PV such as Si and IV-VI materials, halide perovskites achieve remarkable optoelectronic properties without the need for energy-intensive manufacturing processes. In fact, part of the reason for the current "renaissance" in halide perovskite material research owes to the ease of preparation: solution-based methods allow facile growth of halide perovskite crystals. Typically, low-temperature, solution-based processes hinder the electronic performance of materials due to the introduction of defects into the crystal structure; however, halide perovskites are known to be exceptionally defect-tolerant. [3, 4] Additionally, halide perovskites show

the best aspects of direct-gap semiconductors, such as high absorption coefficients, but also those of indirect-gap materials, such as long carrier diffusion and low recombination rates. [5, 6, 7, 8, 9, 10, 11, 12, 13, 14, 6] The unexpectedly long carrier diffusion lengths have been shown to derive from Rashba-Dresselhaus type splittings of the conduction band, [15, 16, 17, 18, 15, 19, 20] leading to slightly indirect band-gap character, and also to the formation of large polarons which describe lattice phonon-electron coupling thought to screen free carriers from recombination events. [21, 22, 12]

Central to understanding the properties of halide perovskite system is to understand how the different microscopic degrees of freedom give rise to functional aspects of the materials. For example, the record-breaking halide perovskite materials involve complicated alloying strategies with general compositions of $(MA/FA/Cs/Rb)Pb(Br/Cl)_3$ indicating mixtures of methylammonium, formamidinium, Cs, and Rubidium ions on the A-site, and mixtures of bromine and chlorine on the halide site. Alloying on the A-site with differently sized cations is a way to tune the average, effective A-site cation size which has been shown to stabilize the perovskite structure with respect to decomposition to photo-inactive phases. [23, 24, 25, 26, 27] Substitution on the halide X-sublattice, on the other hand, gives rise to a tunable band gap. [28, 29, 30, 31] In addition to degrees of freedom associated with chemical substitution, molecular rotations and atomic displacements play a large role in dictating halide perovskite properties. For instance, the polar methylammonium ion, $CH_3NH_3^+$, undergoes order-disorder transitions within the inorganic cage [32, 33, 21, 34, 35], which has important consequences on the dielectric properties of the material. [36, 37, 38, 39, 40, 41, 42] Lastly, both hybrid and all-inorganic halide perovskites undergo structural phase transitions associated with octahedral tilting as a function of temperature. [43, 44, 45, 42, 46, 47, 48, 49, 50] In fact, the technologically useful phases at room temperature, either the tetragonal or cubic phases, are dynamically unstable, meaning symmetry-lowering distortions will occur spontaneously

as the temperature is reduced. The anharmonic lattice dynamics that give rise to structural phase transitions in these materials are also partly responsible for many of the important electronic properties such as polaron formation [21, 22, 12] and splitting of the conduction band due to local symmetry breaking. [15, 16, 17, 18, 15, 19, 20] The central tasks of this dissertation are to survey the important microscopic degrees of freedom in halide perovskites, to understand their contributions the energy using first-principles calculations, and to link first-principles results to finite temperature properties through statistical mechanics and an appropriate effective Hamiltonian.

1.2 Organization and Contents

First, Chapter 2 reviews the computational methods used in this dissertation. After a discussion of electronic structure calculations and density functional theory, the cluster expansion formalism is discussed in the context of its applications for alloys, molecular crystals, and anharmonic vibrational effective Hamiltonians. Methods for solving the linear regression problem for finding fitting coefficients to cluster expansion are covered as well as application of artificial neural networks to regression problems. Lastly, the Monte Carlo method is reviewed as it pertains to computing thermodynamic averages as a function of temperature and chemical potential.

In Chapter 3, the energy landscape with respect molecular orientation is investigated with density functional theory calculations (DFT), and a strong preference for the crystallographic [100] direction in the cubic unit cell is found. In addition, molecular translations are shown to play the largest role with respect to orientational preference indicating that hydrogen bonding between NH_3 hydrogen atoms and the iodine sublattice dictates the interactions between the molecule and inorganic host.

Chapter 4 focuses on the atomic displacement and strain degrees of freedom that

describe structural phase transitions in inorganic halide perovskites. Primary displacement order parameters are defined in terms of octahedral tilt modes for $CsSnBr_3$, $CsSn_3$, $CsPbBr_3$, and $CsPbI_3$. Geometric optimization by DFT for all 14 symmetry lowering tilt modes reveals that the stability of a particular tilt system corresponds to its ability to reduce the unit cell volume. Additionally, A-site displacements are shown to be crucial to stabilizing the ground state Pnma structure, again pointing to the importance of A-site translations.

Chapter 5 explores chemical substitution degrees of freedom where phase stability with respect to halide (X-site) alloying is investigated using the cluster expansion approach. Phase diagrams of six halide binaries including $CsSn(Br_xCl_y)_3$, $CsSn(Br_xI_y)_3$, $CsSn(Cl_xI_y)_3$, $CsPb(Br_xCl_y)_3$, $CsPb(Br_xI_y)_3$, and $CsPb(Cl_xI_y)_3$, are constructed by first fitting a cluster expansion Hamiltonian to DFT calculations of halide orderings in the ground state Pnma phase, and using the resulting model in semi-grand canonical Monte Carlo simulations. Interestingly, the temperature at which the solid solution becomes stable correlates with the volume difference between end members. The results provide a convenient design principle: to encourage solid solutions at low temperatures, choose end members which have similar unit cell volumes.

An efficient parameterization of the DFT potential energy surface is sought in Chapter 6 where we generalize the notion of the anharmonic vibrational cluster expansion using artificial neural network model architectures. In this way we are able to parameterize the DFT energy landscape with respect to atomic displacements for $CsPbBr_3$. Cluster-based and site-based models are explored and a detailed exploration of hyperparameter tuning shows that models utilizing high-order basis function tend to extrapolate poorly. On the other hand, we find that second order (harmonic) basis functions used in the cluster-based neural net models are able to reproduce the highly anharmonic perovskite energy landscape due to the non-linear activation functions.

In Chapter 7, we introduce a conceptually simple vibrational effective Hamiltonian for perovskite systems that includes only four pair interactions as well as an octahedral cluster. The model is parameterized using machine-learning neural net models, and finite-temperature Monte Carlo simulations are used to investigate structural phase transitions. Remarkably, these simple models reproduce qualitatively the phase transition sequence observed in inorganic halide perovskites. Moreover, the fitting procedure sheds light on the pair interactions in halide perovskites and reveals how the under-coordination of the A-site leads to subtle changes in the CsBr energy landscape in accordance with traditional tolerance factor intuition. These results lead to the first ab initio statistical mechanics study of inorganic halide perovskites that qualitatively reproduces the tilt transition sequence as well as the local fluctuations of atoms as confirmed through analysis of atomic anisotropic displacement parameters and distributions of octahedral rotations.

Chapter 2

Background and Computational Methods

The cluster expansion method has proven to be a useful tool, especially in the alloy community, to link first principles electronic structure calculations to finite temperature materials properties through statistical mechanics. A large portion of this dissertation makes use of the cluster expansion method to define a suitable effective Hamiltonian which allows the calculation of phase diagrams through finite temperature statistical mechanics. The procedure first involves identifying a microscopic degree of freedom suitable for the problem at hand. For instance, predicting a temperature-composition phase diagram involves tracking the identity of atom on every crystallographic site using discrete site variables. More recently, the cluster expansion formalism has been extended for continuous degrees of freedom such as molecular rotations, magnetic spins, and atomic displacements. In any case, the cluster expansion allows one to define an appropriate set of basis functions in terms of a microscopic degree of freedom used to model a crystal property such as the formation energy. First-principles calculations are performed to build a database of training data which include the crystallographic information and the

formation energy. The raw cystallographic information is encoded as a feature vector by means of the symmetry-invariant basis functions. Linear regression or other machine learning methods can be used to find the fitting coefficients which parameterize the cluster expansion effective Hamiltonian. Statistical mechanics then associates this effective Hamiltonian with a probability distribution over all microstates, which, in principle, allows for the calculation of the materials properties at any temperature. However, the normalizing factor to the thermodynamic probability distribution, i.e. the partition function, is unknown due to the high dimensionality of the phase space. Therefore, Monte Carlo simulations must be used to draw samples from the distribution, which in turn provides a way to calculate thermodynamic averages allowing for ab initio predictions of finite-temperature materials properties.

This section walks through each step of the ab initio statistical mechanics approach. First the foundations of modern electronic structure calculations are discussed and how density functional theory allows approximate solutions to the many-body Schrodinger equation. An overview of effective Hamiltonians and cluster expansion methods shows how symmetry invariant basis function can be constructed for different types of microscopic degrees of freedom. The procedure for fitting model parameters is discussed in the context of the traditional linear cluster expansion as well as machine-learning models. Finally, the connection between the effective Hamiltonian and finite-temperature properties is madethrough the use of statistical mechanics and Monte Carlo simulations.

2.1 Electronic Structure Calculations

The behavior of a quantum system comprised of electrons and ions can be solved via the time-independent Schrodinger equation given by

$$\hat{H}|\Psi\rangle = E|\Psi\rangle \tag{2.1}$$

where $\hat{H}$ is the Hamiltonian which encodes all interactions among and between electrons and nuclei, $|\Psi\rangle$ is the many-body wavefunction, and E is the total energy. Given the different time scales of atomic and electronic motion, the Born-Oppenheimer approximation allows for the decoupling of the nuclear and electronic wavefunctions, since electrons are assumed to instantaneously adjust to a shift in atomic coordinates. This leads to the electronic part of the Schrodinger equation below written in Hartree atomic units ($\hbar = m_e = e = 4\pi/\epsilon_0 = 1$) as:

$$\hat{H} = T_e + V_{\text{int}} + V_{\text{ext}} \tag{2.2}$$

$$= -\frac{1}{2}\sum_j \nabla_j^2 + \sum_i \sum_{j<i} \frac{1}{|\mathbf{r}_j - \mathbf{r}_i|} - \sum_{i,j} \frac{Z_i}{|\mathbf{r}_j - \mathbf{R}_i|} \tag{2.3}$$

where T_e, V_{int} and V_{ext} are the kinetic energy of the electrons, interactions among electrons, and Coulomb interactions between electrons and ions, respectively. [51] Electron coordinates and nuclear coordinates are denoted $\mathbf{r}$ and $\mathbf{R}$, respectively. This equation with $3N$ electronic degrees of freedom is impractical to solve directly, and a simplification is needed.

2.2 DFT

The seminal contributions of Hohenberg, Kohn, and Sham recast the intractable many-body problem into into a more manageable problem by introducing the electron density as the central quantity. [52] Hohenberg and Kohn proved two essential theorems that laid the framework for density functional theory which stated: (1) the ground state energy is a unique functional of the ground state electron density, and (2) that the ground state electron density is the unique density that minimizes the energy. By working with the electron density $n(\mathbf{r})$ which depends only on 3 spatial coordinates, we circumvent finding the $3N$ many-body wavefunction. Further, Hohenberg and Kohn showed that the many-body Schrodinger equation can be recast in terms of energy functionals as

$$E_{\mathrm{HK}}[n] = T[n] + E_{ee}[n] + \int d\mathbf{r} V_{\mathrm{ext}}(\mathbf{r}) n(\mathbf{r}) \tag{2.4}$$

where $E_{\mathrm{ext}} = \int V(\mathbf{r}) n(\mathbf{r}) d\mathbf{r}$.

The Kohn-Sham approach [53] to solving for the ground state electron density is to first solve an auxiliary independent-particle system with "orbital" wavefunction solutions ψ_i that reproduce the solution to the many-body problem whose ground state electron density is given as

$$n = \sum_i |\psi_i|^2 \tag{2.5}$$

The Kohn-Sham energy functional takes the form:

$$E_{\mathrm{KS}}[n] \ = T_S[n(\mathbf{r})] + E_H[n] + \int d\mathbf{r} V_{ext}(\mathbf{r}) n(\mathbf{r}) + E_{XC}[n] \tag{2.6}$$

The difference between the Hohenberg-Kohn functional and the Kohn-Sham functional is the expression for the combined kinetic and interaction energies of the electrons:$F =$

$T + E_{\text{int}}$. Kohn and Sham sought a way to express F exactly in terms of the electron density. First, one contribution to the kinetic energy that can be explicitly written out is the kinetic energy for a system of non-interacting electrons of density n given as T_S. Furthermore a part of the electron-electron interaction due to the classical Coulomb interaction, known as the Hartree term, can be written as

$$E_H[n] = \frac{1}{2} \int \int \frac{n(\mathbf{r})n(\mathbf{r}')}{|\mathbf{r} - \mathbf{r}'|} d\mathbf{r} d\mathbf{r}' \tag{2.7}$$

The difference between the real kinetic Energy and the kinetic energy of the non-interacting system, as well as the difference between the electron-electron interaction and the classical Coulomb interaction are all rolled into a single term known as the exchange-correlation functional:

$$E_{XC}[n] = T[n] - T_S[n] + E_{ee}[n] - E_H[n] \tag{2.8}$$

Hence, the exchange correlation functional incorporates all of the approximations to the electron kinetic energy and interaction terms. If the exchange-correlation functional was known, then the solution for the ground state electron density would be exact by solving the Kohn-Sham equations for independent particles. By variationally minimizing the energy functional $E_{\text{KS}}[n]$, Kohn and Sham arrived at the self-consistent Kohn-Sham equations:

$$H_{\text{KS}}\psi_i(\mathbf{r}) = \varepsilon_i \psi_i(\mathbf{r}) \tag{2.9}$$

where

$$H_{\mathrm{KS}}(\mathbf{r}) = -\frac{1}{2}\nabla^2 + V_{\mathrm{eff}}(\mathbf{r}) \tag{2.10}$$

$$V_{\mathrm{eff}}(\mathbf{r}) = V_{\mathrm{ext}}(\mathbf{r}) + \frac{\delta E_{\mathrm{H}}}{\delta n(\mathbf{r})} + \frac{\delta E_{\mathrm{XC}}}{\delta n(\mathbf{r})} \tag{2.11}$$

$$= V_{\mathrm{ext}}(\mathbf{r}) + V_{\mathrm{H}}(\mathbf{r}) + V_{\mathrm{XC}}(\mathbf{r}) \tag{2.12}$$

$$= -\sum_j \frac{Z_j}{|\mathbf{r}_j - \mathbf{r}|} + \int d\mathbf{r}' \frac{n(\mathbf{r}')}{|\mathbf{r} - \mathbf{r}'|} + V_{\mathrm{XC}}(\mathbf{r}) \tag{2.13}$$

Hence, the only unknown is the exchange-correlation functional. Note that the Hartree term and the XC term both depend on the electron density so this is a self-consistent equation. The general procedure for solving the Kohn-Sham equations involves expanding the single electron wavefunctions in terms of a set of basis functions, typically plane waves in calculations of periodic solids, but Gaussian basis functions are also used in calculation of molecular species. To solve the equations, first a trial wavefunction is supplied, the effective potential is calculated, and the expansion coefficients of the single-electron wavefunctions are calculated along with the energy levels. Given the new expansion coefficients a density can be recalculated and a new energy is found. This procedure is repeated until a converged energy results. The energy levels at each k-point give good approximations to the electronic eigenvalues of the band structure which is accessible from certain experiments.

DFT reduces the intractable problem of n-body interactions between electrons by making several approximations. First, only the outer shell electrons of individual atoms interact with other neighboring atoms giving rise to the use of pseudopotentials which only treat valence electrons explicitly and treat core electrons as a field of electron density. The second approximation is treating not individual electrons but calculating the energy in terms of an electron density throughout a material. The energy can be minimized

self-consistently in a way to find the ground state electron density and this is guaranteed to be the ground state.

2.3 Effective Hamiltonians

While DFT is an exceptional approach to investigate the electronic structure of solids, its computational complexity which scales as the cube of the number of electrons limits its application to relatively small systems on the order of 100s of atoms. Moreover, DFT calculations are performed at 0 K where entropic contributions are neglected. In order to study finite temperature properties of materials, we make use of effective Hamiltonians, which seek to reproduce the results of DFT with more computationally efficient models. The general approach involves first collecting a database of DFT calculations. Invariant features are formed from the structures, whether they be descriptors of the site decorations (configurational cluster expansion), molecular orientations (rigid-rotor cluster expansion), or atomic displacements (anharmonic vibrational cluster expansions). The cluster expansion method involves expanding a scalar or tensor quantity of interest over symmetry invariant basis functions. The coefficients to these terms are referred to as effective cluster interactions (ECI) and are found by minimizing a particular objective function, typically the squared difference between the model energies and the true DFT energies.

In order to calculate finite temperature properties of solids it is necessary to re-parameterize and approximate the DFT energy landscape in terms of a more convenient, computationally less expensive model. One approach that has proven especially convenient and useful is the cluster expansion method whereby a set of crystal basis functions are constructed with respect to clusters of atoms in a crystal. As will be demonstrated below and in the subsequent chapters, many degrees of freedom can be incorporated

in the cluster expansion formalism, such as occupancy of chemical species on a lattice, atomic displacements, and molecular rotations. Regardless of the microscopic degree of freedom the procedure for constructing the cluster expansion consists of several universal steps. First, a local basis is defined on each site. Then crystal basis functions are constructed by taking the tensor product of all site basis functions. By including the constant basis function, 1, in the site bases, it is possible to distinguish the crystal basis functions according to clusters (i.e. a local neighborhood of a small number of atoms such as a pair, triplet, etc) thereby resulting in the cluster expansion. To fit the expansion coefficients, spatial averages are taken over all symmetric equivalent basis functions giving the correlations. This sets up a linear regression task for which many approaches and algorithms are possible. Below we detail the specific cases of the configurational, vibrational, and rotational cluster expansions with respect to how the site and crystal basis functions are constructed.

2.3.1 Configurational Cluster Expansion

The alloy cluster expansion expands the energy of a solid in terms of basis functions, ϕ, of configuration variables, σ which take on the values $\{0, 1\}$ in the occupation basis or $\{-1, +1\}$ in the spin basis. The configuration variable defines which atomic species resides at the site. For instance, in the occupation basis, $\sigma = 0$ may denote the presence of atom A, while $\sigma = 1$ denotes the presence of atom B. Formally the energy can be

written as [54, 55, 56, 57, 58]:

$$E = \sum_{\alpha} V_{\alpha} \prod_{i \in \alpha} \sigma_i \tag{2.14}$$

$$= \sum_{\alpha} V_{\alpha} \Phi_{\alpha}(\vec{\sigma}) \tag{2.15}$$

$$= \sum_{\alpha'} V_{\alpha'} \sum_{\beta \in \Omega_{\alpha'}} \Phi_{\alpha'}(\vec{\sigma}_{\beta}) \tag{2.16}$$

where α runs over all clusters in the crystal, α' runs over all symmetrically distinct clusters, β indexes each symmetrically equivalent cluster within the orbit of the prototype cluster $\Omega_{\alpha'}$, Φ is a crystal basis function,and $V_{\alpha'}$ is an expansion coefficient known as an effective cluster interaction (ECI). The cluster expansion provides a means to re-parameterize the complicated quantum mechanical interactions onto a classical basis, parameterized by only a few coefficients. The process for fitting a cluster expansion involves enumerating symmetrically distinct configurations, fully relaxing them in DFT to find the ground state energy, and then performing regression in order to minimize an objective function such as a root mean squared error, or a cross validation score. [59, 60, 61, 62, 63]

2.3.2 Anharmonic Vibrational Cluster Expansion

The problem of describing the vibrational free energy of a solid that undergoes structural phase transitions is an extremely difficult problem in computational materials science. The existing methods, such as high-order Taylor expansions, or fitting force constants to ab initio MD simulations have their own drawbacks, including difficult compatibility relations to ensure rotational invariance and high computational cost. An alternative approach of describing all vibrational degrees of freedom in a solid has been developed in our group by Thomas and Van der Ven, and the essential features are

described below. [64]

We want to describe the energy of a crystal with respect to atomic displacements:

$$E = E(\mathbf{R}) \tag{2.17}$$

where E represents the energy of a collection of N atoms and $\mathbf{R}$ is a $3 \times N$ matrix of atomic positions. We will begin with the cluster expansion formalism that posits that the energy can be expressed as a sum of local cluster energies as

$$E = E_0 + \sum_{\alpha} \sum_{n} \sum_{i} V_{(\alpha,n,i)} \Phi_{(\alpha,n,i)}(\vec{q}^{\alpha}) \tag{2.18}$$

where α labels all of the clusters in a crystal n labels the polynomial order of the basis function and i labels individual basis function of order n. V indicate the expansion coefficients and Φ are the crystal basis functions which describe the cluster deformations. A key feature of this description is the use of a symmetry-adapted coordinate system in order to describe local cluster deformations, denoted by q. They are defined in terms of the pair distances within a cluster as

$$q_k = \sum_{l} Q_{kl} f(d_l, d_0) \tag{2.19}$$

where Q is a linear transformation of the vector of functions of pair distances d_l within the cluster. The functor can take several form including the logarithm, linear, functional

or quadratic functional defined as

$$f_{\text{LOG}} = \frac{1}{2} \ln \left[\frac{d_l^2}{d_{l_0}^2} \right] \tag{2.20}$$

$$f_{\text{LIN}} = \left[\frac{d_l^2}{d_{l_0}^2} \right]^{1/2} - 1 \tag{2.21}$$

$$f_{\text{QUAD}} = \frac{1}{2} \left[\frac{d_l^2}{d_{l_0}^2} - 1 \right] \tag{2.22}$$

Hence the amplitudes q define a naturally rotationally and translationally invariant description of the cluster deformation. The q vectors transform as irreducible representations of the cluster point group, but to define the energy of the crystal, we need functions that are invariant to the symmetry operations of the crystal. Crystal basis functions of order n are constructed conceptually via tensors of rank n. For instance first, second, and third order basis functions can be constructed as:

$$\Phi_{n=1} = \sum_i \kappa_i q_i = \kappa^\top \mathbf{q} \tag{2.23}$$

$$\Phi_{n=2} = \sum_{ij} \kappa_{ij} q_i q_j = \mathbf{q}^\top \kappa \mathbf{q} \tag{2.24}$$

$$\Phi_{n=3} = \sum_{ijk} \kappa_{ijk} q_i q_j q_k \tag{2.25}$$

Above second order, we can no longer represent the polynomials as matrix algebra. In general an order n polynomial basis function is defined as

$$\Phi_n = \sum_\eta \kappa_\eta \prod_{\eta_i}^{n} q_{\eta_i} \tag{2.26}$$

where η represents a vector of n indices specifying the index of each of the n different q vectors.

2.3.3 Rotational Cluster Expansion

The investigations into molecular rotations led in part to the development of the rotational cluster expansion which is outlined here. First, local degrees of freedom must be defined for a rotation. Typically, rotation matrices are the most convenient form to parameterize a rotation, however, a key insight is the use of the quaternion parameterization of a rotation which allows for a consistent description of this degree of freedom in line with the natural cluster expansion formalism. This is because the quaternion can be treated as a column vector with its own symmetry representation, therefore all of the tools of linear algebra are available, such as the use of the Reynold's operator and tensor basis for the construction of crystal basis function polynomials. Typically the rotation of a vector proceeds as

$$x' = Rx \tag{2.27}$$

where x are the coordinates of the original vector, x' are the coordinates of the rotated vector, and R is a rotation matrix. It should be noted that, in general, rotations do not commute, which makes dealing with rotations tricky in practice. As an alternative of the rotation matrix we can also describe the rotation of a matrix using quaternion algebra, which can be thought of as an extension of the complex numbers. In this algebra a rotation is accomplished via,

$$[0, x'] = q^*[0, x]q \tag{2.28}$$

Quaternions of unit length offer an alternative parameterization of the space of rotations. As unit vectors on the 3-sphere (S^3) embedded in 4-dimensional Euclidean space, the group of quaternions is isomorphic to $SU(2)$ and they satisfy $||q||^2 = q_0^2+q_1^2+q_2^2+q_3^2 = 1$; therefore quaternions as four component vectors have three degrees of freedom asso-

ciated with the hyperspherical angles $q(\alpha, \theta, \phi)$ which define quaternion components as follows:

$$q_0 = \cos\alpha$$
$$q_1 = \sin\alpha \sin\theta \cos\phi$$
$$q_2 = \sin\alpha \sin\theta \sin\phi$$
$$q_3 = \sin\alpha \cos\theta$$

Alternatively, the quaternion can be expressed in the axis angle form:

$$q = (q_0, \boldsymbol{q}) = [\cos(\omega/2), \hat{\mathbf{n}}(\theta, \phi)\sin(\omega/2)]$$

where $\omega = 2\alpha$ represents the rotation angle, and $\hat{\mathbf{n}}(\theta, \phi)$ represents the axis of rotation.

In the rotation cluster expansion the crystal basis functions are made of products of hyperspherical harmonics which have been pre-symmetrized to the molecular symmetries. The site basis must be made invariant to the symmetries of the molecule which can be accomplished by applying the Reynold's operator with respect to the molecular point group. Furthermore, the crystal symmetries dictate which polynomials formed through a tensor product of the site bases survive when applying the Reynold's operator of the crystal factor group. A full treatment of the rotational cluster expansion can be found in [65].

2.3.4 Fitting the ECI

In a linear cluster expansion, the ECI are in principle attainable due to the orthogonality of basis functions. However, in practice the ECI are found through regression

techniques such as linear regression meant to minimize the squared error between the model and the DFT energies. The correlations for each basis function are calculated by averaging the basis function over all symmetrically equivalent clusters.

$$e = E/N \tag{2.29}$$

$$= \frac{1}{N} \sum_{\alpha} V_{\alpha} \Phi_{\alpha}(\vec{\sigma}) \tag{2.30}$$

$$= \sum_{\alpha'} v_{\alpha'} \langle \Phi_{\alpha'}(\vec{\sigma}_{\beta}) \rangle \tag{2.31}$$

where $v = \frac{V|\Omega_{\alpha'}|}{N}$ is the ECI normalized by the number of unit cells and multiplied by the multiplicity of the cluster α' in the unit cell. The correlations are defined as $\langle \Phi_{\alpha}(\vec{\sigma}_{\beta}) \rangle = \frac{1}{|\Omega_{\alpha'}|} \sum_{\beta \in \Omega_{\alpha'}} \Phi_{\alpha'}(\sigma_{\beta})$, which is the average of the basis function of cluster α' over all equivalent clusters β denoted as the orbit $\Omega_{\alpha'}$. Then the $n \times m$ correlation matrix Φ contains m correlations for n configurations. DFT calculations are performed to find the energy associated with each configuration which makes up the vector e. Finding the set of clusters that should be included can either be done first, followed by linear regression, or all at once, by using a regularized regression function. In this first approach a method of traversing the parameter space is needed, and the genetic algorithm is a particularly useful approach. [66] The linear regression problem is to find the expansion coefficients v in

$$\boldsymbol{\Phi v} = \boldsymbol{e} \tag{2.32}$$

which minimize an objective function of the form:

$$\Gamma = ||\mathbf{e} - \boldsymbol{\Phi v}||_2^2 + ||\boldsymbol{\Lambda} \mathbf{v}||_1 + ||\boldsymbol{\Pi} \mathbf{v}||_2^2 \tag{2.33}$$

where $||\cdot||_1$ refers to the l_1 norm and $||\cdot||_2$ refers to the Euclidean, or l_2 norm. The terms scaled by weight matrices $\mathbf{\Lambda}$ and $\mathbf{\Pi}$ are known as regularization terms, and larger values in $\mathbf{\Lambda}$, LASSO [67, 68], penalizes the number of nonzero ECI, while $\mathbf{\Pi}$ penalizes the size of the ECI, where a larger $\mathbf{\Pi}$ will shrink ECI closer to zero.

2.4 Finite Temperature Thermodynamics

We are interested in the equilibrium properties of materials which are described by classical thermodynamics and are connected to the microscopic behavior of materials through statistical mechanics. Due to the immense number of microscopic degrees of freedom that make up a solid, including atomic displacements, magnetic moments, strain, atomic species, and more, we must work with distributions over these degrees of freedom. Probability theory tells us that the expectation value of a certain quantity is related to the probability distribution over that value as:

$$\langle y \rangle = \int d\boldsymbol{\sigma} \mathcal{P}(\boldsymbol{\sigma}) y(\boldsymbol{\sigma}) \tag{2.34}$$

Here $\boldsymbol{\sigma}$ defines a microstate of the system, $\mathcal{P}(\boldsymbol{\sigma})$ is the probability of being in that microstate and $y(\boldsymbol{\sigma})$ is the value of the observed quantity. For discrete microstates, such as configurations of atomic species on the lattice, the integral is replaced by a sum. However, for continuous degrees of freedom such as atomic displacements or spins a $3N$-dimensional integral is required over all states. For all but the simplest cases this sum or integral over all of phase space is computationally intractable.

2.4.1 Canonical Ensemble

The form of $\mathcal{P}$ is given by statistical mechanics and it is the distribution that maximizes the entropy. Depending on which variables are held constant the form of $\mathcal{P}$ changes slightly but the starting point is the canonical distribution in which the temperature is held constant and all other intensive variables are allowed to take on the values that minimize the free energy. In this case

$$\mathcal{P} = \frac{1}{\mathcal{Z}} \exp\left[-\beta E(\boldsymbol{\sigma})\right] \tag{2.35}$$

$$\mathcal{Z} = \int d\boldsymbol{\sigma} \exp\left[-\beta E(\boldsymbol{\sigma})\right] \tag{2.36}$$

where $\mathcal{Z}$ is the canonical partition function. This allows us to define the Helmholtz free energy:

$$A = \langle E \rangle - TS \tag{2.37}$$

$$= -k_B T \ln\left[\mathcal{Z}\right] \tag{2.38}$$

2.4.2 Grand Canonical

In the grand canonical ensemble both the chemical potential and temperature are held fixed resulting in the thermodynamic probability distribution:

$$\mathcal{P} = \frac{1}{\mathcal{Z}} \exp\left[-\beta \left(E(\boldsymbol{\sigma}) + \mu x\right)\right] \tag{2.39}$$

$$\mathcal{Z} = \int d\boldsymbol{\sigma} \exp\left[-\beta \left(E(\boldsymbol{\sigma}) + \mu x\right)\right] \tag{2.40}$$

where $\mathcal{Z}$ is the grand canonical partition function. This results in the Grand Canonical Free Energy:

$$\Phi = \langle E \rangle - \mu \langle x \rangle - TS \tag{2.41}$$

$$= -k_B T \ln(\mathcal{Z}) \tag{2.42}$$

2.4.3 Monte Carlo

In ab initio statistical mechanics thermodynamic properties are calculated via Markov Chain Monte Carlo (or simply Monte Carlo) simulations. The idea is to generate samples of states from the probability density function for which we don't know the normalization factor, i.e. the partition function. In the Metropolis-Hastings algorithm [69, 70], within a lattice model, individual sites are perturbed and the move is accepted with a certain transition probability. If the energy of the system decreases, the move is always accepted. However, for a move where the energy remains the same or increases, the move is accepted with probability proportional to the Boltzmann factor. Transition probabilities for accepting a proposed step are:

$$p_{i \to f} = \min\left(1, \exp\left[-\beta \Delta E\right]\right) \tag{2.43}$$

where ΔE refers to the difference between the proposed state and the current state. Using this acceptance probability, proposals which decrease the energy are always accepted ($p_{i \to f} = 1$) and moves that increase the energy are accepted with probability ($p = \exp\left[-\beta \Delta E\right]$). Due to the temperature dependence of the Boltzmann factor, unfavorable moves are more likely to be accepted at higher temperatures, which aligns with our intuition of a thermally fluctuating system. Using the Metropolis algorithm guarantees that the visited chain of states approaches the thermodynamic distribution defined by our

Hamiltonian. The massive appeal to Monte Carlo simulations is that we draw samples from $\mathcal{P}$ without having to explicitly know how to calculate $\mathcal{Z}$. When this technique is used the intractable problem of calculating thermodynamic averages simplifies to taking arithmetic means of the quantities of interest. That is, the thermodynamic average

$$\langle X \rangle = \int X(\sigma)\mathcal{P}(\sigma)d\sigma \tag{2.44}$$

is calculated simply as

$$\langle X \rangle = \frac{1}{N}\sum_{i}^{N} X_i \tag{2.45}$$

where X are the values determined at each Monte Carlo step.

2.5 Machine Learning

In addition to linear models such as cluster expansions, numerous machine learning methods have been utilized by the computational materials science community in order to reproduce the high-dimensional DFT energy landscape. [71, 72, 73, 74, 75] In this dissertation, we have explored the use of artificial neural nets as an alternative model for anharmonic cluster expansion Hamiltonians. Artificial neural networks (ANNs) can be thought of as a non-linear generalization of a linear model. ANNs have been shown to perform regression and classification tasks with state-of-the-art accuracy. The high accuracy/low training error achievable with ANNs is due in part to the high number of fitting coefficients (analogous to the cluster expansion ECI) within each model. Due to the large number of fitting coefficients, very large training databases are necessary in order to train accurate, generalizable models. In this dissertation an ANN was trained on over 30,000 DFT configurations in order to model the DFT energy landscape with

respect to atomic displacements. The functional form of a two-layer neural net can be written

$$\mathcal{N} = \sum_l V_l^{(3)} f_l^{(2)} \left(\sum_k f_k^{(1)} \left(\sum_i x_i^{(0)} V_{ij}^{(1)} + b_j^{(1)} \right) V_{kl}^{(2)} + b_l^{(2)} \right) + b^{(3)} \tag{2.46}$$

where x is the input feature vector, which is composed of polynomial basis functions as described in Chapter 6, f are the activation functions and can take several functional forms such as rectified linear unit, sigmoid or hyperbolic tangent. The fitting parameters are the weights of the connection between nodes V and the biases b. Efficient ways of determining the optimal weights is an intense area of research, and we make use of state of the art tools provided by open source libraries, specifically Tensorflow Python API. Training neural nets can be achieved by standard gradient descent algorithms which find the gradient of the objective function, Γ, defined as

$$\Gamma = \sum_i (\mathcal{N}(\sigma_i, V, b) - E_{\mathrm{DFT}})^2 \tag{2.47}$$

where $\mathcal{N}(\sigma_i, V, b)$ represents the neural net approximation to the energy for configuration σ_i. Given the objective function, the problem turns into the optimization problem of finding the weights and biases of the model $\mathcal{N}$ which minimize Γ. While no method can guarantee to find the global minimum of the objective function, efficient gradient descent related algorithms are able to locate local minima that reproduce the DFT training energies with high accuracy. A drawback of the ANN models is that it is potentially very easy to overfit the training data; therefore, cross-validation schemes must be used in order to validate the model's performance in an unbiased way. Chapter 6 details the construction, training, and validation of ANNs applied to fitting the DFT energy landscape of $CsPbBr_3$.

Chapter 3

Energy Landscape of Molecular Motion in Cubic Methylammonium Lead Iodide from First Principles

3.1 Introduction

Hybrid organic-inorganic perovskite materials for photovoltaics present a promising avenue toward efficient, inexpensive solar energy conversion. [77] Reaching power conversion efficiencies of nearly 20%, the record-setting perovskites consist of a Pb−I octahedral framework with methylammonium cations ($CH_3NH_3^+$) occupying the *A*-site. [78, 79, 80] Long electron-hole diffusion lengths [81, 82], high absorption coefficients [1, 83], and a 1.6 eV band gap [84, 1] contribute to the remarkable photovoltaic properties of this material.

Establishing structure-property relationships in $CH_3NH_3PbI_3$ has proven challenging due to important entropic contributions arising from PbI_6 octahedral tilting and $CH_3NH_3^+$ rotational degrees of freedom. At elevated temperature, the PbI_6 octahedra of the inorganic host undergo large tilt-mode oscillations relative to their average positions in the ideal cubic structure, [85] while the molecular cations rotate rapidly. [32, 34] Distortions of the inorganic lattice by halide substitution and octahedral tilting have been shown to influence the band gap and absorption properties. [86, 1, 87, 88] Although the A-cation does not contribute to electronic states near the band gap, [89, 90, 4] it has been shown to affect the nature of the band gap through interaction with the inorganic Pb−I sublattice. [17] Moreover, the dielectric properties of $CH_3NH_3PbI_3$ are linked to both the rotational dynamics and ordering of the molecular A-cation and the structural phase transitions of the inorganic Pb−I lattice. [32, 35, 42, 91, 92]

$CH_3NH_3PbI_3$ undergoes a transition from the high-temperature pseudo-cubic aristotype $Pm\bar{3}m$ structure to the tetragonal $I4/mcm$ phase ($a^0a^0c^-$ tilt system in Glazer notation) [93] at 330 K and then to the orthorhombic $Pnma$ phase ($a^+b^-c^-$ tilt system) below 160 K. [94, 95, 43, 96] The transitions associated with A-cation ordering have been the subject of some debate. [35, 97, 34, 32, 86, 98, 99] Nevertheless, recent quasi-elastic neutron scattering experiments indicate that the $CH_3NH_3^+$ molecules in the cubic phase dynamically disorder and undergo both fast reorientations of the C−N bond axis (≈5 ps at 300 K) and faster on-axis rotations about the C−N bond axis (≈1 ps at 300 K). [32] Some degrees of freedom freeze out upon cooling and only on-axis rotations are observed in the low temperature orthorhombic phase (≈4 ns at 70 K) accompanied by a dramatic loss in dielectric permittivity. [32]

Several studies have employed first-principles calculations to reveal the microscopic origins of preferential $CH_3NH_3^+$ orientations and the interactions between $CH_3NH_3^+$ and the inorganic Pb−I host lattice. [100, 101, 102, 103] In the orthorhombic phase, energy

barriers of ≈100 meV were calculated for on-axis rotations of the staggered configuration of $CH_3NH_3^+$ due to strong N−H···I interactions, suggesting fully ordered *A*-cations in the low temperature phase. [100] Recently, $CH_3NH_3^+$ rotations were investigated in the tetragonal phase, and energy barriers of ≈50 and ≈20 meV for on-axis rotation were found depending on the molecular orientation. [101] Low energy pseudo-cubic $Pm\bar{3}m$ configurations have previously been identified with molecular orientations in the [100], [110], and [111] directions. [102, 103] While past studies have explored the energy of the crystal for a subset of orientations and on-axis rotational degrees of freedom, an understanding of the interactions of the *A*-cation with the inorganic Pb−I sublattice as a function of all its rotational and translational degrees of freedom remains incomplete.

In this letter, we map out the full energy landscape of $CH_3NH_3^+$ motion in the cubic inorganic host by accounting for all reorientations of the C−N bond axis, all on-axis rotations about the bond axis, and translations of the molecule from the ideal *A*-site. While the orthorhombic phase is characterized by ordered $CH_3NH_3^+$ orientations in a rigid host lattice, large anharmonic vibrational excitations associated with octahedral tilting and disordered molecular orientations and translations add considerable structural complexity to the high-temperature cubic phase. Here we focus on the ideal cubic perovskite structure in order to investigate the microscopic details of N−H interactions with the Pb−I host lattice. By maintaining a rigid inorganic lattice, we separate the effects of octahedral tilting and molecular rotation. This allows us to quantify the energy associated only with the rigid rotations of the methylammonium molecule and its interactions with the inorganic lattice. We find that the energy of the crystal is especially sensitive to molecular translations which lead to a stabilization of the [100] orientation as a result of favorable N−H···I interactions. The energy barriers to reorientation approach 100 meV when translations are considered, while barriers to on-axis rotations range from 200 meV in the [111] orientation to <10 meV in the [110] and [100] orientations. Finally, we show

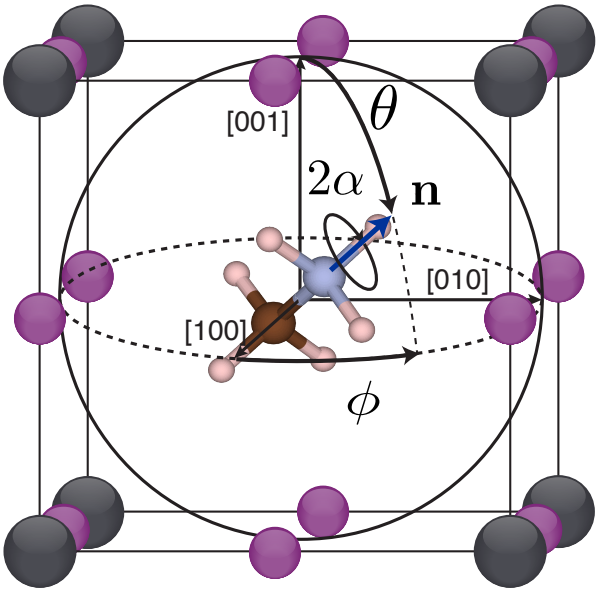

Figure 3.1: Molecular rotational degrees of freedom described by the axis-angle representation. Orientation of the C−N bond axis is given by $\mathbf{n}(\phi, \theta)$, and on-axis rotations are described by the angle 2α about the bond axis.

that molecular orientation has minimal effect on the band structure. In contrast, distortions of the inorganic Pb−I lattice in response to different orientations and translations of $CH_3NH_3^+$ can cause as much as a 0.25 eV increase in the band gap and, additionally, can change it from direct to indirect.

3.2 Methods

Energies associated with molecular rotation were calculated with density functional theory (DFT) as implemented in the Vienna ab initio Simulation Package (VASP) [104, 105] using projector augmented wave [104, 106] (PAW) pseudopotentials within the Perdew-Burke-Ernzerhof (PBE) generalized gradient approximation (GGA) [107]. Approximate van der Waals corrections were accounted for with the zero damping DFT-D3 method of Grimme [108]. For the cubic aristotype a 6×6×6 k-point mesh centered at the Γ point was employed with a 700 eV plane wave energy cutoff. Energies were converged

to within 1 meV/atom with respect to k-point density. A volume relaxation of the cubic parent phase resulted in an optimized lattice parameter of 6.32 Å which agrees very well with the experimental lattice parameter 6.3286 Å at 343 K. [95] The methylammonium cation geometry and bond lengths were adapted from experimental and computational structures of the orthorhombic phase at 100 K. [96, 100] The final molecular geometry was obtained by relaxing the molecular cation geometrically centered on the cubic perovskite A-site with a staggered H arrangement, and this geometry was fixed throughout all subsequent rigid-body rotations and translations. Energies associated with molecular rotations were calculated for a single unit cell within a rigid cubic inorganic lattice. Crystal structures were visualized using the VESTA program suite. [109]

3.3 Results and Discussion

We define molecular rotations with respect to a reference configuration where the C−N bond axis is oriented in the [100] direction of the cubic host. As shown in Figure 3.1, the rotational degrees of freedom can be described by the axis-angle representation where the polar angle θ and the azimuthal angle ϕ define an orientation vector for the C−N bond. This vector also serves as a rotation axis, with 2α denoting the rotation angle around the C−N bond. The inclination of the molecule from the xy plane is given by $|\theta - \pi/2|$ while the azimuthal angle, ϕ, describes the counterclockwise rotation around the z-axis. For $\theta = 90°$ and $\phi = 45°$ the molecular C−N axis points toward the edge of the cubic unit cell in the [110] direction, while $\theta = 54.74°$, $\phi = 45°$ corresponds to a molecular orientation along the body diagonal of the cubic unit cell in the [111] direction.

The Kohn-Sham energy landscapes of molecular rotations were calculated in an ideal cubic perovskite crystal structure which corresponds to the average high temperature (>330K) phase observed in $CH_3NH_3PbI_3$. In addition to molecular rotations we also

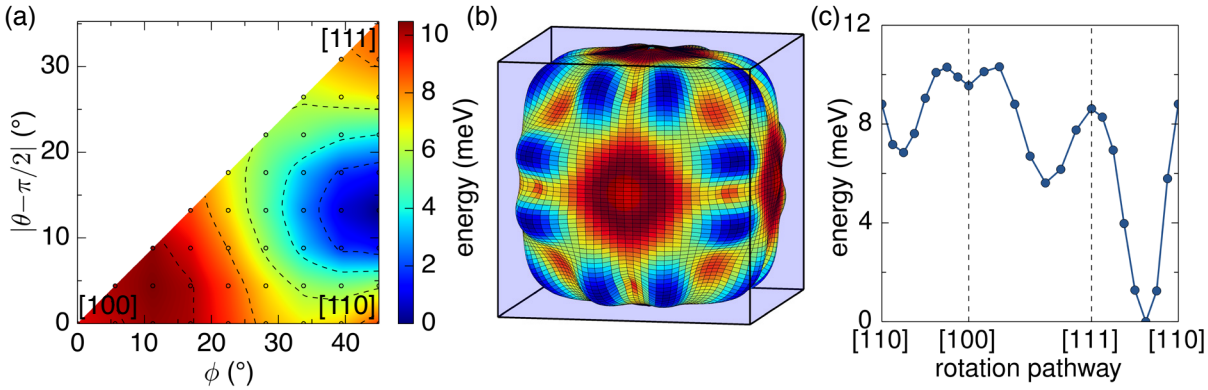

Figure 3.2: (a) Interpolated energy surfaces for molecular reorientation of $CH_3NH_3^+$ within cubic PbI_6 octahedral cages where the molecular geometrical center of mass resides at the A-site. At each orientation, the energy corresponding to the minimum energy on-axis rotation is plotted. (b) Polar plot of orientational energy surface where the radius is proportional to $|E - \beta E_{\max}|$ of scale from (a) where $\beta = 1 - {}^1/_{1000}$. (c) Energies for selected rotational pathways along the edges of the aymmetric orientation region which represent rotations within the (001) and ($\bar{1}$10) lattice planes via [100] $\rightarrow$ [110] and [001] $\rightarrow$ [111] $\rightarrow$ [110] rotations, respectively.

considered translation of the A-cation within the cage formed by the PbI_6 octahedra. Due to the cubic symmetry of the perovskite structure, it is sufficient to consider only orientations within the region enclosed by the [100], [110], and [111] crystallographic directions, which we will refer to as the asymmetric region in orientation space. The 48 symmetry operations of the Oh point group tile the asymmetric region over the complete orientation space. We calculated the energies associated with on-axis rotations and translations of up to 1.0 Å in the direction of the N atom over a grid that spanned the asymmetric region of orientation space.

To probe the strength and nature of the interactions between the molecular A-cation and the inorganic Pb−I sublattice, we first consider the energy surface associated with the ideal cubic structure with the molecule's geometric center of mass located at the ideal perovskite A-site. The calculated energy surface is shown in Figure 3.2(a,b). The minimum energy surface for the centered molecule is constructed by considering the minimum energy on-axis rotation, 2α, of $CH_3NH_3^+$ at each orientation (θ,ϕ). In this

way, the minimum energy surface for the space of all rigid body rotations is considered at zero translation. Figure 3.2c reveals a shallow energy surface for the centered molecule in which any reorientation is met by a small energy barrier <11 meV. Thus, the molecular *A*-cation should tumble freely above room temperature if its position is restricted to the center of the cubic inorganic cage.

However, when translations of $CH_3NH_3^+$ are taken into account, as shown in Figure 3.3(a,b,c) for the three high-symmetry molecular orientations, it becomes clear that the center of the perovskite *A*-site cage is not the lowest energy configuration for the molecular cation. Instead, translation in any positive direction (in the direction of the ammonium group) lowers the energy. Due to the point group of the molecule, all energy surfaces obey the symmetries of C_3; therefore only on-axis rotations up to 120° need be considered. In the [100] direction (Figure 3.3a), minima occur for a 0.6 Å translation toward the face of the cubic unit cell while on-axis rotations remarkably have no effect on the energy surface. In the [110] and [111] directions, however, the energy does depend strongly on both molecular translations and on-axis rotations. When oriented toward the edge of the cubic unit cell along the [110] direction (Figure 3.3b), the molecular cation favors a 0.3 Å translation with two equivalent low-energy rotational configurations. Similarly, in the [111] orientation (Figure 3.3c), the *A*-cation tends to off-center by 0.4 Å, and adopts a preferred rotational configuration aligned with proximal I atoms. The locus of minimum energy translations are summarized in Figure 3.4, which depicts off-centering preferences toward the face of the cubic unit cell and along the body diagonal.

We attribute the tendencies to off center and to adopt specific rotational states to N−H···I hydrogen-bonding interactions. For instance, at a translation of 0.4 Å in the [111] direction, the local minimum observed in Figure 3.3c corresponds to near alignment and N−H···I distances of approximately 2.6 Å. In contrast, the local maximum along the 0.4 Å translation for the same direction corresponds to an on-axis rotation that

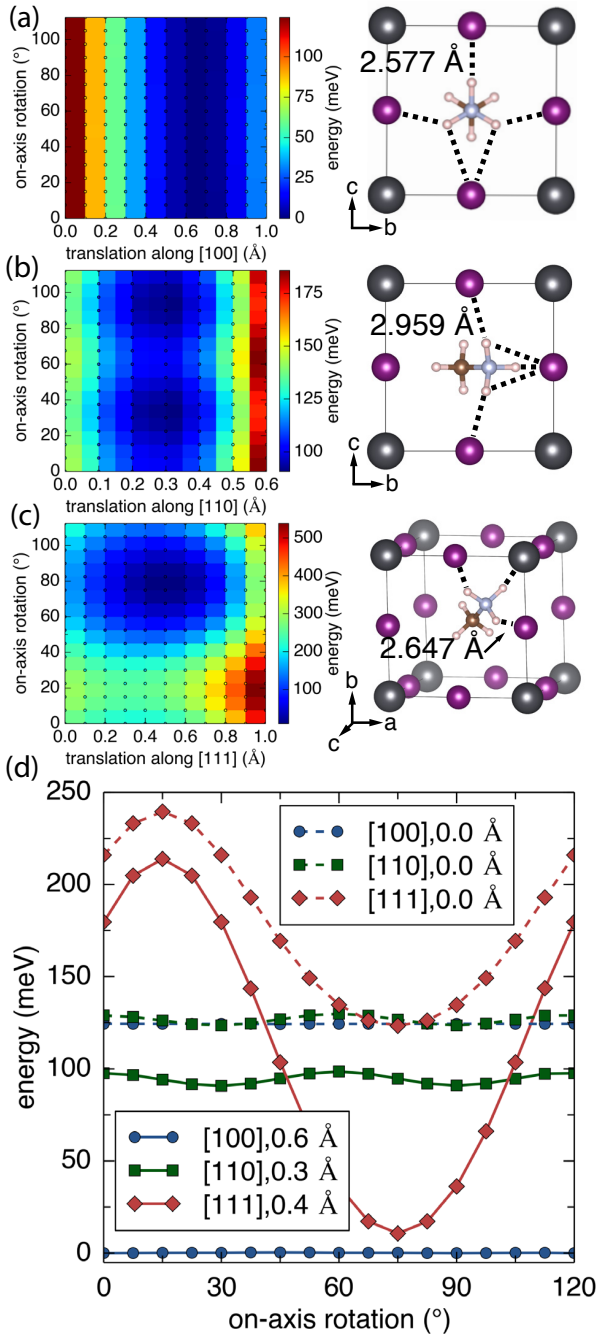

Figure 3.3: (a,b,c) Energy surfaces plotted as heat maps for the three high symmetry directions showing the effect of molecular translation and twisting rotations. Energy heat maps (a,b,c) share the same absolute energy scale but are shown with relative color scales. Low energy configurations in each high symmetry orientation are shown with the minimum N−H$\cdots$I distance labeled. (d) Relative energies associated with on-axis rotations at zero translation and the minimum energy translation in each direction.

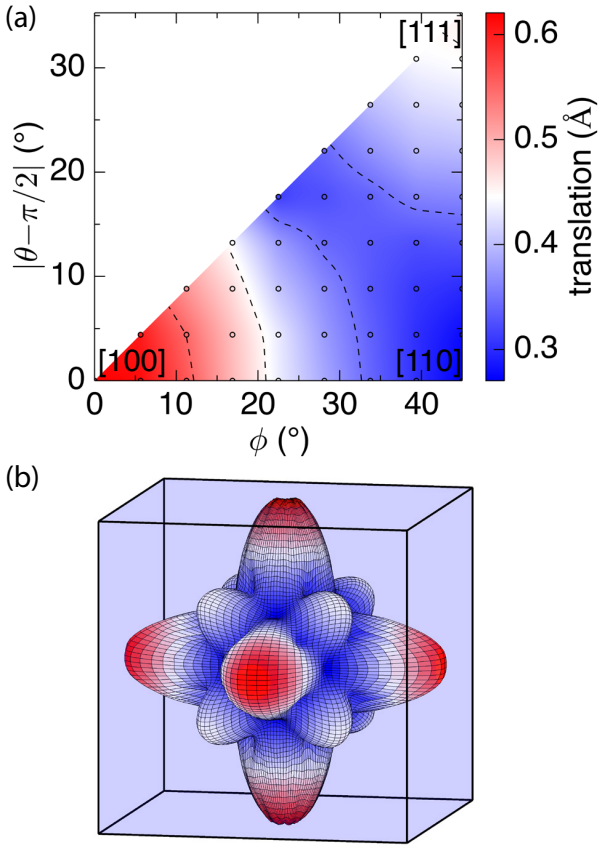

Figure 3.4: (a) Within the asymmetric orientation region, the translations associated with the lowest energy configurations are plotted. The inclination and azimuthal angles are given relative to the [100] reference configuration. (b) Polar plot where the radius is proportional to the minimum-energy translation providing a representation of the locus of minimum energy molecular translations throughout the cubic unit cell.

maximizes N−H···I distances. The effect of on-axis rotations decreases from the [111], [110] to [100] directions as shown in Figure 3.3d. Along the body-diagonal of the cubic unit cell, on-axis rotations which minimize N−H···I distances are stabilized by 203 meV compared to the rotation that maximizes N−H···I distances. On the other hand, on-axis rotations only account for a 7 meV energy decrease in the [110] direction, and, in the [100] direction, there is no preferred on-axis rotation. These differences stem from the number of favorable N−H···I interactions for the different orientation geometries. Along [111] (Figure 3.3c), the molecule can simultaneously minimize three N−H···I dis-

tances (2.64 Å); thus on-axis rotations encounter a large energy penalty as these three interactions are all simultaneously disrupted. Along [110] (Figure 3.3b), the energy is lowered by only two minimized N−H···I distances (2.96 Å). Hence, when the molecule rotates it is able to form a new N−H···I bond as it breaks two old ones resulting in a lower energy barrier to on-axis rotations. Lastly, in the [100] orientation (Figure 3.3a), only one N−H···I is minimized at a time (2.58 Å), so upon on-axis rotation, a favorable N−H···I interaction is reformed as soon as an old one is broken, resulting in an extremely shallow energy profile. These trends show that the differences in calculated energy barriers to on-axis rotation between the high-symmetry orientations stem from the number of disrupted N−H···I interactions.

Figure 3.5(a,b,c) shows the energy as a function of orientation (θ, ϕ), after minimizing not only over on-axis rotations, but also over translational degrees of freedom. A comparison with Figure 3.2, where translations were not treated as a degree of freedom, reveals the significant impact that molecular off-centering from the *A*-site has on the crystal energy. Molecular transitions between two locally stable configurations require reorientation, translation and an axial rotation. The most favored directions are in the [100] and [111] orientations, separated by high energy barriers to reorientation. Figure 3.5c, for example, shows that the reorientation from [110] to [100] (corresponding to molecular rotation in the (001) plane) encounters a 100 meV energy barrier. For the molecule to reorient between the [100] and [111] directions it must surmount an 85 meV energy barrier, while an 80 meV energy barrier separates the [110] and [111] orientations. Hence, a molecule rotating within the $(\bar{1}10)$ plane from the z-axis, through [111] to [110] and $[11\bar{1}]$ to the negative z-axis encounters a maximum barrier of 85 meV. Moreover, Figure 3.5 shows the large stabilization of the [100] direction when translations are considered, which is a result of reduced N−H···I distances. In particular, the energies for the low-energy configurations in the high-symmetry directions decrease as the N−H···I distances de-

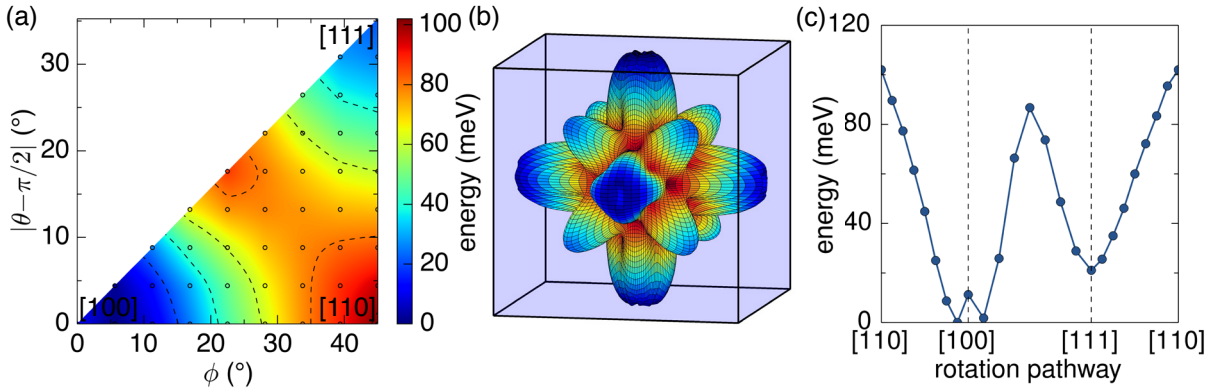

Figure 3.5: (a) Interpolated energy surfaces for molecular reorientation of $CH_3NH_3^+$ within cubic PbI_6 octahedral cages. At each orientation, the energy corresponding to the minimum energy on-axis rotation and minimum-energy translation is plotted. (b) Polar plot of orientational energy surface where the radius is proportional to $|E - \beta E_{\max}|$ of scale from (a) where $\beta = 1 - {}^1/_{1000}$. (c) Energies for selected rotational pathways along the edges of the asymmetric orientation region which represent rotations within the (001) and $(\bar{1}10)$ lattice planes via [100] $\rightarrow$ [110] and [001] $\rightarrow$ [111] $\rightarrow$ [110] rotations, respectively.

crease from 2.96 Å for the [110] orientation to 2.65 Å along [111] and to 2.58 Å along [100], resulting in relative energies $E_{\min}^{[110]} > E_{\min}^{[111]} > E_{\min}^{[100]}$. Thus as identified above, the number of N$-$H$\cdots$I interactions dictates the barrier to on-axis rotation, but $CH_3NH_3^+$ orientational preferences originate from minimizing N$-$H$\cdots$I distances.

We also investigated the electronic band structure as a function of molecular orientation to assess the impact of molecular rotation on the electronic properties of $CH_3NH_3PbI_3$. It is well known that Pb 6*s* and I 5*p* σ-antibonding orbitals form the top of the valence band while Pb 6*p* and I 5*p* π-antibonding orbitals contribute to the bottom of the conduction band. [110] The calculated atomic orbital contributions to the electronic density of states in Figure 3.6a confirm the participation of Pb *s* and I *p* orbitals in the valence band as well as Pb *p* and I *p* orbital contributions to the conduction states. Therefore, the inorganic Pb$-$I host lattice dictates the electronic properties of the $CH_3NH_3PbI_3$ perovskite. This is verified by the calculated electronic band structures for the three high-symmetry $CH_3NH_3^+$ orientations in a cubic PbI_3 host shown in Figure 3.6a. The

almost perfectly overlapping band structures in Figure 3.6a reveal that molecular orientation plays a minimal role in determining the nature of the bands near the band gap.

Pb-containing compounds often exhibit interesting lone pair chemistry which typically manifests in high Born effective charges indicating a tendency for Pb off-centering and the formation of local dipoles. [111, 112] The calculated Born effective charge tensors for the Pb^{2+} ions of cubic $CH_3NH_3PbI_3$ is predicted to be nearly isotropic with values of the averaged trace around 4.9 e. Well above the nominal value of $+2\,e$, the high values for the Born effective charges suggest a highly polarizable Pb s-lone pair. Figure 3.6(b,c,d), showing the summed partial charge density near the top of the valence bands, reveals the interplay between the molecular dipole and the Pb s-lone pair. As is evident in Figure 3.6(b,c,d), the orientation of the A-cation affects the charge density surrounding the Pb atoms. In fact in the cubic perovskite, an asymmetry arises in the Pb valence electron distribution, with the Pb valence states tending to polarize in opposition to the molecular orientation. Due to the periodic boundary conditions imposed in our calculations, it must be recognized that the partial charge density represents that of a crystal with periodically aligned organic cations in a ferro arrangement, where the orientation, translation, and on-axis rotations are repeated periodically throughout the crystal. The presence of such ferroelectric domains at ambient temperature is an intensely debated topic. Several studies [113, 114, 115] suggest that ferroelectric domains exist at room temperature and aid carrier separation through internal electric fields while others [116, 117] observe no appreciable macroscopic polarization. While the reported partial charge densities may not represent operating conditions at high-temperatures due to the artificial periodic boundary conditions, in the presence of an applied electric field, $CH_3NH_3PbI_3$ does exhibit macroscopic polarization. [117] In this context, the predicted high Pb^{2+} Born effective charges and the sensitivity of the Pb valence charge on molecular orientation

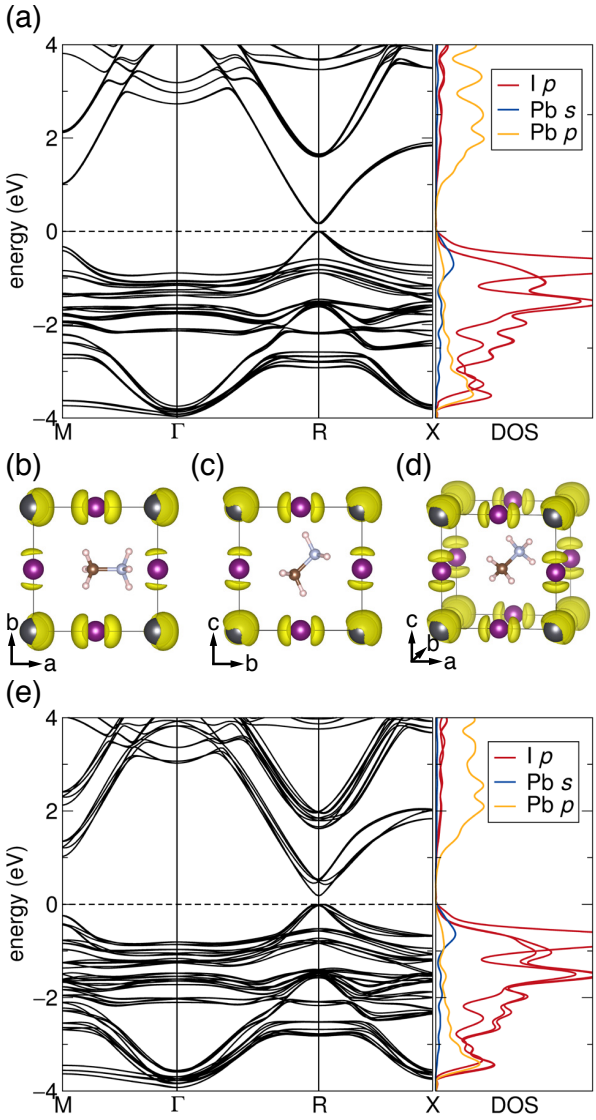

Figure 3.6: (a) Overlayed band structures for high symmetry molecular orientations in the ideal cubic perovskite depicting the direct band gap at the R point in GGA-PBE with spin-orbit coupling. DOS presented for the lowest energy [100] orientation. (b,c,d) Partial charge density associated with top of the valence band for the high symmetry directions ([100], [110], [111]), showing the Pb s and I p orbital character at isosurface levels of 1.912×10^{-5}, 1.925×10^{-5} and 1.920×10^{-5} $e/\text{Å}^3$, respectively. (e) Overlayed band structures for the three high symmetry molecular orientations after relaxing only the inorganic lattice. DOS shown for relaxed [100] orientation.

suggests that the Pb s-lone pair plays a role in the polarizability and dielectric response of $CH_3NH_3PbI_3$.

The high-temperature $CH_3NH_3PbI_3$ cubic phase is stabilized by vibrational entropy and experiences large oscillations of the inorganic octahedral network, with root-mean-squared atomic displacements as high as 0.41 Å for the I-sublattice in the direction perpendicular to the Pb−I−Pb bond. [85] Hence, while the calculated rigid-body rotational energy landscape (Figure 3.5) corresponds to $CH_3NH_3^+$ motion within the average cubic structure with nominal 180° Pb−I−Pb bond angles, the local *A*-site environments of the actual crystal fluctuate freely as a result of I-sublattice displacements at finite temperature (>330 K).

The true energy landscape of the solid is substantially more complex than that probed in this study. It depends not only on the rotational and translational degrees of freedom of $CH_3NH_3^+$, but also on the displacement degrees of freedom of the Pb and I host atoms. Collective octahedral tilting degrees of freedom are especially important as they are in part responsible for the symmetry breaking phase transformations upon cooling [94, 95, 43, 96] and likely dominate the anharmonic vibrational excitations that stabilize the high temperature cubic phase. Mapping out this more complex energy landscape can be done with an effective Hamiltonian [118, 64, 119, 120, 121, 122] that is expressed as a function of displacement degrees of freedom of the inorganic host along with the rotational and translational degrees of freedom of the *A*-cation. High temperature behavior as well as low temperature symmetry breaking orderings can then be probed with Monte Carlo simulations.

While a full statistical mechanics study relying on an effective Hamiltonian is beyond the scope of this work, we can nevertheless obtain a sense of the coupling between displacement degrees of freedom of the PbI_3 host and the orientational and translational degrees of freedom of $CH_3NH_3^+$ by considering relaxations of the host for different rigid molecular orientations and translations. To this end, we performed DFT relaxations in which the internal degrees of freedom of the inorganic lattice (within a fixed cubic unit

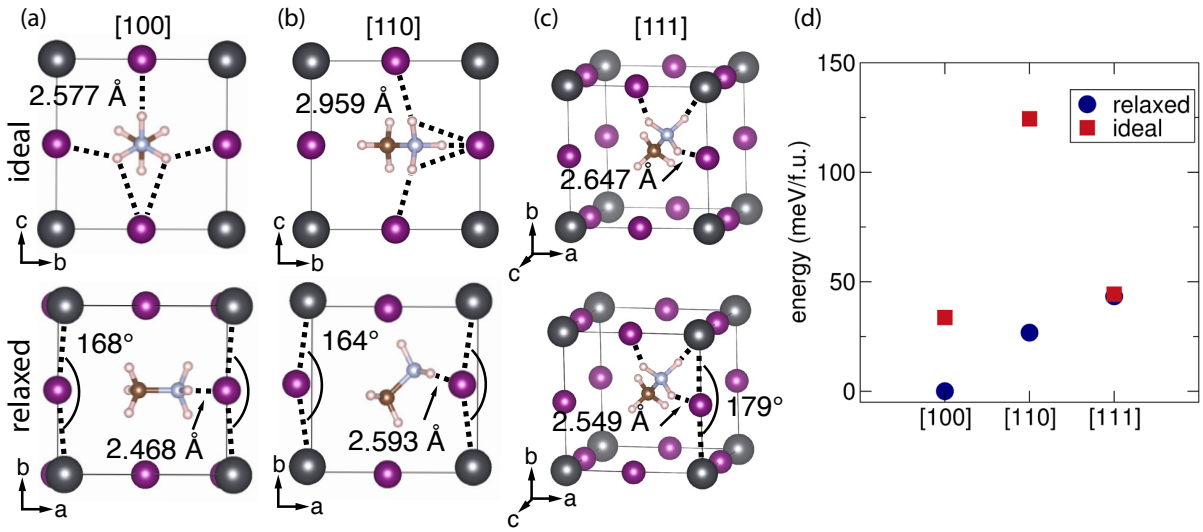

Figure 3.7: (a,b,c) Ideal (cubic) and relaxed inorganic lattice around rigid $CH_3NH_3^+$ molecules in the [100],[110], and [111] directions, respectively. (d) Relative energy comparison per formula unit of the ideal and relaxed configurations for each of the three high-symmetry orientations.

cell) were allowed to relax to forces less than 5 meV/ Å while the molecular cation was held rigidly in place. Both the Pb and I-sublattices experience significant distortions from the ideal cubic aristotype as shown in Figure 4.4(a,b,c) where the N−H···I distances as well as Pb−I−Pb angles are labeled to emphasize the relevant distortions.

The most significant distortions are observed for the [110] orientation (Figure 4.4b) with 164° Pb−I−Pb bond angles. Similarly, in the relaxed [100] configuration (Figure 4.4a), Pb−I−Pb bond angles of 168° are found. The observed I-sublattice displacements support the idea that N−H···I interactions play a dominant role in stabilizing the preferred molecular orientations.

Relaxation of Pb and I around a rigid $CH_3NH_3^+$ molecule also has a dramatic effect on the electronic band structure of the material. Figure 3.6e, shows the calculated electronic band structures corresponding to configurations with relaxed Pb and I ions. Since the inorganic Pb−I host lattice governs the electronic properties of $CH_3NH_3PbI_3$, distortions in the Pb−I−Pb bond angle directly impact the band structure near the band gap. The

distortions of the inorganic cage widen the band gap by almost 0.25 eV, and the nature of the band gap changes from direct to indirect, which has been previously identified as a factor leading to an increase in minority carrier lifetime and to the suppression of radiative recombination [17].

3.4 Conclusions

In summary, we have calculated the energy surface of $CH_3NH_3PbI_3$ as a function of the orientational, translational and on-axis rotational degrees of freedom of $CH_3NH_3^+$ within the *A*-site cage of the cubic Pb−I perovskite host. Our calculations show that N−H$\cdots$I interactions play a dominant role in determining low energy $CH_3NH_3^+$ orientations and translations. The energy landscape as a function of molecular orientation when minimized over translational and on-axis rotational degrees of freedom is highly anisotropic, a property that should be accounted for in meso-scale models of this compound. Translational degrees of freedom are found to be especially important with the equilibrium translations exhibiting a strong dependence on molecular orientation. Molecular reorientation in cubic Pb−I will therefore require substantial rigid translation when following the minimum energy surface. We also found that the band structure of cubic $CH_3NH_3PbI_3$ is relatively insensitive to the *A*-cation orientation, but can change substantially when the Pb−I host is allowed to relax in response to different configurations of $CH_3NH_3^+$. In addition to revealing the nature of the interactions between $CH_3NH_3^+$ and the inorganic perovskite host, the results of this work set the stage for future statistical mechanics studies relying on effective Hamiltonians to probe the finite temperature vibrational, rotational and translational excitations and their effect on electronic structure in this fascinating class of materials.

Chapter 4

Octahedral Tilting Instabilities in Inorganic Halide Perovskites

4.1 Introduction

Since the introduction of hybrid perovskite materials for photovoltaics in 2009, [1] the materials community has seen a resurgence in halide perovskite research. Hybrid perovskite photovoltaic device efficiencies approach those of silicon based technologies for PV; [24] however, stability issues, such as photo-degradation under irradiation and decomposition to a yellow photo-inactive phase, [8, 50, 123] prevent commercial adoption of hybrid perovskite photovoltaics. Techniques to enhance structural stability include substitution on the A-site to stabilize the photo-active black perovskite polymorphs [23, 24, 25, 26, 27] while substitution on the halide site can be used to tune the bandgap of these materials. [28, 29, 30, 31] Alloy engineering has aided efficiencies and stability of halide perovskite-based devices; [25] however, the end members must be fully understood in order to appreciate emergent structure property relationships.

The remarkable electronic properties of halide perovskites stem from low carrier trap-

ping and low recombination rates that result in diffusion lengths [5] and lifetimes [6, 7] on par with pristine III-V semiconductors. [8, 9, 10, 11, 12, 13, 14, 6] The goal of resolving the origin of unexpectedly low recombination rates in these solution-processed materials continues to motivate many theoretical and experimental studies on halide perovskite photophysics. Several explanations for low carrier recombination include polaron formation, [21, 22, 12] local dynamical Rashba splitting, [15, 16, 17, 18, 15, 19, 20] and dielectric screening. [36, 37, 38, 39, 40, 41, 42] The common denominator of these hypotheses is the necessity of a highly polarizable and deformable lattice facilitated by anharmonic dynamic fluctuations including octahedral tilting, [18, 124, 125, 126, 127] dynamical A- [128] and B-site off-centering, [129, 42] as well as orientational disorder of the A-site organic cation. [32, 33, 21, 34, 35] In this study, we use DFT to investigate the origin of structural instabilities and the role of octahedral tilting, strain, and A-site displacements in phase stability of inorganic perovskites.

Halide perovskites undergo structural phase transitions as a function of temperature due to an undersized A-cation which gives rise to octahedral tilt instabilities as explained geometrically by the Goldschmidt tolerance factor. [130] In the description of halide perovskite phase transitions, the high temperature cubic (α) phase with space group $Pm\bar{3}m$ transitions either to a tetragonal P4/mbm phase $a^0a^0b^+$ with in-phase tilts in Glazer notation [93] or I4/mcm phase with out-of-phase tilts $a^0a^0b^-$. The prototypical hybrid perovskite $CH_3NH_3PbI_3$ adopts the I4/mcm phase [131] at intermediate temperature while inorganic perovskites have been observed to transition to the P4/mbm phase. [43, 44, 45, 42, 46, 47, 48, 49, 50] Finally, both inorganic and hybrid perovskites show Pnma ground state γ-phases with $a^-a^-b^+$ tilts. [49, 132, 8, 133, 134] Several compounds, particularly $CsPbI_3$ and $CsSnI_3$, [135] also exhibit a photo-inactive, non-perovskite yellow polymorph, known as the δ-phase which consists of 1D chains of face sharing octahedra. [136, 8, 132, 49] While the δ-phase is likely the thermodynamic

equilibrium phase of these materials at low temperatures, [137, 24, 23, 138, 100, 139] the technologically relevant phases include only the perovskite series. Therefore in this study we focus only on the inorganic perovskite polymorphs even though we recognize they may be metastable at operating temperatures for devices.

We investigate the Born-Oppenheimer energy landscape associated with octahedral tilt instabilities to understand the impact of strains and A-cation off-centering on phase stability. We first describe primary tilt order parameters in terms of symmetry adapted collective displacement modes for $Pm\bar{3}m$ space group irreducible representations R_4^+ and M_3^+. Using the Hencky strain metric, we describe secondary strain order parameters and enumerate symmetry-allowed strains for the 14 unique tilt systems. Lastly, the role of the A-site cation is investigated. We find that inorganic perovskites all show Pnma ground states, and the relative stability compared to the cubic phase correlates with the ratio of the ground state and cubic volumes. In fact, the correlation holds for all tilt systems studied: the relative energy of an octahedrally tilted perovskite system is dictated by its decrease in volume. Finally, we demonstrate the importance of A-site displacements and strain coupling in stabilizing the Pnma ground state structure.

4.2 Methods

DFT calculations were carried out using the Vienna ab initio Simulation Package (VASP) [104, 105] with a plane-wave basis set and projector augmented wave [104, 106] (PAW) pseudopotentials. Electron exchange and correlation were approximated within the Perdew-Burke-Ernzerhof (PBE) generalized gradient approximation (GGA) [107]. For the cubic primitive cell a $8\times8\times8$ k-point mesh centered at the Γ point was employed with a 600 eV plane wave energy cutoff. Energies were converged to within 1 meV/atom with respect to k-point density. Geometric optimization of the 14 distinct octahedral tilt

systems, calculated in a $2 \times 2 \times 2$ supercell, were seeded with an initial displacement field associated with the octahedral rotations, and all degrees of freedom were allowed to relax until forces were converged to within 5 meV/Å. Static calculations for the tilt subspaces were made over a grid of order parameter amplitudes, and selective dynamics was used to optimize only the Cs cation positions until energies were converged to within 1 meV. To obtain accurate lattice vectors for decomposition into strain order parameters, a strict force convergence criterion to within 0.5 meV/ Åwere used for geometric optimizations of all translational and rotational equivalents. In plotting the strain order parameters, the strains of translationally equivalent structures were averaged. Crystal structures were visualized using the VESTA program suite. [109]

4.3 Perovskite Crystallography

We focus on three degrees of freedom to develop an understanding of the microscopic aspects of phase transitions in inorganic halide perovskites. First, symmetry-adapted normal modes are considered to describe rotations of the metal-halide octahedra. Second, we define symmetry adapted strain order parameters which measure macroscopic lattice deformations. Lastly, we consider the effect of collective A-cation displacements within the perovskite structure.

4.3.1 Octahedral Tilt Order Parameters

Due to the structural flexibility of a lattice of corner-connected octahedra, ionic perovskites tend to undergo distortions involving octahedral tilting as well as off-centering of the A- and B-site cations.[18, 124, 125, 126, 127] The phase sequence of inorganic halide perovskites is shown along with the space group symmetry in Figure 4.1(a). The phase sequence involves a high temperature cubic α-phase, an intermediate tetragonal β-phase,

and a low temperature orthorhombic γ-phase. Along with changes in lattice parameter, each phase is distinguished by the presence of metal-halide octahedral rotations. Here we consider two types of octahedral rotations: (1) in-phase rotations about a common axis where every octahedron along the axis rotates in the same direction by the same amplitude (left panel of Figure 4.1(b)) or (2) out-of-phase rotations about a common axis where the amplitude of rotation changes sign for each octahedron along the rotation axis (right panel of Figure 4.1(b)). The rotation axes are considered to lie along the high symmetry lattice vectors of the cubic crystal, and here we will assume that the lattice vectors coincide with the Cartesian axes.

Since octahedral rotations in perovskites can be distinguished by three rotation axes and two types of rotation (in- or out-of-phase) a complete description of the degrees of freedom involves a six component order parameter $\boldsymbol{\eta} = (abcdef)$ where a, b, c and d, e, f denote the amplitude of in-phase and out-of-phase rotations, respectively. While $\boldsymbol{\eta}$ spans a six dimensional space, we restrict ourselves by considering only *pure* tilt systems by enforcing either only in-phase or out-of-phase rotations to be nonzero for a particular rotation axis. Hence, $\boldsymbol{\eta} = (abc000)$ describes a tilt system of in-phase rotations about each axis of differing amplitudes while $(a000bb)$ corresponds to an in-phase rotation along the x-axis and simultaneous out-of-phase rotations of equal amplitude about the y and z axes. As an alternative notation for octahedral tilting, Glazer [93] notation uses a three component vector to encode the three crystallographic axes, a lower case letter to denote tilt amplitude, and a $+$ or $-$ exponent to denote in-phase or out-of-phase rotations, respectively. Thus the order parameter $(abc000)$ corresponds to the $a^+b^+c^+$ tilt system while $(a000bb)$ corresponds to $a^+b^-b^-$.

The full six dimensional order parameter $\boldsymbol{\eta}$ corresponds to crystal normal modes of the R_4^+ and M_3^+ irreducible representations (irreps) of the crystal space group. Normal

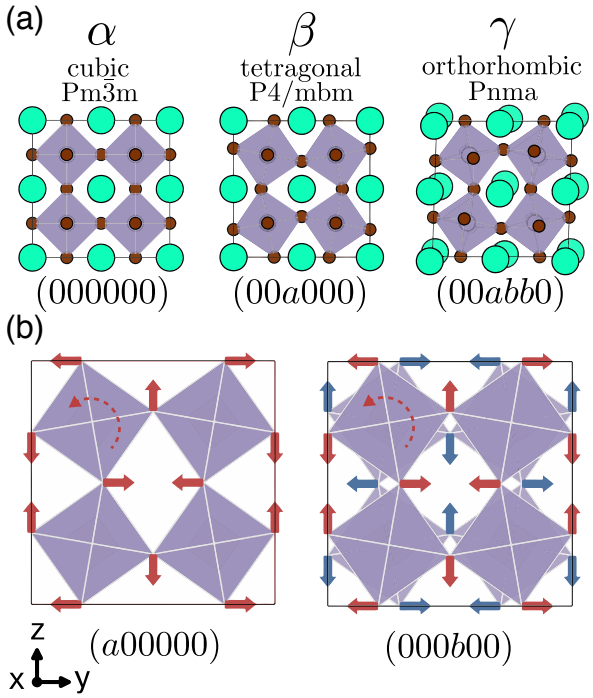

Figure 4.1: (a) The three phases observed as a function of temperature for $CsXY_3$ perovskites. Cubic $Pm\bar{3}m$ α-phase has no activated tilt modes. Tetragonal P4/mbm β-phase contains an in-phase tilt along one axis. Orthorhombic Pnma γ-phase contains one in-phase tilt mode and two equal out-of-phase tilt modes. (b) The left panel schematically depicts the displacement field corresponding to the (a00000) order parameter (in-phase tilt mode along the x-axis), while the right panel depicts the out--of-phase tilt mode (000b00). Tilt modes along the y- and z- directions are similarly defined where the diagrams would be viewed perpendicular to the zx- and xy-planes, respectively.

modes that transform as the three dimensional irreps R_4^+ and M_3^+ approximate the effect of out-of-phase and in-phase rotation of the the metal halide octahedra. To generate the displacement fields that transform as R_4^+ and M_3^+, it is necessary to work within a supercell that is commensurate with the R-point and M-point of the Brillouin zone. By considering atomic displacements in a $2 \times 2 \times 2$ supercell we generate all symmetry adapted collective displacements corresponding to phonon modes at commensurate k-points including the R-point $(\frac{1}{2}, \frac{1}{2}, \frac{1}{2})$, the M-point $(\frac{1}{2}, \frac{1}{2}, 0)$, the X-point $(\frac{1}{2}, 0, 0)$ and the Γ-point $(0, 0, 0)$.

Table 4.1: Symmetry allowed secondary strain order parameters due to octahedral rotations.

Space Group # *name*	M_3^+ *(a,b,c)*	R_4^+ *(a,b,c)*	*Strain* $(e_1, e_2, e_3, e_4, e_5, e_6)$
221 $Pm\bar{3}m$	(0,0,0)	(0,0,0)	(A,0,0,0,0,0)
127 P4/mbm	(0,0,a)	(0,0,0)	(A,0,B,0,0,0)
139 I/mmm	(0,a,a)	(0,0,0)	(A,$\frac{\sqrt{3}}{2}$B,$-\frac{1}{2}$B,0,0,0)
204 $Im\bar{3}$	(a,a,a)	(0,0,0)	(A,0,0,0,0,0)
71 Immm	(a,b,c)	(0,0,0)	(A,B,C,0,0,0)
140 I4/mcm	(0,0,0)	(0,0,a)	(A,0,B,0,0,0)
74 Imma	(0,0,0)	(0,a,a)	(A,$\frac{\sqrt{3}}{2}$B,$-\frac{1}{2}$B,C,0,0)
167 $R\bar{3}c$	(0,0,0)	(a,a,a)	(A,0,0,$-\frac{\sqrt{3}}{3}$B,$\frac{\sqrt{3}}{3}$B,$\frac{\sqrt{3}}{3}$B)
12 C2/m	(0,0,0)	(0,a,b)	(A,B,C,D,0,0)
15 C2/c	(0,0,0)	(b,b,a)	(A,0,B,$-\frac{\sqrt{2}}{2}$C,$\frac{\sqrt{2}}{2}$C,D)
2 $P\bar{1}$	(0,0,0)	(a,b,c)	(A,B,C,D,E,F)
63 Cmcm	(0,0,a)	(0,b,0)	(A,B,C,0,0,0)
62 Pnma	(0,0,a)	(b,b,0)	(A,0,B,0,0,C)
11 $P2_1/m$	(0,0,a)	(b,c,0)	(A,B,C,0,0,D)
137 $P4_2/nmc$	(0,a,a)	(b,0,0)	(A,$\frac{\sqrt{3}}{2}$B,$-\frac{1}{2}$B,0,0,0)

To find collective displacement modes of the 40 atom supercell, we first collect the coordinates of all atoms in a (120×1) column vector $\mathbf{r}$. The displacements of the atoms, $\mathbf{d}$, from their ideal crystallographic locations, $\mathbf{r}_0$, are given by $\mathbf{r} = \mathbf{r}_0 + \mathbf{d}$. We construct the Cartesian symmetry representation $\mathbf{M^d}$ for the factor group, G, as described by Thomas and Van der Ven [140] which describes how the vector of displacements transforms under a crystal symmetry operation $\mathbf{g}$ by the equation $\mathbf{d'} = \mathbf{M^d}(g)\mathbf{d}$. Next, we find a coordinate transformation,

$$\mathbf{d} = \mathbf{Q}\boldsymbol{\eta}, \tag{4.1}$$

for which the matrix $\mathbf{Q}$ block diagonalizes the symmetry representation of the order parameter space, $\mathbf{M^{\eta}}(g) = \mathbf{Q}^{\top}\mathbf{M^d}(g)\mathbf{Q}$ for all symmetry operations $g \in G$. In this context the columns of $\mathbf{Q} = [\mathbf{q_1}\mathbf{q_2}...]$, represent the symmetry-adapted collective displacement modes. For a certain column $\mathbf{q}_i$ the corresponding amplitude is η_i. In this

way we find the collective displacement modes $\mathbf{q}_1$ through $\mathbf{q}_6$ and their corresponding amplitudes η_1 through η_6 which correspond to the frozen phonon modes described by the three-dimensional R_4^+ and M_3^+ space group irreps.

Glazer *et al.* [93] and subsequently Howard and Stokes [141] enumerated the unique space groups associated with symmetry breaking due to R_4^+ and M_3^+ displacement modes. All 14 unique tilt systems (which result from symmetrically distinct combinations of in-phase and out-of-phase tilts) as well as the cubic $Pm\bar{3}m$ reference phase are listed along with their space group in Table 4.1. For each unique tilt system, there exists rotational and translational equivalents due to the symmetry of the cubic parent group. For instance, a z-oriented $a^0a^0a^+$ in-phase tilt system is equivalent to a y-oriented in phase tilt system $a^0a^+a^0$ and the x-oriented tilt system $a^+a^0a^0$. In the supplemental materials we enumerate all rotational and translation equivalents for each of the 14 unique tilt systems.

4.3.2 Strain Order Parameters

The progression of phase changes from the cubic high temperature α-phase through the intermediate tetragonal β-phase to the orthorhombic ground state γ-phase is accompanied by macroscopic strains of the crystal unit cell. Often structural phase transitions are monitored by the corresponding unit cell parameters; however, a convenient alternative is the use of strain order parameters defined relative to the cubic reference crystal.

An arbitrary lattice deformation corresponds to a left acting tensor $\mathbf{F}$ that operates as $\mathbf{L}' = \mathbf{FL}$, where $\mathbf{L}$ denotes a 3×3 matrix comprised of three lattice vectors arranged in columns as $\mathbf{L} = [\mathbf{abc}]$. We use the Hencky strain defined as $\mathbf{E} = \ln(\mathbf{F}^\top\mathbf{F})/2$ where $\mathbf{F}^\top\mathbf{F}$ is a real symmetric deformation tensor and ln refers to the matrix logarithm. Using the same group theoretical techniques as outlined in the previous section, symmetry adapted

order parameters are defined in terms of the tensor **E** as: [142]

$$e_1 = (E_{xx} + E_{yy} + E_{zz})/\sqrt{3} \tag{4.2}$$

$$e_2 = (E_{xx} - E_{yy})/\sqrt{2} \tag{4.3}$$

$$e_3 = (2E_{zz} - E_{xx} - E_{yy})/\sqrt{6} \tag{4.4}$$

$$e_4 = \sqrt{2}E_{yz} \tag{4.5}$$

$$e_5 = \sqrt{2}E_{xz} \tag{4.6}$$

$$e_6 = \sqrt{2}E_{xy} \tag{4.7}$$

The first strain order parameter, e_1, is proportional to the trace of the strain tensor and describes purely volumetric expansion or compression of the crystal. The effect of the e_1 strain order parameter is illustrated in Figure 4.2(a). When using the Hencky strain metric, e_1 is related to the volume as $e_1 = \ln(\frac{V'}{V_0})/\sqrt{3}$ where V' is the volume of the deformed lattice and V_0 is that of the reference lattice.

Deviatoric strains, spanned by e_2 and e_3 are pictured in Figure 4.2(b) where the origin represents the undistorted cubic reference phase. Along the high symmetry directions (following the blue or purple arrows in Figure 4.2(b)) volume preserving deformations (i.e. e_1 = const.) maintain 90 degree angles between lattice vectors and result in tetragonal distortions of the cubic reference lattice. For example, deformations described by e_3 result in elongation of the z-axis as shown in Figure 4.2(b). Furthermore, tetragonal deformations from elongation of the x- or y-axes show up as high symmetry lines within the e_2-e_3 strain subspace. Due to the equivalence of the x, y, and z directions in a cubic crystal, the x, y, and z-oriented tetragonal deformations are equivalent by symmetry. The use of the e_2 and e_3 strain order parameters allows us to distinguish between the

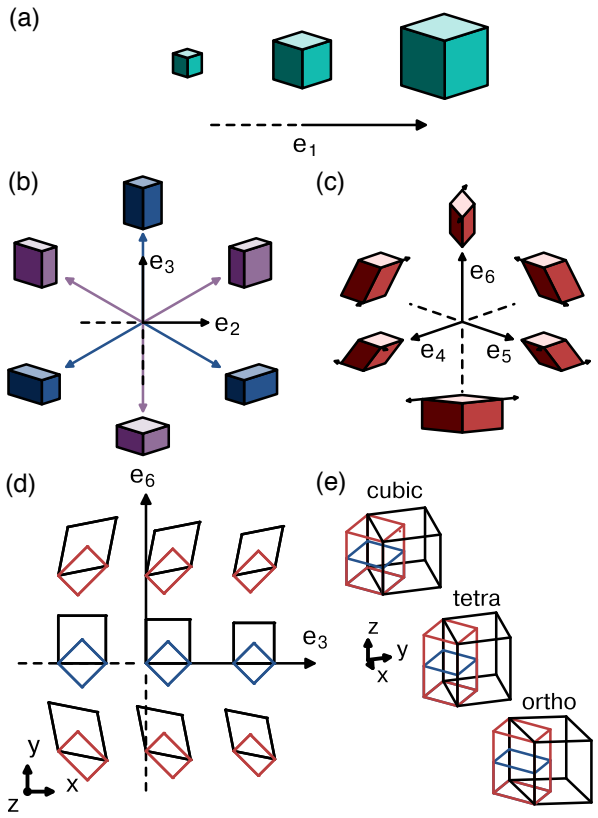

Figure 4.2: (a) Schematic representation of the volumetric e_1 strain order parameter. (b) 2D strain subspace spanned by e_2 and e_3 strain order parameters. Figures of the same color are symmetrically equivalent tetragonal variants. (c) 3D strain subspace spanned by e_4, e_5 and e_6. All variants pictured are symmetrically equivalent under rotations of the cubic reference. (d) The distortions of the primitive and supercell lattices are shown in the 2D subspace spanned by e_3 and e_6. Along e_3 the lattice maintains tetragonal symmetry (blue), and, along e_6, orthorhombic symmetry is obtained (red). (e) Depictions of the tetragonal primitive cell (blue), orthorhombic primitive cell (red) and perovskite $2 \times 2 \times 2$ supercell (black) under the associated lattice strains.

different tetragonal variants and to conveniently display all variants within a single two-dimensional plot.

The e_4, e_5, and e_6 strain order parameters describe shear strains and their effect on a cubic reference crystal is shown in Figure 4.2(c). In this work we focus on the shear distortions described by the high symmetry axes: e_4, e_5, and e_6. Strains along the e_4 , e_5, and e_6 axes distort lattice angles away from 90 degrees and correspond to orthorhombic

deformations of the cubic reference. Due to the symmetry of the parent group, all of the pictured distortions in Figure 4.2(c) are related by a rotation of the cubic crystal; therefore the six displayed shear distortions are said to be rotationally equivalent. The use of e_4 , e_5, and e_6 makes it possible to distinguish among the orthorhombic variants and to visualize all symmetrically equivalent shear strains within a three-dimensional subspace.

In this work, we treat strain as secondary order parameters to the primary tilt order parameters. When a primary tilt order parameter, denoted $\boldsymbol{\eta}$, is activated in the reference cubic crystal, the symmetry is reduced from the $Pm\bar{3}m$ space group to a subgroup which we call $G_{\boldsymbol{\eta}}$. Symmetry lowering by the primary order parameters allows different strains to take on nonzero values without changing the symmetry of the internally distorted structure. These symmetry invariant strains are known as secondary order parameters. [143]

In particular, a secondary strain order parameter must be invariant to the point group $P_{\boldsymbol{\eta}}$ associated with the space group $G_{\boldsymbol{\eta}}$ as defined above. With a symmetry representation of the point group for the strain order parameters, $\mathbf{M^e}$, as described by Thomas and Van der Ven [142], we can uncover the strains that may serve as secondary order parameters to the primary tilt order parameters through the requirement: $\mathbf{e} = \sum_{g \in P_{\boldsymbol{\eta}}} \mathbf{M^e}(p)\mathbf{e}$ where $\mathbf{e}$ is a vector of the strain order parameters e_1 through e_6 and $\mathbf{M^e}(p)$ denotes the strain symmetry representation for a symmetry operation p.

Table 1 shows symmetry allowed secondary strain order parameters relative to the cubic crystal for each octahedral tilt system. The directions in strain space are invariant to the point group imposed by the primary tilt order parameter. The listed invariant strain direction (e.g. (A,0,B,0,0,0)) therefore corresponds only to the listed tilt distortion. In order to find the symmetrically equivalent directions, one must apply the symmetry operations of the parent group to the strain order parameter. We include a full description

of allowed strain order parameters for all rotational and translational variants of each tilt system in the supplemental materials.

4.3.3 Strain/Tilt Order Parameters for $\alpha \rightarrow \beta \rightarrow \gamma$ Phase Transitions

The $\alpha \rightarrow \beta \rightarrow \gamma$ phase transitions in inorganic perovskites involve symmetry breaking due to octahedral tilting and macroscopic strains. The primary octahedral tilt order parameters dictate group-subgroup relations between phases as a result of symmetry breaking due to atomic displacements while secondary strain order parameters measure the change in lattice vectors that accompany internal distortions. In this section, we apply the previously developed strain and displacement order parameters to describe the symmetry breaking associated with the experimentally observed $\alpha \rightarrow \beta \rightarrow \gamma$ phase sequence.

We begin by discussing the $\alpha \rightarrow \beta$ transition which corresponds to a lowering of symmetry from cubic to tetragonal. The tetragonal symmetry breaking of the lattice is associated with strains in the e_2-e_3 subspace as shown in Figure 4.3(a). Along e_3, the crystal is elongated along the z-direction while the xy-plane is compressed resulting in the z-oriented β_z phase. Symmetrically equivalent deformations distinguished by elongation of the y or x-axes are shown as the β_y and β_x variants. Hence there are three rotationally equivalent β-phase variants associated with the cubic α-phase reference.

The $\beta \rightarrow \gamma$ transition lowers the crystal point group symmetry from tetragonal to orthorhombic. Orthorhombic symmetry breaking of the lattice results from activation of shear modes, described by the e_4, e_5, and e_6 strain order parameters as discussed above. In discussing the $\beta \rightarrow \gamma$ transition, we will focus on a particular tetragonal β-phase variant, specifically β_z, but the same arguments apply for both β_x and β_y. For the case

of β_z, two γ_z-phase variants, γ_z^+ and γ_z^- result from the activation of the e_6 strain order parameter giving rise to shears in the xy-plane. As pictured in Figure 4.3(b), the positive and negative γ_z variants correspond to positive or negative e_6 amplitudes. The γ_z^+ and γ_z^--phases are related by a 90° rotation about the z-axis making them rotationally equivalent. If we were to consider the $\beta \rightarrow \gamma$ transitions for the other tetragonal variants, i.e. $\beta_y \rightarrow \gamma_y^{\pm}$ or $\beta_x \rightarrow \gamma_x^{\pm}$, orthorhombic symmetry breaking would correspond to activation of the e_5 and e_4 strain order parameters, respectively. Hence, each tetragonal phase results in two symmetrically equivalent γ-phase orientational variants, giving a total of six symmetrically equivalent orientational γ-phase variants that can emerge from a common cubic phase.

So far, we have described the macroscopic strain order parameters which uniquely identify a phase among the three experimentally observed phases (i.e. α, β, and γ), but which also allow one to distinguish between rotational variants of the same phase (i.e. β_x, β_y and β_z). Next we describe the symmetry-adapted displacement order parameters which give rise to corresponding tilt systems of the β and γ phases. In doing so, we will be able to distinguish translational variants of the different phases. Physically, this corresponds to distinguishing between a positive or negative rotation about a particular tilt axis.

We now identify a two-dimensional tilt subspace which contains all three experimentally observed phases for the $\alpha \rightarrow \beta_z \rightarrow \gamma_z^+$ transition. The ground state Pnma orthorhombic structure commonly observed in perovskites, for example the γ_z^+-phase variant, adheres to the $(00abb0)$ tilt pattern or $b^-b^-a^+$ in Glazer notation. The tilt components of this phase can be separated into two order parameters $\boldsymbol{\eta}_1 = (00a000)$, which describes in-phase tilts along the z-axis, and $\boldsymbol{\eta}_2 = (000bb0)$, which describes simultaneous and equivalent out-of-phase tilts along both the x- and y-axes. Together these order parameters span a two-dimensional tilt subspace pictured in Figure 4.3(c) which contains

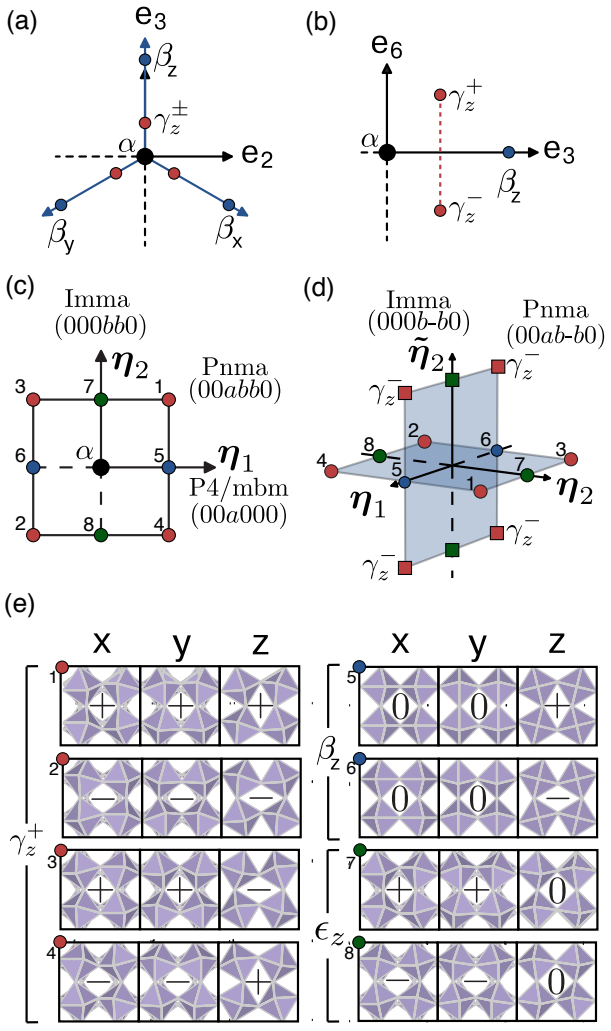

Figure 4.3: (a) Relevant strain order parameter subspaces for all rotational variants of the $\alpha \to \beta \to \gamma$ phase transitions. Points marked β represent symmetrically equivalent tetragonal variants, and γ points are symmetrically equivalent orthorhombic phases. In this work we focus on the strain subspace spanned by e_3-e_6 plotted in (b). (b) For the β_z variant there exists two rotationally equivalent orthorhombic variants, γ_z^+ and γ_z^-. (c) Two-dimensional tilt subspace spanned by the in-phase tilt order parameter $\boldsymbol{\eta}_1 = (00a000)$ which results in P4/mbm symmetry and the out-of-phase tilt order parameter $\boldsymbol{\eta}_2 = (000bb0)$ which results in Imma symmetry. When both $\boldsymbol{\eta}_1$ and $\boldsymbol{\eta}_2$ are nonzero, the symmetry is reduced to the Pnma space group. (d) The rotationally equivalent tilt order parameter $\tilde{\boldsymbol{\eta}}_2 = (000b\text{-}b0)$ is introduced to describe the Pnma γ_z^- variants which occur when both $\tilde{\boldsymbol{\eta}}_2$ and $\boldsymbol{\eta}_1$ are nonzero. (e) Examples of the translation variants corresponding to (c) where the $\pm$ sign indicates positive or negative tilts.

the α-phase at the origin, the β_z-phase along the $\boldsymbol{\eta}_1$ axis, and the γ_z^+-phase when both $\boldsymbol{\eta}_1$ and $\boldsymbol{\eta}_2$ are nonzero. Depictions of the tilt systems associated with $\boldsymbol{\eta}_1$ and $\boldsymbol{\eta}_2$ are pictured in Figure 4.3(e).

An additional unique tilt system also appears within this subspace, namely the Imma orthorhombic phase corresponding to nonzero values of the $\boldsymbol{\eta}_2$ order parameter. Although the Imma orthorhombic phase with $b^-b^-a^0$ tilts is not experimentally observed, we will refer to it as a hypothetical ϵ-phase when discussing energy landscapes within this subspace below.

While the strain order parameters distinguish symmetrically equivalent rotational variants as shown in Figures 4.3(a,b), the microscopic displacement order parameters $\boldsymbol{\eta}_1$ and $\boldsymbol{\eta}_2$ allow us to distinguish between symmetrically equivalent translational variants. For a particular strain state, there exist several equivalent internal displacements arising from the octahedral tilt patterns. That is, the crystal can sample translational variants through pure octahedral rotations, but rotational equivalents come along with a reorientation of the macroscopic strain.

For example, consider the z-oriented tetragonal β_z-phase. This phase is distinguished by a positive e_3 strain component and in-phase tilts along the z-axis, described by $\boldsymbol{\eta}_1$ in Figure 4.3(c). However a translational equivalent exists for tilts with negative tilt angle about the z-axis given by $-\boldsymbol{\eta}_1$. Hence for each tetragonal variant there exists two equivalent translational variants (e.g. $a^0a^0a^+$ and a^0a^0-a^+ for β_z). Likewise, for each orthorhombic γ-phase variant (e.g. γ_z^+=(+e_3,+e_6)) there exist four translational variants (e.g. tilt systems $b^-b^-a^+$, -b^--b^-a^+, -b^--b^--a^+, and b^-b^--a^+), as shown by the four red circles in Figure 4.3(c).

The tilt subspace presented in Figure 4.3(c) corresponds only to the α, β_z, and γ_z^+ variants from Figure 4.3(b). In order to describe the octahedral tilts of γ_z^-, we introduce the rotationally equivalent tilt order parameter $\tilde{\boldsymbol{\eta}}_2 = (000b\text{-}b0)$ as shown as an orthogonal

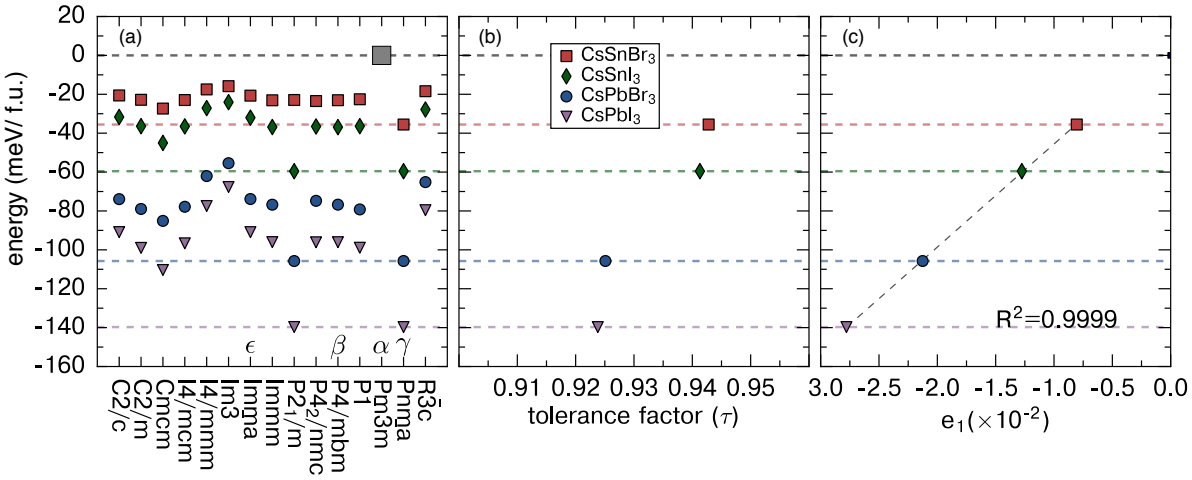

Figure 4.4: (a) Energies per formula unit (f.u.) of DFT relaxed tilt systems for $CsSnBr_3$, $CsSnI_3$, $CsPbBr_3$, and $CsPbI_3$ relative to the cubic reference within each chemistry. Pnma γ-phase ground states are found for all compounds. The low energy $P2_1/m$ structures are found to map to the Pnma structures with a tolerance of 0.01 Å. (b) Relative energies of the Pnma ground states as a function of tolerance factor in Equation 4.8. (c) Relative energies of the Pnma ground states plotted as a function of the $e_1 = \ln(V'/V)/\sqrt{3}$ strain order parameter as explained in the Section IIIB . The relative energy shows a linear relationship with e_1 indicating the significant role of volume contraction in perovskite stability.

axis in Figure 4.3(d). Here, the red squares indicate the four translational equivalents corresponding to γ_z^-.

In summary, there exist three rotational variants of the β-phase, each with two translational variants, for a total of six symmetrically equivalent tetragonal variants. For the γ-phase, there are six rotational equivalents, each with four translational variants, for a total of 24 symmetrically equivalent structures. The relationship between rotational and translational equivalents and the corresponding secondary strain order parameters are compiled in the supplemental materials.

4.3.4 A-Cation Displacement

The third degree of freedom explored in this study involves displacements of the A-site cation, in this case Cs. We probe the stability of the ground state orthorhombic A-cation ordering by displacing the Cs sub lattice within the ab plane according to the factor group of the crystal. Since the four Cs atoms are related by symmetry operations of the factor group, a displacement of one Cs atom dictates the displacement field of all atoms related by symmetry. By exploring the energy landscape associated with displacements that maintain Pnma symmetry, we are able to determine if there exist unexplored local minima with respect to Cs displacements.

4.4 Results

4.4.1 Tilt System Energy and Volume

In Figure 4.4(a) we present the DFT energies obtained after full geometric optimization of all 14 possible tilt systems including the reference cubic α-phase structure. We find that, among all chemistries, the orthorhombic γ-phase tilt system $b^-b^-a^+$ always has the lowest energy. This finding agrees with experimental observations of γ-phase ground states upon cooling from the high temperature α-phase in $CsSnI_3$, $CsSnBr_3$, $CsPbI_3$, and $CsPbBr_3$. [49, 132, 8, 133, 134]

In perovskite materials, the tendency to distort from the cubic α-phase has been shown to correlate with the size of the A-site cation relative to the size of the cuboctahedral void in which it resides. The Goldschmidt tolerance factor quantifies the degree of under or over coordination of the A-site as:

$$\tau = \frac{r_{\mathrm{A}} + r_{\mathrm{X}}}{\sqrt{2}(r_{\mathrm{B}} + r_{\mathrm{X}})} = \sqrt{2}\left(\frac{r_{\mathrm{A}}}{a} + \frac{r_X}{a}\right). \tag{4.8}$$

where r_A, r_B, and r_X refer to the ionic radii of the A, B and X sites of a perovskite, respectively, and a refers to the cubic lattice parameter. For compounds with perfectly coordinated A-site cations, $\tau = 1$, and the cubic α-phase is typically favored. However, for materials with under-coordinated A-sites, $\tau < 1$, and structural distortions associated with octahedral tilts are expected to occur.

Figure 4.4(b) depicts the relative energies of the γ-phase ground states (where each chemistry is referenced to the energy of the cubic α-phase) as a function of the Goldschmidt tolerance factor. In the case of halide perovskites, ionic radii for the group VI divalent cations such as Pb^{2+} and Sn^{2+} are not well established. [144, 27] Hence, we instead calculate τ using the the second equality in Equation 4.8, with r_A and r_X given by the known Shannon radii [144] and a given by the DFT calculated cubic lattice parameter. In Figure 4.4(b), the tolerance factor moderately correlates with the relative energy of the ground state γ-phase systems across each chemistry.

While the tolerance factor serves as a proxy to predict the stabilization of the γ-phase based only upon α-phase properties, we observe that the trend in energy of the ground state γ-phase relative to the cubic high temperature α-phase follows an almost perfect linear relationship with the volumetric e_1 strain order parameter as presented in Figure 4.4(c). In agreement with the predictions based on tolerance factor, Figure 4.4(c) shows that Pb-based compounds undergo larger volume contraction resulting in larger stabilization energies relative to the Sn-based counterparts. In addition to comparisons between chemistries, the volumetric e_1 strain order parameter also aids in the analysis of tilt systems within a single chemistry. Remarkably, the correlation between relative tilt system energy (as referenced to the cubic α-phase) and e_1 persists among all tilt systems as shown in Figure 4.5. Here, we observe that the γ-phase ground state corresponds to the most volume-decreasing tilt system, thereby resulting in the lowest energy. Together, Figures 4.4 and 4.5 suggest a unified description of tilt system stability in

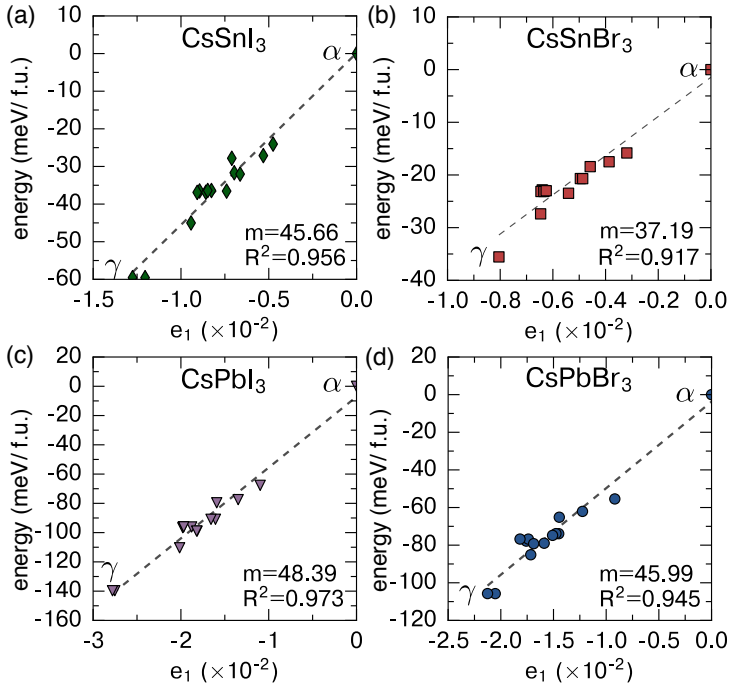

Figure 4.5: Energy per formula unit (f.u.) of DFT relaxed tilt systems vs e_1 for (a) $CsSnI_3$, (b) $CsSnBr_3$, (c) $CsPbI_3$, and (d) $CsPbBr_3$ relative to the cubic reference within each chemistry. All chemistries show a linear relationship between the relative energy (with respect to the cubic phase) and the e_1 invariant of the Hencky strain metric. The relationship between e_1 and the ratio of the volumes between the deformed structure, V, and the reference structure V_0 is given by $e_1 = \ln(V/V_0)/\sqrt{3}$.The slope (m) is given in meV/(0.01 unit e_1) and R^2 is the coefficient of determination of the best fit line. The ground state γ-phase is the lowest energy and most volume decreasing tilt system for each chemistry.

ionic all-inorganic halide perovskites where, within a certain chemistry, the most volume decreasing tilt system corresponds to the most stable phase, and between chemistries, the volume contraction of the ground state phase dictates the energy difference from the high temperature α-phase. Importantly, the energy differences between the γ-phase ground state and the α-phase cubic reference for each chemistry are consistent with the observed orthorhombic to tetragonal transition temperatures of this perovskite series. [42, 135, 43, 8, 50]

4.4.2 Strain/Tilt Order Parameter Decomposition of DFT Optimized Tilt Systems

In order to study the coupling between tilt modes and lattice strains, we performed DFT relaxations with tight force convergence criteria for a subset of the tilt systems considered in Figure 4.4(a), including Imma (ϵ), P4/mbm (β), and Pnma (γ). Figure 4.6 shows decompositions of the lattice strains in terms of symmetrized strain order parameters e_3 and e_6 as well as a decomposition of activated tilt modes in terms of collective displacement modes $\boldsymbol{\eta}_1 = (00a000)$, $\boldsymbol{\eta}_2 = (000bb0)$, and $\tilde{\boldsymbol{\eta}}_2 = (000b\text{-}b0)$ for $CsSnBr_3$, $CsSnI_3$, $CsPbBr_3$, and $CsPbI_3$. The tilt mode decompositions in Figure 4.6(b-e) are plotted using the same coordinate system described in Figures 4.3(c,d) where translationally equivalent structures belong to the same plane while rotationally equivalent structures belong to an orthogonal plane. The length of each displacement order parameter axis is normalized to $\boldsymbol{\eta}_1 = \boldsymbol{\eta}_2 = \tilde{\boldsymbol{\eta}}_2 = 1$ which corresponds to a displacement $||\mathbf{d}(\eta_1 = 1)|| = ||\mathbf{d}(\eta_2 = 1)|| = ||\mathbf{d}(\tilde{\boldsymbol{\eta}}_2 = 1)|| = 4.088$Å where $\mathbf{d}$ is defined in Equation 4.1.

As is clear in Figure 4.6, the tetragonal β-phase (P4/mbm, $a^0a^0a^+$), represented as blue circles, has large $\boldsymbol{\eta_1}$ amplitudes as expected due to the presence of in-phase tilts. Additionally the tetragonal β-phase structures show large positive e_3 strains, indicating a compression in the xy-plane and expansion along the z-axis (Figure 4.2(b,d)) as a result of large in-phase tilting.

The orthorhombic ϵ-phase (Imma, $b^-b^-a^0$), represented by green symbols, undergoes large $\boldsymbol{\eta}_2$ or $\tilde{\boldsymbol{\eta}}_2$ amplitudes, depending on the rotational variant. Its unit cell undergoes negative e_3 strains and moderate e_6 strains. A negative e_3 strain indicates expansion of the xy-plane as shown in Figure 4.2(d). Unlike the tetragonal β-phase which contracts in the xy-plane ($e_3 > 0$) due to in-phase tilts about the z-axis, the ϵ phase has no tilts along the z-axis and exhibits expansion of the xy-plane ($e_3 < 0$).

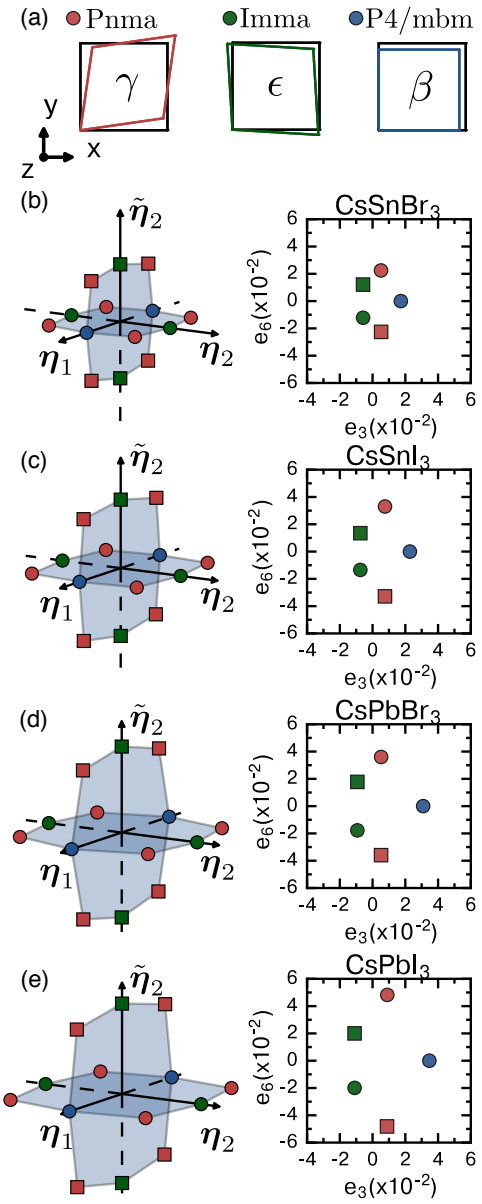

Figure 4.6: (a) Strains associated with the (00$a$$b$$b$0), (000$b$$b$0), and (00$a$000) are shown as 2D projections into the xy-plane. Strains are enlarged by a factor of three for clarity. Amplitude of tilt modes (left) and strain modes e_3 and e_6 (right) for (b) $CsSnBr_3$, (c) $CsSnI_3$, (d) $CsPbBr_3$, (e) $CsPbI_3$. Order parameters $\boldsymbol{\eta}_1$ and $\boldsymbol{\eta}_2$ represent the tilt systems (00a000) and (000$b$$b$0) respectively, while $\tilde{\boldsymbol{\eta}}_2$ denotes (000$b$$-b$0), the rotationally equivalent axis to (000$b$$b$0).

Interestingly, two simultaneous out-of-phase tilts (i.e. $\boldsymbol{\eta}_2$ or $\tilde{\boldsymbol{\eta}}_2$ are nonzero) are always accompanied by shear strains represented, in this case, as the e_6 strain order parameter.

The strain decompositions in the right column of Figure 4.6(b-e) illustrate that the sign of e_6 depends on the rotational equivalent specified by the octahedral tilt order parameter either $\boldsymbol{\eta}_2$ or $\tilde{\boldsymbol{\eta}}_2$. The corresponding strains are illustrated in Figure 4.2(d) where a change in the sign of e_6 corresponds to a 90° rotation of the lattice about the z-direction.

The orthorhombic γ-phase (Pnma, $b^-b^-a^+$) structures express large amplitudes for both the $\boldsymbol{\eta}_1$ and $\boldsymbol{\eta}_2$ (or $\boldsymbol{\eta}_1$ and $\tilde{\boldsymbol{\eta}}_2$ for the rotational variants) as well as large e_6 strains and small e_3 strains. Exaggerated illustrations of the strains associated with the γ (Pnma), ϵ (Imma), and β (P4/mbm) phases are pictured in Figure 4.6(a)

Lastly, we observe from Figures 4.6(b,c,d,e) that the magnitudes of the tilt modes and strains generally increase as a function of relative stability from $CsSnBr_3$, $CsSnI_3$, $CsPbBr_3$, to $CsPbI_3$, similar to the correspondence between e_1 and energy from Figure 4.4(c). This further illustrates the coupling between strain and tilts, where larger amplitude octahedral tilts induce larger macroscopic strains in the crystal. Furthermore, the most volume decreasing system, $CsPbI_3$, exhibits the largest strains, the largest tilt mode amplitudes and the deepest stabilization energies, while for the least volume decreasing compound, $CsSnBr_3$, the opposites hold true.

4.4.3 Energy Landscape of Octahedral Tilt Order Parameters

Now we explore the energy landscape associated with pure octahedral tilts and Cs displacements for $CsSnBr_3$ and $CsPbI_3$ as shown in Figure 4.7(a,b). $CsSnBr_3$ and $CsPbI_3$ were chosen since they represent the extremes in terms of volume contraction, tilt amplitude, and stabilization energies as previously discussed. The horizontal and vertical axes in Figure 4.7 correspond to the subspace first presented in Figure 4.3(c) and have been normalized such that a value of 1 corresponds to a displacement, $||\mathbf{d}(\eta_1 = 1)|| = ||\mathbf{d}(\eta_2 = 1)|| = 4.088$Å where $\mathbf{d}$ is defined in Equation 4.1. The three

rows of Figure 4.7 represent the same energy landscape at the equilibrium (i) α-cubic strain, (ii) β-tetragonal strain, and (iii) γ-orthorhombic strain, which are represented by the inset in the middle of Figure 4.7. Furthermore, within each row, the first column of Figure 4.7(a,b) fixes the Cs positions to the center of the A-site cage, while in the second column the Cs atoms are allowed to relax to their minimum energy positions. By investigating the octahedral tilt energy landscape at different strains and with/without Cs displacements, we are able to disentangle the effects of octahedral tilting, A-site displacements, and strain on perovskite tilt system stability.

We begin by studying the octahedral tilt energy landscape at the reference cubic strain in the first row of Figure 4.7(a,b)(i). Interestingly as seen in the fixed Cs columns of Figure 4.7(a,b)(i) the energy landscape within the tilt subspace is nearly isotropic with respect to any combination of imposed tilts. Both $\boldsymbol{\eta}_1$ and $\boldsymbol{\eta}_2$ octahedral tilts lower the energy of the crystal relative to the cubic reference. Hence, the cubic crystal, represented at the origin of the energy landscape, is dynamically unstable within this subspace. In harmonic phonon dispersions, these instabilities manifest as imaginary frequency vibrational modes at the R- and M-points of the Brillouin zone. [127] The constant energy contours are almost perfectly isotropic with a slight preference for the $(00a000)$ $a^0a^0a^+$ tilt system. Thus, based solely on halide displacements, all of the considered tilt patterns are nearly degenerate in energy, and the primary tilt order parameters are inadequate to distinguish the ground state phases. This raises the question of why the γ-phase is stable as a ground state as previously demonstrated in Figure 4.4(a).

The answer lies in the position of the A-site cation, in this case the Cs^+ ion. While the left columns of Figure 4.7(a,b)(i) are calculated at fixed strain, halide displacement, and Cs position, the right columns represent the energy surface after only the Cs atoms are allowed to relax to their minimum energy positions. Upon relaxation of the A-site cation, the energy surfaces exhibit minima at each of the Pnma translational equivalents

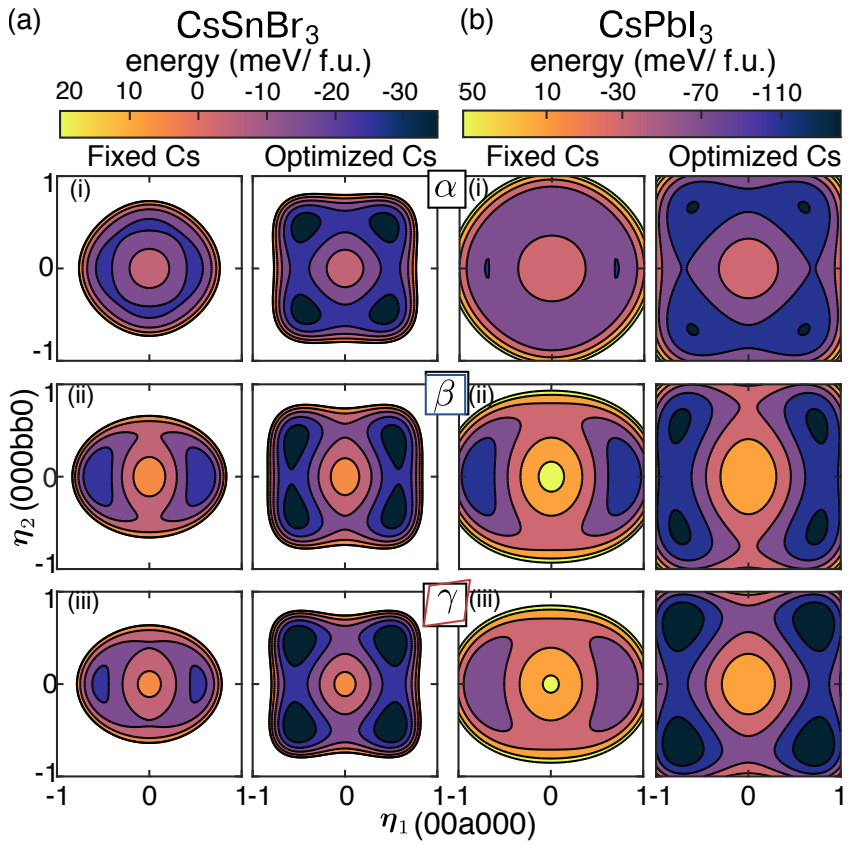

Figure 4.7: Energy surfaces for (a) $CsSnBr_3$ and (b) $CsPbI_3$ plotted as heat maps for the 2D tilt space spanned by $\boldsymbol{\eta}_2 = (000bb0)$ on the vertical axis and $\boldsymbol{\eta}_1 = (00a000)$ on the horizontal axis. Energies are relative to the energy of the cubic reference in each chemistry and are normalized per one perovskite formula unit (f.u.). The order parameter axes are normalized such that $||\mathbf{d}(\eta_1 = 1)|| = ||\mathbf{d}(\eta_2 = 1)|| = 4.088$Å where $\mathbf{d}$ is defined in Equation 4.1. Left column represents static calculations at (i) cubic $Pm\bar{3}m$ α-phase strain, (ii) tetragonal P4/mbm β-phase strain, and (iii) orthorhombic Pnma γ-phase strains. Right column indicates the energy at the same strain after optimizing only the Cs^+ cation positions. Only after cation displacements are the Pnma ground state tilt systems stabilized.

as shown in the right columns of Figure 4.7(a,b)(i) for both $CsSnBr_3$ and $CsPbI_3$. Hence at the reference cubic strain, both the α-phase, located at a local maximum, and the β-phase, located at a saddle point, are unstable with respect to a combination of octahedral tilts and A-site displacements.

Up to this point the calculated energy surface is of the crystal in the reference strain of the high temperature cubic phase; however at intermediate and low temperatures, the

average strain state of the crystal changes to tetragonal and orthorhombic. Therefore, it is instructive to investigate the same octahedral tilt energy landscapes at the equilibrium strains of the low symmetry structures.

Next, in Figure 4.7(a,b)(ii), we recalculate the same octahedral tilt energy landscape at the equilibrium tetragonal β-phase strain corresponding to the $a^0a^0a^+$ tilt system (pictured as the third panel in Figure 4.6(a)). Before Cs optimization, there exist minima at the β-phase tilt systems $(\boldsymbol{\eta}_1^{\beta}, 0)$ while the ϵ, α, and γ phases are all unstable. After the Cs positions are optimized, (right columns of Figure 4.7(a,b)(ii)), the γ-phase tilt systems are again stabilized at the local minima $(\pm\boldsymbol{\eta}_1^{\gamma}, \pm\boldsymbol{\eta}_2^{\gamma})$. The main effect of fixing the equilibrium β-phase lattice parameters is the reduction in energy of the β-phase saddle points after Cs optimization relative to the ϵ-phase saddle point. The significant energy reduction associated with Cs displacements is enough to stabilize the γ-phase even at β-phase lattice parameters.

Finally, Figure 4.7(a,b)(iii) shows the octahedral tilt energy landscape at the ground state γ-phase strain. Interestingly, before Cs optimization the experimentally observed tetragonal β-phase (P4/mbm $a^0a^0a^+$ tilt system) is slightly stabilized at $(\boldsymbol{\eta}_1^{\beta}, 0)$ as shown in left columns of Figure 4.7(a,b)(iii). However, once Cs cation positions are optimized, (right columns of Figure 4.7(a,b)(iii)), we once again observe the stabilization of the γ-phase tilt system at minima located at $(\pm\boldsymbol{\eta}_1^{\gamma}, \pm\boldsymbol{\eta}_2^{\gamma})$. At the ground state equilibrium lattice parameters, the energy of the β-phase saddle point is reduced relative to the ϵ-phase saddle point.

By recalculating the energy landscape with respect to octahedral tilts at the strains of the α, β, and γ phases, we have shown that the main effect of strain is to alter the relative energies of the β and ϵ saddle points. Furthermore, through selective optimization of the Cs positions, we have shown that a strong coupling between octahedral tilts and Cs displacements is the main source for stabilization of the γ-phase regardless of the strain

state of the crystal.

4.4.4 A-cation Off-Centering in γ-phase Ground States

The effect of Cs optimization in Figure 4.7 demonstrates the importance of a strong coupling between octahedral tilts and A-site displacements in stabilizing γ-phase ground states. According to bond valence arguments, A-cation displacements originate from a minimization of unfavorable Coulomb interactions in the crystal. [145] Since Cs^+ off-centering plays such a large role in the stabilization of the γ-phase ground state, we also explored the energy landscape as a function of cooperative Cs^+ displacements in the ground state γ-phase structure.

Figure 4.8(a) depicts the $z = 0$ and $z = 1/2$ slices of the γ-phase ground state structure within the orthorhombic primitive cell. In the ground state Pnma γ-phase, the Cs atoms displace from the ideal cubic positions (shown as dashed circles) to their minimum energy positions (indicated by filled teal circles). Using the factor group of the structure, we find symmetrically equivalent displacements of the Cs asymmetric unit represented as the unit axes in Figure 4.8(a). In this way we map out the energy landscape of Cs displacements that maintain Pnma symmetry as shown in Figure 4.8(b,c) for $CsSnBr_3$ and $CsPbI_3$, respectively. Even for small Cs displacements away from the minimum energy positions, the energy penalty for Cs displacements is quite large (Figure 4.8(b,c)); therefore, we rule out the possibility of any other local minima for Cs orderings in the Pnma ground state.

4.5 Discussion and Conclusions

We have confirmed Pnma γ-phase ground states among the 14 distinct tilt systems for $CsSnBr_3$, $CsSnI_3$, $CsPbBr_3$, and $CsPbI_3$ through full geometric optimization using

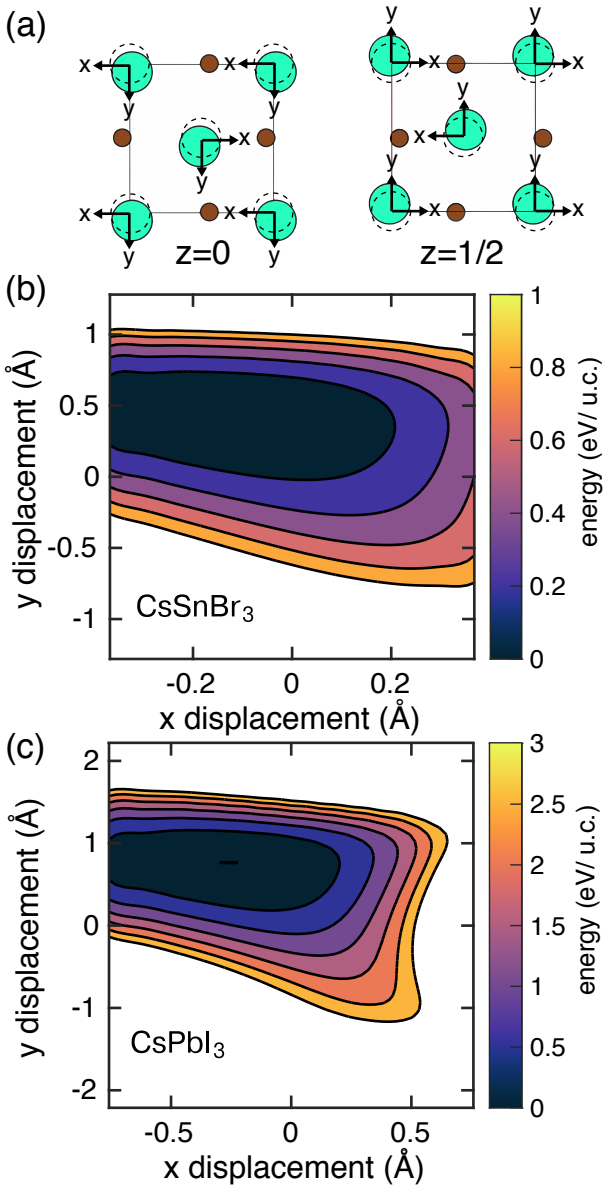

Figure 4.8: (a) z=0 and z=1/2 sections of the orthorhombic primitive cell of the Pnma ground state. Dashed circles represent high symmetry points of the orthorhombic lattice which correspond to the ideal A-site positions in the cubic crystal and the coordinate axes represent displacements from these points that respect that factor group of the crystal. (b,c) Energy contours with respect to cation displacements as defined above for $CsSnBr_3$ and $CsPbI_3$, respectively. Energies are relative to the relaxed ground state energy and are presented as energy per unit cell (u.c.) which contains 20 atoms. All displacements raise the energy thereby ruling out any other local minima in terms of cation displacements that maintain Pnma symmetry.

DFT. We find that all tilt systems lower the energy of the crystal with respect to the high temperature cubic α-phase. Furthermore, by calculating the Born-Oppenheimer energy landscape with respect to symmetry adapted collective displacement modes at various strain states and with/without Cs displacements, we were able to disentangle the energetic contributions of these three degrees of freedom. Notably, the coupling between tilts and A-site displacements are necessary to stabilize the γ-phase ground state tilt systems, while strain coupling lowers the β-phase saddle point energy relative to that of the ϵ-phase saddle point.

The next important result is that the cubic and tetragonal phases are unstable as opposed to metastable. The presence of continuous energy lowering distortions in the cubic and tetragonal phase means that harmonic phonon theory is inadequate to describe the vibrational thermodynamics of these systems. Interestingly, we observe nearly isotropic instabilities with respect to pure octahedral tilts associated with the R_4^+ and M_3^+ irreps of the cubic $Pm\bar{3}m$ space group. Only upon selective relaxation of the Cs^+ A-cation are Pnma phases stabilized. The configuration of the Cs cations is fully dictated by distortions of the octahedral cage, and we find no other Cs displacement patterns with lower energy.

Upon full relaxations, tilt instabilities are always accompanied by macroscopic strains which we decomposed into symmetrized strain order parameters using the Hencky strain metric. We found that the volumetric strain order parameter e_1 correlates with the relative energy of $CsBX_3$ perovskites. Interestingly, Pb based compounds show a greater degree of volume contraction as well as octahedral tilting. In addition to the geometrical aspects of A-site under coordination, the trend that Pb-containing compounds show deeper stabilization energies for octahedral tilting likely originates due to the higher band gap of Pb compounds indicating a higher degree of ionicity. [146, 43] The degree of ionicity is known to play a role in the degree of octahedral tilting in oxide per-

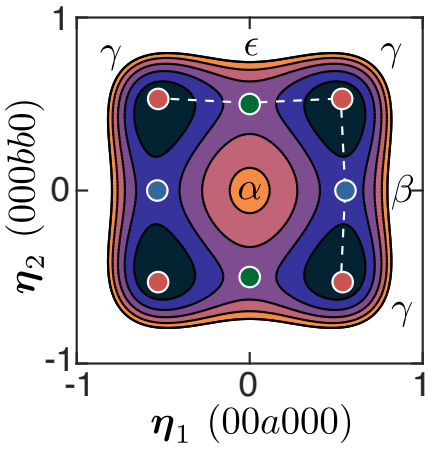

Figure 4.9: Enlarged energy surface with respect to $\boldsymbol{\eta}_1$ and $\boldsymbol{\eta}_2$ at the ground state orthorhombic Pnma strain from Figure 4.7(a)(iii) where Cs^+ positions have been optimized. Circles mark the location of minima or saddle points; red indicates the $b^-b^-a^+$ tilt system occurring at the minimum ($\boldsymbol{\eta}_1^\gamma$,$\boldsymbol{\eta}_2^\gamma$), green $b^-b^-a^0$ at (0,$\boldsymbol{\eta}_2^\epsilon$) and blue $b^0b^0a^+$ at ($\boldsymbol{\eta}_1^\beta$,0). At the orthorhombic ground state strain, we observe deeper saddle points for the P4/mbm tilt system ($\pm\boldsymbol{\eta}_1^\beta$,0) as opposed to the Imma tilt system (0,$\pm\boldsymbol{\eta}_2^\epsilon$) which follows the experimentally observed phase sequence from the ground state orthorhombic γ-phase to tetragonal P4/mbm β-phase at intermediate temperatures to the high temperature $Pm\bar{3}m$ cubic α-phase.

ovskites where more covalent metal-oxygen bonds stabilize 180° degree O−M−O bond angles. [147, 148, 149] For instance, the metal, ReO_3, comprised of corner connected octahedra maintains 180° bond angles [148, 150] despite the lack of a central A-site cation (leading to a tolerance factor of zero). Therefore, higher ionicity leads to weaker Pb−I−Pb bonds in Pb-based compounds resulting in larger octahedral tilting distortions relative to Sn-based compounds studied here. In addition, stronger relative stabilization energies for the Pb-containing compounds correlates with the experimentally observed orthorhombic to tetragonal phase transition temperatures of $CsMX_3$ halide perovskites where Sn-containing compounds exhibit smaller bandgaps and lower transition temperatures than the Pb-containing counterparts.

The cubic α-phase and tetragonal β-phase of inorganic $CsMX_3$ perovskites are dynamically unstable as demonstrated by the energy landscape with respect to octahedral

tilt order parameters and Cs^+ displacements. We reproduce the energy landscape with respect to octahedral tilts at the orthorhombic γ phase strain in Figure 4.9 for $CsSnBr_3$. The experimental high temperature α-phase and the intermediate temperature β-phase reside at a local maximum and saddle point, respectively, indicating that these phases are unstable. Two important aspects of this energy landscape are that (1) the γ-phase is only stabilized after optimization of the Cs positions and (2), at the equilibrium γ-phase lattice parameters, the β-phase saddle point has a lower energy compared to the ϵ-phase saddle point. The lower energy barrier between γ-phase variants passing through the β-phase saddle points suggest that this is the more favorable transition pathway as the structure is heated from low temperature. The phase progression from γ to β likely occurs as out-of-phase octahedral rotations oscillate between positive and negative rotations corresponding to oscillations between γ phase translational and orientational variants through the β-phase. As the temperature is increased, sufficient thermal energy allows the system to sample all symmetrically equivalent structures resulting in an average cubic structure.

The complexity of the Born-Oppenheimer energy surface at zero Kelvin underscores the many avenues for anharmonic and dynamic fluctuations at high temperature. While high temperature halide perovskites adopt the cubic phase, large anharmonic vibrational excitations are likely occurring dynamically within local environments. For instance, polar fluctuations involving head-to-head displacements of the Cs cation, have been observed in hybrid and inorganic lead bromide perovskites, [128] large anharmonic halide displacements contribute to a fluctuating lattice,[18, 124, 125, 126, 127] and dynamically disordered metal atoms have been shown to increase with temperature [129, 42]. More specifically, inelastic x-ray scattering experiments on hybrid perovskites show that phonon modes corresponding to the R_4^+ and M_3^+ irreps are substantially populated in the cubic crystal indicating non-cubic local environments. [18] Moreover, structural studies

on inorganic cesium lead halide nanocrystals have shown that increasing populations of twinned γ-phase nano domains can appear as higher symmetry phases from XRD further complicating the picture of local symmetry breaking at high temperature. [151]

The dynamic local environment of perovskites at high temperatures remains unclear, and accurate simulations of the lattice dynamics of these systems are critical to understand the impact on electronic properties. However, due to the dynamically unstable nature of the intermediate temperature tetragonal β-phase and high temperature cubic α-phase, models of the lattice dynamics of inorganic halide perovskites cannot be adequately handled within a harmonic approximation. Instead anharmonic vibrational hamiltonians are needed to model structural phase transitions. [64] We have identified the relevant strain and displacement order parameters to guide the construction and fitting of DFT-based anharmonic vibrational effective hamiltonians in order to build accurate lattice dynamics models of inorganic perovskite materials.

In conclusion, we have shown that a careful examination of the coupling between strain, tilts, and Cs^+ displacements is needed to explain the nature of structural phase transitions in inorganic halide perovskites. However, from a macroscopic standpoint, it is simply the degree of volume contraction that dictates the stability of the Pnma ground state perovskite tilt system. Finally, we reiterate that the intermediate and high temperature phases are both dynamically unstable (i.e. they appear at saddle points or local maxima with respect to tilt order parameters) which gives rise to a deformable and polarizable lattice that is essential to the optoelectronic properties of halide perovskites.

4.6 Secondary Strain Order Parameters for Perovskite Tilt Transitions

For each 14 unique tilt system we compile its rotational and translational equivalents below along with the symmetry-allowed secondary strain order parameters. Given a direction in the six dimensional tilt space corresponding to a particular tilt system (e.g. $\boldsymbol{\eta} = (a00000)$ P4/mbm) the symmetry equivalent tilt order parameters are found by applying the symmetry operations of the 2×2×2 cubic perovskite factor group as $\boldsymbol{\eta}' = \mathbf{M}^{\eta}(g)\boldsymbol{\eta}$. The parent factor group contains several distinct types of symmetry operations including pure translations, rotations/reflections, and glide/screw operations. Pure translations applied to $\boldsymbol{\eta}$ result in translational equivalents that are grouped between single horizontal lines in the tables below. For example, in the P4/mbm space group, $\boldsymbol{\eta} = (a00000)$ and $\boldsymbol{\eta} = (-a00000)$ are translational equivalents. Rotations, reflections, glide, or screw operations result in rotational equivalents which have their own translation equivalents. For example $\boldsymbol{\eta} = (0a0000)$ and $\boldsymbol{\eta} = (00a000)$ are rotational equivalents for the P4/mbm tilt system. In the tables below, single lines separate rotational equivalents. The secondary strain order parameters are found by applying the Reynold's operator of the primary order parameter subgroup as described in the main text. Since strains are a macroscopic property, they are invariant to microscopic translations resulting in just one secondary strain order for each group of translational tilt equivalents.

Table 4.2: 127 P4/mbm

M_3^+ *(a,b,c)*	R_4^+ *(a,b,c)*	*Strain* $(e_1, e_2, e_3, e_4, e_5, e_6)$
(a,0,0)	(0,0,0)	(A,$\frac{\sqrt{3}}{2}$B,$-\frac{1}{2}$B,0,0,0)
(-a,0,0)	(0,0,0)	
(0,a,0)	(0,0,0)	(A,$\frac{\sqrt{3}}{2}$B,$\frac{1}{2}$B,0,0,0)
(0,-a,0)	(0,0,0)	
(0,0,a)	(0,0,0)	(A,0,B,0,0,0)
(0,0,-a)	(0,0,0)	

Table 4.3: 139 I/mmm

M_3^+ *(a,b,c)*	R_4^+ *(a,b,c)*	*Strain* $(e_1, e_2, e_3, e_4, e_5, e_6)$
(0,a,a)	(0,0,0)	(A,$\frac{\sqrt{3}}{2}$B,$-\frac{1}{2}$B,0,0,0)
(0,a,-a)	(0,0,0)	
(0,-a,-a)	(0,0,0)	
(0,-a,a)	(0,0,0)	
(a,0,a)	(0,0,0)	(A,$\frac{\sqrt{3}}{2}$B,$\frac{1}{2}$B,0,0,0)
(a,0,-a)	(0,0,0)	
(-a,0,-a)	(0,0,0)	
(-a,0,a)	(0,0,0)	
(a,a,0)	(0,0,0)	(A,0,B,0,0,0)
(a,-a,0)	(0,0,0)	
(-a,-a,0)	(0,0,0)	
(-a,a,0)	(0,0,0)	

Table 4.4: 204 Im$\bar{3}$

M_3^+ *(a,b,c)*	R_4^+ *(a,b,c)*	*Strain* $(e_1, e_2, e_3, e_4, e_5, e_6)$
(a,a,a)	(0,0,0)	(A,0,0,0,0,0)
(a,-a,-a)	(0,0,0)	
(-a,a,-a)	(0,0,0)	
(-a,-a,a)	(0,0,0)	
(-a,-a,-a)	(0,0,0)	(A,0,0,0,0,0)
(-a,a,a)	(0,0,0)	
(a,-a,a)	(0,0,0)	
(a,a,-a)	(0,0,0)	

Table 4.5: 71 Immm

M_3^+ *(a,b,c)*	R_4^+ *(a,b,c)*	*Strain* $(e_1, e_2, e_3, e_4, e_5, e_6)$
(a,b,c)	(0,0,0)	(A,B,C,0,0,0)
(a,-b,-c)	(0,0,0)	
(-a,b,-c)	(0,0,0)	
(-a,-b,c)	(0,0,0)	
(-a,-c,-b)	(0,0,0)	(A,B,C,0,0,0)
(-a,c,b)	(0,0,0)	
(a,-c,b)	(0,0,0)	
(a,c,-b)	(0,0,0)	
(c,a,b)	(0,0,0)	(A,B,C,0,0,0)
(c,-a,-b)	(0,0,0)	
(-c,a,-b)	(0,0,0)	
(-c,-a,b)	(0,0,0)	
(-c,-b,-a)	(0,0,0)	(A,B,C,0,0,0)
(-c,b,a)	(0,0,0)	
(c,-b,a)	(0,0,0)	
(c,b,-a)	(0,0,0)	
(b,c,a)	(0,0,0)	(A,B,C,0,0,0)
(b,-c,-a)	(0,0,0)	
(-b,c,-a)	(0,0,0)	
(-b,-c,a)	(0,0,0)	
(-b,-a,-c)	(0,0,0)	(A,B,C,0,0,0)
(b,a,-c)	(0,0,0)	
(b,-a,c)	(0,0,0)	
(-b,a,c)	(0,0,0)	

Table 4.6: 140 I4/mcm

M_3^+ *(a,b,c)*	R_4^+ *(a,b,c)*	*Strain* $(e_1, e_2, e_3, e_4, e_5, e_6)$
(0,0,0)	(a,0,0)	(A,$\frac{\sqrt{3}}{2}$B,-$\frac{1}{2}$B,0,0,0)
(0,0,0)	(-a,0,0)	
(0,0,0)	(0,a,0)	(A,$\frac{\sqrt{3}}{2}$B,$\frac{1}{2}$B,0,0,0)
(0,0,0)	(0,-a,0)	
(0,0,0)	(0,0,a)	(A,0,B,0,0,0)
(0,0,0)	(0,0,-a)	

Table 4.7: 74 Imma

M_3^+ *(a,b,c)*	R_4^+ *(a,b,c)*	*Strain* $(e_1, e_2, e_3, e_4, e_5, e_6)$
(0,0,0)	(0,a,a)	(A,$\frac{\sqrt{3}}{2}$B,$-\frac{1}{2}$B,C,0,0)
(0,0,0)	(0,-a,-a)	
(0,0,0)	(0,a,-a)	(A,$\frac{\sqrt{3}}{2}$B,$-\frac{1}{2}$B,C,0,0)
(0,0,0)	(0,-a,a)	
(0,0,0)	(a,0,a)	(A,$\frac{\sqrt{3}}{2}$B,$\frac{1}{2}$B,0,C,0)
(0,0,0)	(-a,0,-a)	
(0,0,0)	(a,0,-a)	(A,$\frac{\sqrt{3}}{2}$B,$\frac{1}{2}$B,0,C,0)
(0,0,0)	(-a,0,a)	
(0,0,0)	(a,a,0)	(A,0,B,0,0,C)
(0,0,0)	(-a,-a,0)	
(0,0,0)	(a,-a,0)	(A,0,B,0,0,C)
(0,0,0)	(-a,a,0)	

Table 4.8: 167 R$\bar{3}$c

M_3^+ *(a,b,c)*	R_4^+ *(a,b,c)*	*Strain* $(e_1, e_2, e_3, e_4, e_5, e_6)$
(0,0,0)	(a,a,a)	(A,0,0,$\frac{\sqrt{3}}{3}$B,$\frac{\sqrt{3}}{3}$B,$\frac{\sqrt{3}}{3}$B)
(0,0,0)	(-a,-a,-a)	
(0,0,0)	(-a,a,a)	(A,0,0,$-\frac{\sqrt{3}}{3}$B,$\frac{\sqrt{3}}{3}$B,$\frac{\sqrt{3}}{3}$B)
(0,0,0)	(a,-a,-a)	
(0,0,0)	(a,-a,a)	(A,0,0,$\frac{\sqrt{3}}{3}$B,$-\frac{\sqrt{3}}{3}$B,$\frac{\sqrt{3}}{3}$B)
(0,0,0)	(a,-a,a)	
(0,0,0)	(a,a,-a)	(A,0,0,$\frac{\sqrt{3}}{3}$B,$\frac{\sqrt{3}}{3}$B,$-\frac{\sqrt{3}}{3}$B)
(0,0,0)	(-a,-a,a)	

Table 4.9: 12 C2/m

M_3^+ *(a,b,c)*	R_4^+ *(a,b,c)*	*Strain* $(e_1, e_2, e_3, e_4, e_5, e_6)$
(0,0,0)	(0,a,b)	(A,B,C,D,0,0)
(0,0,0)	(0,-a,-b)	
(0,0,0)	(0,a,-b)	(A,B,C,D,0,0)
(0,0,0)	(0,-a,b)	
(0,0,0)	(0,b,a)	(A,B,C,D,0,0)
(0,0,0)	(0,-b,-a)	
(0,0,0)	(0,b,-a)	(A,B,C,D,0,0)
(0,0,0)	(0,-b,a)	
(0,0,0)	(a,0,b)	(A,B,C,0,D,0)
(0,0,0)	(-a,0,-b)	
(0,0,0)	(a,0,-b)	(A,B,C,0,D,0)
(0,0,0)	(-a,0,b)	
(0,0,0)	(b,0,a)	(A,B,C,0,D,0)
(0,0,0)	(-b,0,-a)	
(0,0,0)	(b,0,-a)	(A,B,C,0,D,0)
(0,0,0)	(-b,0,a)	
(0,0,0)	(a,b,0)	(A,B,C,0,0,D)
(0,0,0)	(-a,-b,0)	
(0,0,0)	(a,-b,0)	(A,B,C,0,0,D)
(0,0,0)	(-a,b,0)	
(0,0,0)	(b,a,0)	(A,B,C,0,0,D)
(0,0,0)	(-b,-a,0)	
(0,0,0)	(b,-a,0)	(A,B,C,0,0,D)
(0,0,0)	(-b,a,0)	

Table 4.10: 15 C2/c

M_3^+ *(a,b,c)*	R_4^+ *(a,b,c)*	*Strain* $(e_1, e_2, e_3, e_4, e_5, e_6)$
(0,0,0)	(a,b,b)	(A,$\frac{\sqrt{3}}{2}$B,$-\frac{1}{2}$B,C,$\frac{\sqrt{2}}{2}$D,$\frac{\sqrt{2}}{2}$D)
(0,0,0)	(-a,-b,-b)	
(0,0,0)	(-a,b,b)	(A,$\frac{\sqrt{3}}{2}$B,$-\frac{1}{2}$B,C,$\frac{\sqrt{2}}{2}$D,$\frac{\sqrt{2}}{2}$D)
(0,0,0)	(a,-b,-b)	
(0,0,0)	(a,b,-b)	(A,$\frac{\sqrt{3}}{2}$B,$-\frac{1}{2}$B,C,$\frac{\sqrt{2}}{2}$D,$-\frac{\sqrt{2}}{2}$D)
(0,0,0)	(-a,-b,b)	
(0,0,0)	(a,-b,b)	(A,$\frac{\sqrt{3}}{2}$B,$-\frac{1}{2}$B,C,$\frac{\sqrt{2}}{2}$D,$-\frac{\sqrt{2}}{2}$D)
(0,0,0)	(a,b,-b)	
(0,0,0)	(b,a,b)	(A,$\frac{\sqrt{3}}{2}$B,$\frac{1}{2}$B,$\frac{\sqrt{2}}{2}$C,D,$\frac{\sqrt{2}}{2}$C)
(0,0,0)	(-b,-a,-b)	
(0,0,0)	(b,-a,b)	(A,$\frac{\sqrt{3}}{2}$B,$\frac{1}{2}$B,$\frac{\sqrt{2}}{2}$C,D,$\frac{\sqrt{2}}{2}$C)
(0,0,0)	(-b,a,-b)	
(0,0,0)	(b,a,-b)	(A,$\frac{\sqrt{3}}{2}$B,$\frac{1}{2}$B,$\frac{\sqrt{2}}{2}$C,D,$-\frac{\sqrt{2}}{2}$C)
(0,0,0)	(-b,-a,b)	
(0,0,0)	(-b,a,b)	(A,$\frac{\sqrt{3}}{2}$B,$\frac{1}{2}$B,$\frac{\sqrt{2}}{2}$C,D,$-\frac{\sqrt{2}}{2}$C)
(0,0,0)	(b,-a,-b)	
(0,0,0)	(b,b,a)	(A,0,B,$\frac{\sqrt{2}}{2}$C,$\frac{\sqrt{2}}{2}$C,D)
(0,0,0)	(-b,-b,-a)	
(0,0,0)	(b,b,-a)	(A,0,B,$\frac{\sqrt{2}}{2}$C,$\frac{\sqrt{2}}{2}$C,D)
(0,0,0)	(-b,-b,a)	
(0,0,0)	(b,-b,a)	(A,0,B,$\frac{\sqrt{2}}{2}$C,$-\frac{\sqrt{2}}{2}$C,D)
(0,0,0)	(-b,b,-a)	
(0,0,0)	(-b,b,a)	(A,0,B,$\frac{\sqrt{2}}{2}$C,$-\frac{\sqrt{2}}{2}$C,D)
(0,0,0)	(b,-b,-a)	

Table 4.11: 2 $P\bar{1}$

M_3^+ *(a,b,c)*	R_4^+ *(a,b,c)*	*Strain* $(e_1, e_2, e_3, e_4, e_5, e_6)$
(0,0,0)	(a,b,c)	(A,B,C,D,E,F)
(0,0,0)	(-a,-b,-c)	
(0,0,0)	(a,b,-c)	(A,B,C,D,E,F)
(0,0,0)	(-a,-b,c)	
(0,0,0)	(a,-b,c)	(A,B,C,D,E,F)
(0,0,0)	(-a,b,-c)	
(0,0,0)	(-a,b,c)	(A,B,C,D,E,F)
(0,0,0)	(a,-b,-c)	
(0,0,0)	(a,c,b)	(A,B,C,D,E,F)
(0,0,0)	(-a,-c,-b)	
(0,0,0)	(a,c,-b)	(A,B,C,D,E,F)
(0,0,0)	(-a,-c,b)	
(0,0,0)	(a,-c,b)	(A,B,C,D,E,F)
(0,0,0)	(-a,c,-b)	
(0,0,0)	(-a,c,b)	(A,B,C,D,E,F)
(0,0,0)	(a,-c,-b)	
(0,0,0)	(b,a,c)	(A,B,C,D,E,F)
(0,0,0)	(-b,-a,-c)	
(0,0,0)	(b,a,-c)	(A,B,C,D,E,F)
(0,0,0)	(-b,-a,c)	
(0,0,0)	(b,-a,c)	(A,B,C,D,E,F)
(0,0,0)	(-b,a,-c)	
(0,0,0)	(-b,a,c)	(A,B,C,D,E,F)
(0,0,0)	(b,-a,-c)	

Table 4.12: 2 P$\bar{1}$ cont.

M_3^+ *(a,b,c)*	R_4^+ *(a,b,c)*	*Strain* $(e_1, e_2, e_3, e_4, e_5, e_6)$
(0,0,0)	(b,c,a)	(A,B,C,D,E,F)
(0,0,0)	(-b,-c,-a)	
(0,0,0)	(b,c,-a)	(A,B,C,D,E,F)
(0,0,0)	(-b,-c,a)	
(0,0,0)	(b,-c,a)	(A,B,C,D,E,F)
(0,0,0)	(-b,c,-a)	
(0,0,0)	(-b,c,a)	(A,B,C,D,E,F)
(0,0,0)	(b,-c,-a)	
(0,0,0)	(c,b,a)	(A,B,C,D,E,F)
(0,0,0)	(-c,-b,-a)	
(0,0,0)	(c,b,-a)	(A,B,C,D,E,F)
(0,0,0)	(-c,-b,a)	
(0,0,0)	(c,-b,a)	(A,B,C,D,E,F)
(0,0,0)	(-c,b,-a)	
(0,0,0)	(-c,b,a)	(A,B,C,D,E,F)
(0,0,0)	(c,-b,-a)	
(0,0,0)	(c,a,b)	(A,B,C,D,E,F)
(0,0,0)	(-c,-a,-b)	
(0,0,0)	(c,a,-b)	(A,B,C,D,E,F)
(0,0,0)	(-c,-a,b)	
(0,0,0)	(c,-a,b)	(A,B,C,D,E,F)
(0,0,0)	(-c,a,-b)	
(0,0,0)	(-c,a,b)	(A,B,C,D,E,F)
(0,0,0)	(c,-a,-b)	

Table 4.13: 63 Cmcm

M_3^+ *(a,b,c)*	R_4^+ *(a,b,c)*	*Strain* $(e_1, e_2, e_3, e_4, e_5, e_6)$
(a,0,0)	(0,b,0)	(A,B,C,0,0,0)
(a,0,0)	(0,-b,0)	
(-a,0,0)	(0,b,0)	
(-a,0,0)	(0,-b,0)	
(a,0,0)	(0,0,b)	(A,B,C,0,0,0)
(a,0,0)	(0,0,-b)	
(-a,0,0)	(0,0,b)	
(-a,0,0)	(0,0,-b)	
(0,a,0)	(b,0,0)	(A,B,C,0,0,0)
(0,a,0)	(-b,0,0)	
(0,-a,0)	(b,0,0)	
(0,-a,0)	(-b,0,0)	
(0,a,0)	(0,0,b)	(A,B,C,0,0,0)
(0,a,0)	(0,0,-b)	
(0,-a,0)	(0,0,b)	
(0,-a,0)	(0,0,-b)	
(0,0,a)	(b,0,0)	(A,B,C,0,0,0)
(0,0,a)	(-b,0,0)	
(0,0,-a)	(b,0,0)	
(0,0,-a)	(-b,0,0)	
(0,0,a)	(0,b,0)	(A,B,C,0,0,0)
(0,0,a)	(0,-b,0)	
(0,0,-a)	(0,b,0)	
(0,0,-a)	(0,-b,0)	

Table 4.14: 62 Pnma

M_3^+ *(a,b,c)*	R_4^+ *(a,b,c)*	*Strain* $(e_1, e_2, e_3, e_4, e_5, e_6)$
(a,0,0)	(0,b,b)	(A,$\frac{\sqrt{3}}{2}$B,-$\frac{1}{2}$B,C,0,0)
(a,0,0)	(0,-b,-b)	
(-a,0,0)	(0,b,b)	
(-a,0,0)	(0,-b,-b)	
(a,0,0)	(0,b,-b)	(A,$\frac{\sqrt{3}}{2}$B,-$\frac{1}{2}$B,C,0,0)
(a,0,0)	(0,-b,b)	
(-a,0,0)	(0,b,-b)	
(-a,0,0)	(0,-b,b)	
(0,a,0)	(b,0,b)	(A,$\frac{\sqrt{3}}{2}$B,$\frac{1}{2}$B,0,C,0)
(0,a,0)	(-b,0,-b)	
(0,-a,0)	(b,0,b)	
(0,-a,0)	(-b,0,-b)	
(0,a,0)	(b,0,-b)	(A,$\frac{\sqrt{3}}{2}$B,$\frac{1}{2}$B,0,C,0)
(0,a,0)	(-b,0,b)	
(0,-a,0)	(b,0,-b)	
(0,-a,0)	(-b,0,b)	
(0,0,a)	(b,b,0)	(A,0,B,0,0,C)
(0,0,a)	(-b,-b,0)	
(0,0,-a)	(b,b,0)	
(0,0,-a)	(-b,-b,0)	
(0,0,a)	(b,-b,0)	(A,0,B,0,0,C)
(0,0,a)	(-b,b,0)	
(0,0,-a)	(b,-b,0)	
(0,0,-a)	(-b,b,0)	

Table 4.15: 11 $P2_1/m$

M_3^+ *(a,b,c)*	R_4^+ *(a,b,c)*	*Strain* $(e_1, e_2, e_3, e_4, e_5, e_6)$
(a,0,0)	(0,b,c)	(A,B,C,D,0,0)
(a,0,0)	(0,-b,-c)	
(-a,0,0)	(0,b,c)	
(-a,0,0)	(0,-b,-c)	
(a,0,0)	(0,b,-c)	(A,B,C,D,0,0)
(a,0,0)	(0,-b,c)	
(-a,0,0)	(0,b,-c)	
(-a,0,0)	(0,-b,c)	
(a,0,0)	(0,c,b)	(A,B,C,D,0,0)
(a,0,0)	(0,-c,-b)	
(-a,0,0)	(0,c,b)	
(-a,0,0)	(0,-c,-b)	
(a,0,0)	(0,c,-b)	(A,B,C,D,0,0)
(a,0,0)	(0,-c,b)	
(-a,0,0)	(0,c,-b)	

Table 4.16: 11 $P2_1/m$ cont.

M_3^+ *(a,b,c)*	R_4^+ *(a,b,c)*	*Strain* $(e_1, e_2, e_3, e_4, e_5, e_6)$
(0,a,0)	(b,0,c)	(A,B,C,0,D,0)
(0,a,0)	(-b,0,-c)	
(0,-a,0)	(b,0,c)	
(0,-a,0)	(-b,0,-c)	
(0,a,0)	(b,0,-c)	(A,B,C,0,D,0)
(0,a,0)	(-b,0,c)	
(0,-a,0)	(b,0,-c)	
(0,-a,0)	(-b,0,c)	
(0,a,0)	(c,0,b)	(A,B,C,0,D,0)
(0,a,0)	(-c,0,-b)	
(0,-a,0)	(c,0,b)	
(0,-a,0)	(-c,0,-b)	
(0,a,0)	(c,0,-b)	(A,B,C,0,D,0)
(0,a,0)	(-c,0,b)	
(0,-a,0)	(c,0,-b)	
(0,-a,0)	(-c,0,b)	
(0,0,a)	(0,b,c)	(A,B,C,0,0,D)
(0,0,a)	(0,-b,-c)	
(0,0,-a)	(0,b,c)	
(0,0,-a)	(0,-b,-c)	
(0,0,a)	(0,b,-c)	(A,B,C,0,0,D)
(0,0,a)	(0,-b,c)	
(0,0,-a)	(0,b,-c)	
(0,0,-a)	(0,-b,c)	
(0,0,a)	(0,c,b)	(A,B,C,0,0,D)
(0,0,a)	(0,-c,-b)	
(0,0,-a)	(0,c,b)	
(0,0,-a)	(0,-c,-b)	
(0,0,a)	(0,c,-b)	(A,B,C,0,0,D)
(0,0,a)	(0,-c,b)	
(0,0,-a)	(0,c,-b)	
(0,0,-a)	(0,-c,b)	

Table 4.17: $P4_2/nmc$

M_3^+ *(a,b,c)*	R_4^+ *(a,b,c)*	*Strain* $(e_1, e_2, e_3, e_4, e_5, e_6)$
(0,a,a)	(b,0,0)	(A,$\frac{\sqrt{3}}{2}$B,-$\frac{1}{2}$B,0,0,0)
(0,a,a)	(-b,0,0)	
(0,-a,-a)	(b,0,0)	
(0,a,-a)	(b,0,0)	
(0,-a,a)	(b,0,0)	
(0,a,-a)	(-b,0,0)	
(0,-a,a)	(-b,0,0)	
(0,-a,-a)	(-b,0,0)	
(a,0,a)	(0,b,0)	(A,$\frac{\sqrt{3}}{2}$B,$\frac{1}{2}$B,0,0,0)
(a,0,a)	(0,-b,0)	
(-a,0,-a)	(0,b,0)	
(a,0,-a)	(0,b,0)	
(-a,0,a)	(0,b,0)	
(a,0,-a)	(0,-b,0)	
(-a,0,a)	(0,-b,0)	
(-a,0,-a)	(0,-b,0)	
(0,-a,0)	(b,0,b)	
(a,a,0)	(0,0,b)	(A,0,B,0,0,0)
(a,a,0)	(0,0,-b)	
(-a,-a,0)	(0,0,b)	
(a,-a,0)	(0,0,b)	
(-a,a,0)	(0,0,b)	
(a,-a,0)	(0,0,-b)	
(-a,a,0)	(0,0,-b)	
(-a,-a,0)	(0,0,-b)	

Chapter 5

First principles thermodynamics study of phase stability in inorganic halide perovskite solid solutions

5.1 Introduction

Efficient, low-cost, solution-processed solar cells based on hybrid halide perovskite active layers offer a promising alternative to current Si-based technologies which require energy intensive manufacturing processes. [152] Tolerance to defects [4, 6, 153, 154, 155, 133] as a result of an "inverted" band structure [38] enables high photovoltaic performance from relatively low-temperature, solution-processed perovskite materials. Remarkably, hybrid perovskites seem to offer the best of both worlds in terms of optoelectronic properties: they have a high absorption coefficient [83] and high photoluminescence [156], characteristic of a pristine direct band gap semiconductor, but, at the same time, they exhibit long diffusion lengths [5, 10, 13] and low radiative recombination rates [8, 9, 11, 12], characteristic of indirect band gap semiconductors. The origin of these seemingly contra-

indicated properties is an extremely active area of research, but several explanations have been proposed. First, Rashba-Dresselhaus splitting of the conduction band (composed of Pb p states) due to spin-orbit coupling and local asymmetry of the inorganic sub lattice may explain the low recombination rates[16, 17, 18, 15, 20], since the region of phase space available for direct electron-hole recombination diminishes at moderate carrier concentrations. [19]. Second, electron-phonon interactions may lead to the formation of large polarons which protect carriers from scattering and recombination. [21, 22, 12].

Regardless of the mechanism for low recombination rates, the commercial adoption of hybrid perovskites requires materials that remain thermodynamically stable to thermal variations resulting from the natural day-night cycle and, of course, to light irradiation. Even at ambient conditions, hybrid lead iodide perovskites decompose to PbI_2 within hours or days. [153, 157] Moreover, inorganic perovskite compounds $CsSnI_3$ and $CsPbI_3$ have been observed to revert to a stable non-perovskite δ-phase. [136, 8, 132, 49] The main approach for stabilizing the photoactive perovskite α-phase involves increasing the average effective size of the A-cation constituent through substitution with mixtures of Cs, methylammonium, and formamadinium. [23, 24, 25, 26, 27]

Another key feature of halide perovskites is the ability to tune the band gap through halide substitution. Compositional engineering on the halide sub lattice allows band gap tuning across the entire composition range from small band gap AMI_3 to larger band gap $AMBr_3$ materials. [28, 29, 30, 31] However, in the $x < 0.66$ region of $APb(I_xBr_{1-x})_3$ alloys, the so-called Hoke effect leads to semi-reversible photo-induced phase separation into I-rich and Br-rich domains. [158, 159, 160] In $CH_3NH_3Pb(I_xBr_{1-x})_3$, photo-induced phase separation prevents tuning of the band gap into the 1.75-2.25 eV range thereby diminishing the maximum attainable open circuit voltage in photovoltaic devices. [161]

The most striking experimental signature of the Hoke effect involves a drastic red shift in the photoluminescence spectrum due to the formation of small band gap, brightly lu-

minescing I-rich domains. In particular, when a film of mixed halide content such as $APb(Br_{0.5}I_{0.5})_3$ is subjected to light irradiation, an original PL peak at around 650 nm diminishes while a large peak at 725 nm increases in intensity due to small band gap I-rich domains. A small peak at 530 nm also grows due to large band gap Br-rich domains. Thin film X-ray diffraction also points to the formation of two crystalline domains with differing lattice parameters, namely the Br- and I-rich domains. [158] Transient differential absorption measurements further support the notion of light induced phase segregation and establish kinetic rate constants for the process. [162]. Lastly, direct cathodoluminescence imaging also reveals the formation of I-rich domains due to light irradiation. [163]

In order to better understand the Hoke effect, it is crucial that the equilibrium phase diagrams of the alloyed halide perovskites are accurately characterized and fully understood. In this letter, we use cluster expansions and finite temperature statistical mechanics to predict the equilibrium phase behavior of inorganic binary halide perovskites, $CsM(X_xY_{1-x})_3$. While first-principles approaches have been used before to study binary halide perovskite phase stability [163, 164, 165], they have relied on mean field approaches and therefore neglect the important role of long- and short-range order among the different halide species at finite temperature. We find that Pb-based compounds tend to have a ground state halide ordering at $x = 2/3$, which our finite temperature statistical mechanics treatment rigorously accounts for. In addition, we show that the stability of the $x = 2/3$ ordering in for example $CsPb(I_xBr_{1-x})_3$ results in a miscibility gap that only extends to $x = 2/3$, a composition that closely matches the end state of the photo-induced phase separation in this alloy. Our Monte Carlo simulations also show that the Pb-based compounds retain a degree of long range order associated with halide layering at temperatures above the miscibility gap around $x = 2/3$. Finally, a correlation is found between the critical temperature for mixing and the volume difference between the end members of the alloys, suggesting a simple design rule to control miscibility in alloyed

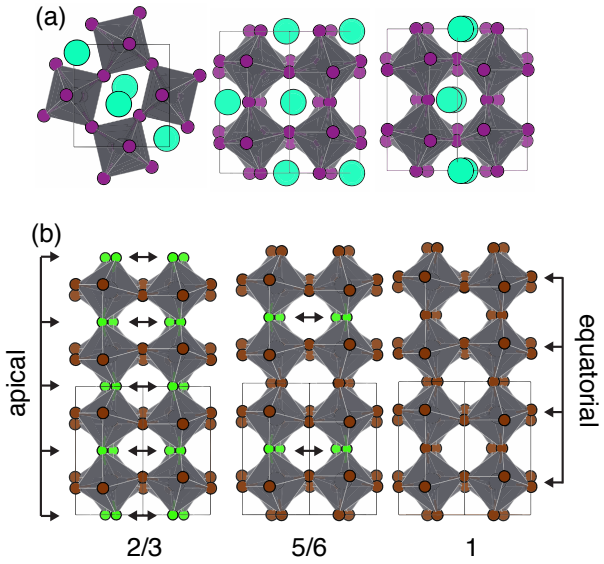

Figure 5.1: (a) Ground state orthorhombic Pnma γ-phase structure for $CsPbI_3$. (b) An example of the layered ground state at $x = 2/3$ is shown for $CsPbBr_2Cl$. The $x = 5/6$ structure is a related layered structure within 1meV of convex hull. Double sided arrows indicate layers of Cl on the halide sub lattice. $x = 1$ is the $CsPbBr_3$ ground state for comparison. The two distinct halide sub lattices are labeled apical and equatorial.

halide perovskites.

5.2 Methods

The Vienna ab initio Simulation Package (VASP) [104, 105] was used to carry out DFT calculations with a plane-wave basis set and projector augmented wave [104, 106] (PAW) pseudopotentials. The Perdew-Burke-Ernzerhof functionals revised for solids (PBEsol) were used to approximate the electron exchange-correlation functional. [166] For the orthorhombic primitive cell a 6×4×4 k-point mesh centered at the Γ point was used with a 600 eV plane wave energy cutoff. Energies were converged to within 1 meV/atom with respect to k-point density. Geometric optimization of symmetrically distinct halide decorations was halted when energies between ionic steps fell below 0.005 meV/atom and final energies were calculated during a subsequent static calculation. The CASM

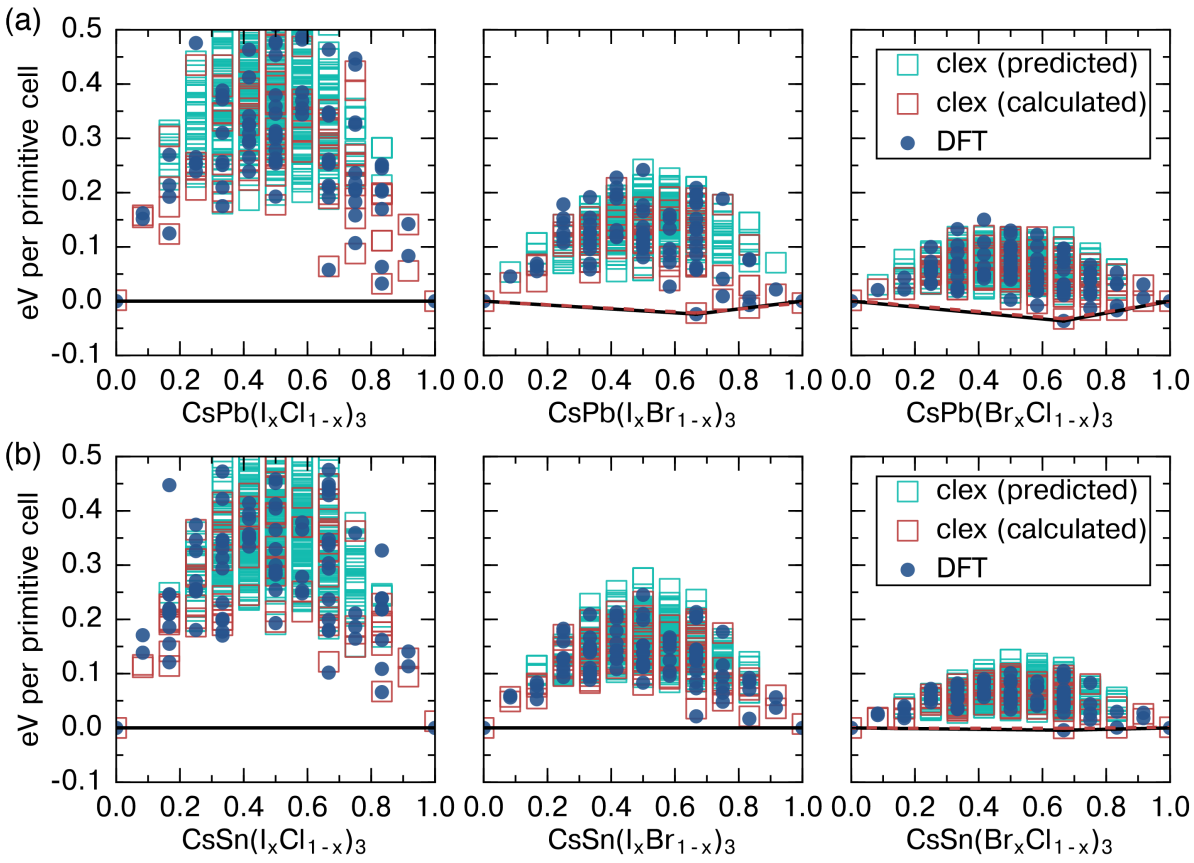

Figure 5.2: DFT formation energies (blue circles) for three (a) Pb-based and (b) Sn-based halide binaries compared to the cluster expansion energies (red squares). Energies for configurations which were not calculated with DFT are all predicted to lie above the convex hull (teal squares).

code, [167, 168, 64] was used to construct cluster expansions and perform Monte Carlo simulations. We fit a cluster expansion effective Hamiltonian to DFT energies using a genetic algorithm for feature (cluster) selection [66] and least squares minimization to calculate the ECI. In order to avoid over-fitting, ECI which minimize a 10-fold cross validation (CV) score were used as the model parameters. In this way we were able to construct effective Hamiltonians with CV scores and root mean square errors (RMSE) less than 10 meV/atom, approaching the limit set by DFT accuracy which is around 1 meV/atom. Crystal structures were visualized using the VESTA program suite. [109]

5.3 Results

Full geometric optimization with DFT predicted the Pnma orthorhombic form of perovskite with $b^-b^-a^+$ tilts as having the lowest energy of all 15 unique perovskite tilt systems for Cs-based inorganic halide perovskites. [169] Hence, to predict miscibility temperatures for halide perovskite binaries we chose the Pnma structure, which is pictured in Figure 5.1, as the parent crystal structure over which to explore binary halide disorder at absolute zero and at finite temperature.

Halide substitution in halide perovskites was modeled with the cluster expansion approach [54]. We studied six binary systems: $CsSn(I_xBr_{1-x})_3$, $CsPb(I_xBr_{1-x})_3$, $CsSn(Br_xCl_{1-x})_3$, $CsPb(Br_xCl_{1-x})_3$, $CsSn(I_xCl_{1-x})_3$, and $CsPb(I_xCl_{1-x})_3$. The orthorhombic primitive cell of the Pnma tilt system has 20 atoms, 12 of which are halide sites. DFT energies were collected after full geometric optimization of about 70-80 configurations with symmetrically distinct halide decorations for each binary. The DFT energies were used to train a cluster expansion of the form:

$$E(\vec{\sigma}) = V_0 + \sum_{\alpha} V_\alpha \varphi_\alpha(\vec{\sigma}) \tag{5.1}$$

where $\vec{\sigma}$ specifies the decoration of halide species on the alloying sites, α denotes clusters of sites, the $\varphi_\alpha(\sigma)$ are polynomial basis functions composed of products of configurational variables, and the V_α are expansion coefficients known as effective cluster interactions (ECI) to be determined by fitting to the DFT training data. Details of the fitting procedure for finding appropriate ECI are given in the Methods.

DFT energies are compared to the cluster expansion energies (clex) in Figure 5.2 for Sn and Pb binaries, respectively. Noticeably, ground state orderings are found at $x = 2/3$ for $CsSnBr_2Cl$, $CsPbBrI_2$, and $CsPbBr_2Cl$, agreeing with other theoretical and experimental

reports. [164, 165, 30, 158, 170] In fact, as has been previously pointed out the layered structures at $x = 2/3$ maximize favorable Coulomb interactions which explains their low formation energy. [165] Furthermore, Figure 5.2 demonstrates the effect of halide size difference on the mixing energy. For instance, neither of the $CsM(I_xCl_{1-x})_3$ binaries (with M = Pb or Sn) exhibit ground state orderings at intermediate concentrations x, and the postive formation energies of these mixed halide configurations are the highest among binary systems studied here. The absolute values of the formation energies of mixing decrease as the size difference between the anions decrease when going from $CsM(I_xCl_{1-x})_3$ to $CsM(I_xBr_{1-x})_3$ to $CsM(Br_xCl_{1-x})_3$.

Semi-grand canonical Monte Carlo simulations were performed using the CASM code to calculate thermodynamic averages as a function of temperature and halide chemical potential. [167, 168, 64] Free energy integration was used to construct finite temperature phase diagrams as presented in Figure 5.3. Miscibility gaps were found for both $CsPb(I_xCl_{1-x})_3$ and $CsSn(I_xCl_{1-x})_3$ with transition temperatures of 423 K and 460 K, respectively. The high transition temperatures are consistent with the fact that $CsM(I_xCl_{1-x})_3$ solutions are experimentally unaccessible at room temperatures. [171] The $CsPb(I_xBr_{1-x})_3$ and $CsSn(I_xBr_{1-x})_3$ binaries exhibit transition temperatures at 217 K and 225 K in agreement with previous theoretical studies. [165] Finally, $CsPb(Br_xCl_{1-x})_3$ and $CsSn(Br_xCl_{1-x})_3$ binaries have transition temperatures at 97 K and 74 K, respectively, indicating facile phase miscibility. A second small miscibility gap was found at very low temperatures below 50 K in the binary systems that exhibit the $x = 2/3$ ground state ordering. However, due to the limitations of Monte Carlo sampling we were unable to resolve these features, and we cut off the phase diagram at 50 K.

The strong preference for layering in $CsPb(Br_xCl_{1-x})_3$, $CsSn(Br_xCl_{1-x})$, and $CsPb(I_xBr_{1-x})_3$ results in the $x = 2/3$ ground state and a sharp phase boundary near that composition. The layered ordering at $x = 2/3$, however, does not undergo an abrupt thermodynamic

order-disorder phase transition with increasing temperature, but instead very gradually approaches the disordered state over a broad temperature interval. This is possible because the layered ordering at $x = 2/3$ does not break any symmetries of the orthorhombic parent Pmna crystal structure. The different halides of the binary alloys segregate to sites that are already symmetrically distinct sites due to the octahedral tilting within the Pmna orthorhombic phase. There is therefore no requirement for a thermodynamic order-disorder transition.

To gauge the degree of halide layering we introduce the order parameter:

$$\eta = x_{\mathrm{eq}} - x_{\mathrm{ap}}$$

where x_{eq} and x_{ap} denote the compositions on the equatorial and apical octahedral sites shown in Figure 5.1. The order parameter η takes on its maximum value of 1 in the fully ordered state at $x = 2/3$, where the larger halide ion occupies the equatorial sites, and becomes equal to zero in the completely disordered state, when the compositions on each sub lattice are equal to each other. In Figure 5.3, constant chemical potential Monte Carlo cooling runs are plotted with the color indicating the average value of η. Yellow indicates an ideally disordered solution, while purple signifies halide layering. As is evident from Figure 5.3, all of the binaries, except $CsSn(I_xCl_{1-x})_3$, retain a degree of halide layering even above the critical temperature for mixing. Interestingly, layering is more pronounced for the Pb-based compounds, with $CsPb(I_xBr_{1-x})_3$ showing long range order even at 300 K.

Although the six binaries studied here show differences with respect to the shape of the two-phase region and the degree of layering, the critical temperatures for full mixing seem to be agnostic to the identity of the metal ion and generally increase as the size difference between halide alloying elements increases. Figure 5.4, which shows the mixing

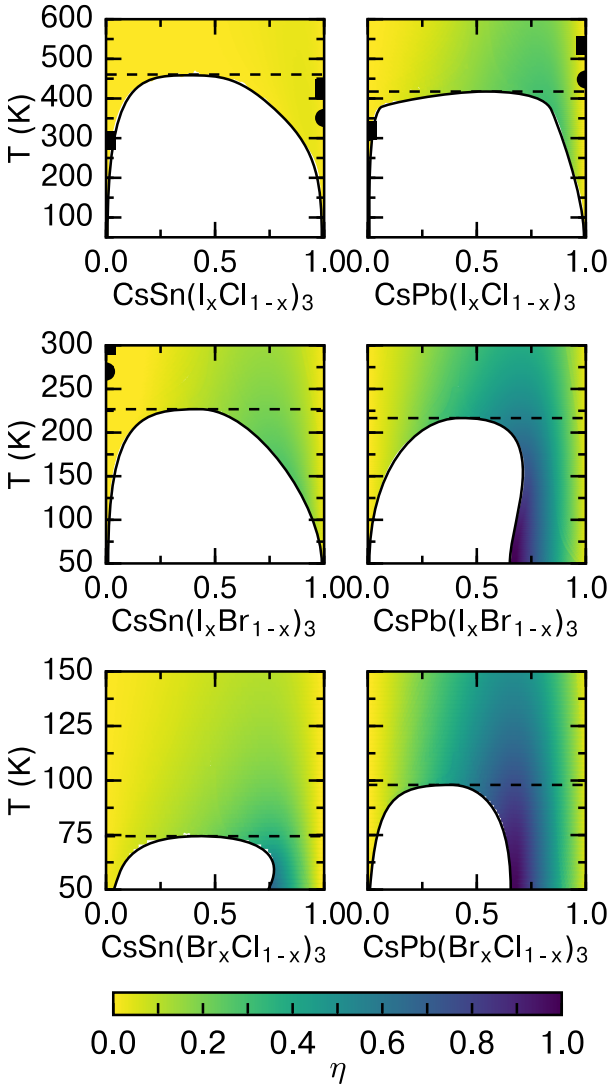

Figure 5.3: Phase diagrams for the three Pb- and Sn-based binaries as determined through free energy integration from semi-grand canonical Monte Carlo sampling within a μT ensemble. Dashed lines indicate the estimated critical temperature. Solid black lines trace the boundary between the two-phase region (white) and the solid solution phase where the color corresponds to the layering order parameter, η, as described in the text. Only $CsM(I_xCl_{1-x})_3$ binaries are predicted to phase separate at room temperature. For systems which exhibit the $x = 2/3$ ground state, a sharp phase boundary around $x = 2/3$ is predicted. Black squares (circles) represent experimentally observed tetragonal to cubic (orthorhombic to tetragonal) structural phase transition temperatures.

temperature T_{mg} as a function of the volume difference between binary end members, reveals the key role played by halide ion size. As is clearly evident in Figure 5.4, a

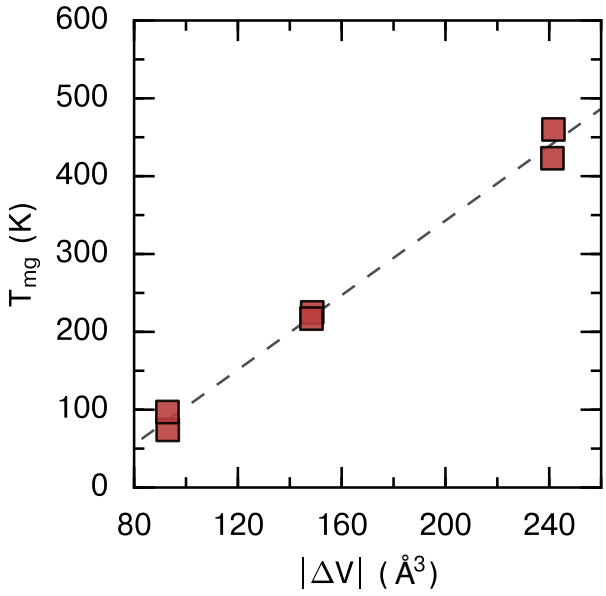

Figure 5.4: Transition temperatures for full halide miscibility (as determined from Figure 5.3) plotted as a function of volume difference between the DFT-relaxed end members for each binary. A strong linear relationship suggests the significant role of strain in determining the phase miscibility.

large volume difference between end-members results in a higher critical temperature. Differently sized halide anions introduce local strains that penalize a solid solution and favor phase separation. This result can serve as a design principle for compositional engineering in other binary halide perovskites with different A-site cations: to decrease the mixing temperature choose end members that have similar volumes.

5.4 Discussion

Our first-principles statistical mechanics study of phase stability in alloyed orthorhombic Pnma $CsM(X_xY_{1-x})_3$ perovskites has demonstrated the importance of long- and short-range order both at absolute zero Kelvin and at finite temperature. Three of the six $CsM(X_xY_{1-x})_3$ binaries studied here favor an ordered phase at $x = 2/3$ in which the larger halide occupies the equitorial sites and the smaller halide occupies the apical

sites of the orthorhombic γ-phase perovskite parent crystal structure. The layered halide ordering within the orthorhombic perovskite persists to room temperature and above, even in the binaries that do not form the perfectly ordered phase at zero Kelvin. Our calculations also show that the binaries that form the layered $x = 2/3$ phase do not have simple miscibility gaps that span the full composition range between $x = 0$ and $x = 1$. Instead, their phase diagrams have two phase regions between $x \approx 0$ and $x \approx 2/3$. The calculated phase diagrams of six halide perovskite alloys have also revealed a clear correlation between the critical temperature of mixing and the volume difference between the alloy end members.

The calculations of this work extend past studies of phase stability in the binary halide perovskites.[164, 165] Previous first-principles treatments, however, did not explicitly treat the long-range ordered $x = 2/3$ phases or the presence of short-range order at finite temperature as they were based on mean field approximations. Furthermore, past studies considered halide disorder over tilt systems of the perovskite crystal that have been shown to be dynamically unstable: Brivio et al. [164] used a pseudo cubic reference phase for the hybrid perovskite, while the orthorhombic Pnma structure is known to be the ground state, and Yin et al. [165] used the I4/mcm reference state for the *inorganic* halide perovskites even though it is only observed in *hybrid* perovskites.

The results presented here, including the calculated phase diagrams and order-parameter maps, represent an accurate thermodynamic description of the alloyed orthorhombic halide perovskites with which a more precise understanding of photo-induced phase separation, also known as the Hoke effect, [158, 30, 160] can be realized. Several models have been put forward to explain the Hoke effect in hybrid perovskites such as $CH_3NH_3Pb(I_xBr_{1-x})_3$. Bischak et al. [163] developed a mean-field thermodynamic description that predicts photo-induced phase segregation as a result of polaron formation due to the preference of holes for small bandgap I-rich domains. In this model, light

irradiation leads to polaron formation which induces local strains that drive halide segregation. Figure 5.4 does indeed show that an increase in the difference in the volumes of the pure halide perovskite end members leads to an increase in the critical temperature of the miscibility gap. Presumably this correlation is preserved even if the increase in the difference in volume between end members is photo-induced. Kinetic models have also been developed that assume that band gap differences between the solid solution phase and the I-rich phase generates driving forces for phase segregation. [172]

A complexity that emerges in studying the Hoke effect in a hybrid perovskite such as $CH_3NH_3Pb(I_xBr_{1-x})_3$ is the occurrence of structural transformations around room temperature. For instance, $CH_3NH_3PbI_3$ exists in the tetragonal I4/mcm phase at room temperature and undergoes a tetragonal to cubic transition at 330 K. [131] For $CH_3NH_3PbBr_3$, this cubic to tetragonal transition occurs below room temperature at 235 K. [173, 174, 92] The difference in transition temperatures for the pure end members indicates that there should be a two-phase region separating an I-rich tetragonal phase from a Br-rich cubic phase around room temperature. The existence of such a two-phase region obfuscates the role of photo-induced excited state phenomena versus equilibrium thermodynamics as the origin of halide segregation in the Hoke effect.

In contrast to the hybrid perovskites, the $CsPb(I_xBr_{1-x})_3$ alloy, which also exhibits photo-induced phase separation, [160, 175, 172] does not undergo structural transformations until well above room temperature. The orthorhombic-tetragonal phase transition occurs at around 448 K [8] (361 K) [45] in $CsPbI_3$ ($CsPbBr_3$), while the tetragonal-cubic transition occurs at 533 K [8] (403 K) [45] in $CsPbI_3$ ($CsPbBr_3$). The dependence of the structural phase transition temperatures on composition x is not yet established for $CsPb(I_xBr_{1-x})_3$. Nevertheless, our first-principles statistical mechanics study predicts that $CsPb(I_xBr_{1-x})_3$ forms a complete solid solution within the orthorhombic phase around 200 K. The higher temperature tetragonal and cubic forms of $CsPb(I_xBr_{1-x})_3$

therefore likely also form solid solutions for all x. To first-order then, we expect simple lens shaped two-phase regions separating tetragonal from orthorhombic and cubic from tetragonal $CsPb(I_xBr_{1-x})_3$ as schematically illustrated by the dashed lines in Figure 5.5. The calculated miscibility gap within the orthorhombic form of $CsPb(I_xBr_{1-x})_3$ is also shown in Figure 5.5 with a solid line.

Beal et al. [160] showed that the Hoke effect takes place in $CsPb(I_xBr_{1-x})_3$ for compositions $x < 0.66$. Under light illumination, the photoluminescence peak of samples with compositions $x < 0.66$ converge to the $x = 2/3$ PL peak at around 650 nm, which remains constant as a function of time. [160] Hence, the experimental observations suggest the presence of a phase boundary at $x = 2/3$ under light irradiation. Our first-principles study predicts that $CsPb(I_xBr_{1-x})_3$ forms a solid solution well below room temperature, which is consistent with the fully tunable band gap for this binary at room temperature across the whole composition range. [176, 160] Remarkably, the topology of the predicted low-temperature miscibility gap in orthorhombic $CsPb(I_xBr_{1-x})_3$ (Figure 5.5) is very similar to the photo-induced miscibility gap observed by Beal et al. [160] at room temperature.

Our calculated low-temperature phase diagram for $CsPb(I_xBr_{1-x})_3$ suggests that the layered halide ordering at $x = 2/3$ plays an important role in the photo-induced phase separation in this alloy. The topology and quantitative transition temperatures of the halide perovskite phase diagrams are sensitive to the distribution of the formation energies for different halide orderings. This is evident upon comparing the first-principles DFT formation energy plots of Figure 5.2 with the calculated phase diagrams of Figure 5.3. Light illumination that causes electronic excitations will affect the formation energy of each halide ordering in a different way, since each symmetrically distinct ordering will have a different band structure. If for example, light illumination affects the formation energy of the layered $x = 2/3$ ordering in a more favorable way than the energies of all the

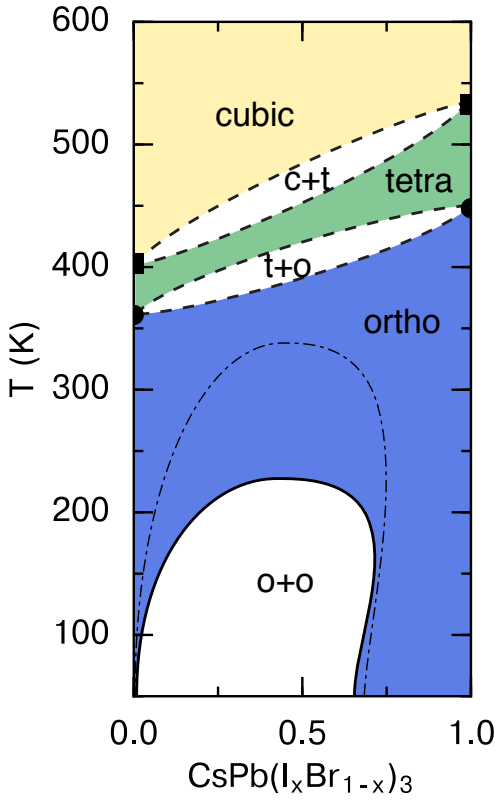

Figure 5.5: Hypothetical extension of the CsPb(I_xBr_{1-x})$_3$ phase diagram to include known structural phase transitions from the stable orthorhombic phase to the dynamically stabilized tetragonal and cubic phases. Black squares (circles) represent experimentally observed tetragonal to cubic (orthorhombic to tetragonal) structural phase transition temperatures. Dashed lines represent two-phase boundaries for ideal mixing and the solid line is adapted from Figure 5.3. Dotted-dashed line represents possible two-phase boundary during light irradiation.

other arrangements, it will result in an increase in the finite temperature thermodynamic stability of the $x = 2/3$ ordering and a concomitant increase in the miscibility gap critical temperature, thereby extending the 2/3 phase boundary to higher temperatures as shown by the dashed-dotted line in Figure 5.5. The photo-luminescence experiments of Beal et al. [160], consistently showing photo-induced phase segregation that results in an I-rich phase around $x = 2/3$, suggests that this may be occurring. It is therefore suggested that future experimental and theoretical studies focus on the $x = 2/3$ layered ordering to further clarify the Hoke effect in CsPb(I_xBr_{1-x})$_3$.

In order to properly account for structural phase transitions of the end members, it is necessary to incorporate the vibrational contributions to the free energy together with the configurational free energy. However, for materials such as perovskites that are dynamically stabilized at high temperatures, harmonic approximations are not adequate, and higher order formulations of the vibrational hamiltonian are required. [169] In principle, the full phase diagram could be calculated by combining an anharmonic vibrational cluster expansion [64] with a configurational cluster expansion.

In conclusion, we have applied a rigorous statistical mechanics approach to calculate the finite temperature phase diagrams for Pb and Sn halide perovskite binaries within the low-temperature orthorhombic γ-phase. The prevailing distinction between binaries studied in this work is the size difference between halide ions, which introduces asymmetry into the phase diagrams and affects the critical temperature for mixing. In particular, we propose a simple design principle to guide alloy engineering: a smaller volume difference between end members results in a lower critical mixing temperature. We presented the first phase diagrams that fully account for the 2/3 ground state and showed that Pb-based compounds still exhibit a tendency to layer ordering at high temperatures. Finally we discussed the implications of the $CsPb(I_xBr_{1-x})_3$ phase diagram and the stability of the $x = 2/3$ layered ordering on the Hoke effect.

Chapter 6

Machine-learning the potential energy landscape of halide perovskites

6.1 Introduction

Structural phase transitions from stable ground states to dynmically unstable high temperature phases are abundant in technoglogically useful materials yet prediction of their vibrational properties from first-principles calculations remains a challenge. In principle, large ab initio molecular dynamics simulations could provide all finite temperature thermodynamic information. However, due to the computational cost of density functional theory calculations it becomes necessary to approximate the DFT with simpler, computationally efficient, effective Hamiltonians. For ground state phases at equilibrium, vibrational models based on harmonic or quasi-harmonic approximations can accurately reproduce finite-temperature vibrational properties; however, for phases that exist at saddle points or local maxima within the potential energy surface (PES), higher order expansions of the PES are necessary.

Several methods exist which seek to parameterize the zero Kelvin PES of materials

from density functional theory including effective Hamiltonians based on local displacive modes [177], localized lattice Wannier modes [118], the slave-mode expansion, [178], and the anharmonic vibrational cluster expansion [64]. Additionally, there exist many machine learning based methods which utilize a set of symmetry invariant basis functions to describe local atomic environments along with a particular model architecture such as artificial neural networks to fit the high-dimensional PES. [71, 72, 73, 74, 75, 179, 180, 181, 182, 183, 184, 185, 186, 187, 188, 189, 190, 191] In this work, we focus on the anharmonic vibrational cluster expansion method and show how the incorporation of a neural net model archiecture provides an avenue for accurately mapping the DFT PES.

Given the impressive success of halide perovskite materials over the past decade in achieveing high power conversion efficiencies as the active material in phtovoltaic devices, [2] we focus on the inorganic halide perovskite $CsPbBr_3$ as our model system. Since most Cs-based inorganic halide perovskite undergo a similar phase transition sequence upon cooling (cubic, $Pm\bar{3}m \rightarrow$ tetragonal, $P4/mbm \rightarrow$ orthorhombic, Pnma), [43, 44, 45, 42, 46, 47, 48, 49, 50] $CsPbBr_3$ can be considered as representative of the family of Cs-based inorganic halide perovskites.

The structural phase transitions in inoragnic halide perovskites involve collective displacement modes associated with octahedral tilting [169], and it has been shown that at high temperatures these modes are still highly populated giving rise to strong local distortion even in the average cubic structure. [18, 124, 125, 126, 127] Moreover, the soft and strongly anharmonic lattice dynamics are thought to play a role in the electronic properties due to large local fluctuations resulting in Rashba-Dresselhaus splitting of the conduction bands [15, 16, 17, 18, 15, 19, 20] and giving rise to strong electron-phonon interactions which allow large polaron formation. [21, 22, 12]

Since the different phases of inorganic halide perovskites can be connected by symmetry lowering displacive modes from the high temperature cubic phase, it is convenient to

parameterize the energy alndscape in terms of distortions of the cubic reference. For this reason we base our method upon the anharmonic vibrational cluster expansion which expands the energy in terms of basis functions of disortions of local cluster as referenced to the cubic phase. Instead of a linear expansion in terms of these basis functions, we use artificial neural nets which are a non-linear extension of the linear cluster expansion model. Two different approaches using the neural-net architecture are explored in which the energy is a sum of either site energies or cluster energies. Finally, after fitting these two different models and performing cross-validation, we find that site-based models best fit the PES. While low training and test set errors are achieved, we also emphasize that neural net architectures are likely not suitable for thermodynamic simulations such as finite temperature Monte Carlo or molecular dynamics studies due to poor model extrapolation.

6.2 Methods

6.2.1 Descriptors

In order to take full advantage of crystal symmetry we work in a symmetry adapted basis of pair distances that corresponds to cluster normal modes. In particular, we represent the energy in terms of polynomials of collective cluster displacements (CCDs) of the high symmetry cubic phase. The CCDs transform as irreducible representations of the clusters point group in the high symmetry phase. Thus, they can capture any symmetry lowering distortions with a minimal number of descriptors. The CCD amplitudes are formed from a linear combination of functions of squared pair distances, d_l,

$$q_k = \sum_l Q_{kl} f(d_l)$$

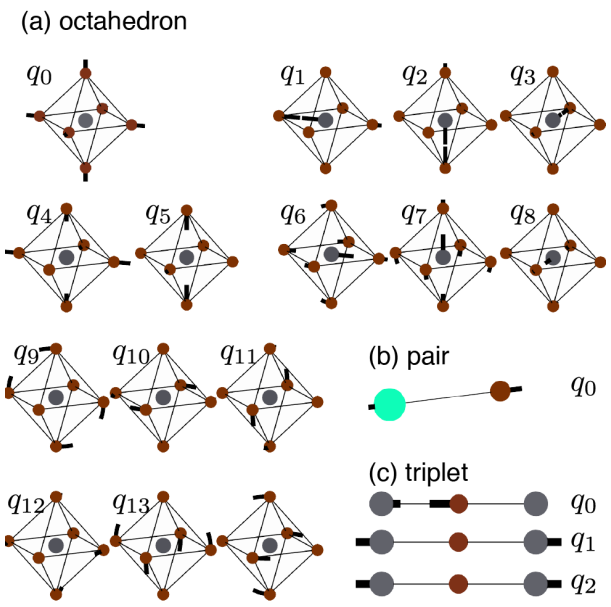

Figure 6.1: Depictions of the displacement modes specified by CCDs for an (a) octahedron, (b) pair, and (c) triplet.

where f can take on different nonlinear forms such as the natural log or quadratic functor. Crystal basis functions which obey symmetries of the crystal point group are then constructed as polynomials of the CCD amplitudes and they are denoted $\Phi_\alpha^{(n)}(\vec{q})$ for the n^{th} basis function of cluster α.

The basis functions for the different clusters are enumerated below up to second order. Higher order basis functions can be found in the appendix.

Table 6.1: General Pair Basis Functions up second order

basis function	formula
Φ_1	q_0
Φ_2	q_0^2

Table 6.2: General linear triplet basis functions up to second order

basis function	formula
Φ_0	q_1
Φ_1	q_2
Φ_2	q_0^2
Φ_3	q_1^2
Φ_4	$\sqrt{2}q_1q_2$
Φ_5	q_2^2

Table 6.3: General octahedron basis functions up to second order

basis function	formula
Φ_0	q_0
Φ_1	q_0^2
Φ_2	$\sqrt{1/3}(q_1^2+q_2^2+q_3^2)$
Φ_3	$\sqrt{1/2}(q_4^2+q_5^2)$
Φ_4	$\sqrt{2/3}(q_1q_6+q_2q_7+q_3q_8)$
Φ_5	$\sqrt{1/3}(q_6^2+q_7^2+q_8^2)$
Φ_6	$\sqrt{1/3}(q_9^2+q_{10}^2+q_{11}^2)$
Φ_7	$\sqrt{1/3}(q_{12}^2+q_{13}^2+q_{14}^2)$

6.2.2 Linear Cluster Expansion

Here we review the mathematical framework for the CCD hamiltonian, a linear combination of crystal basis functions, and generalize to a neural network model based on non-linear combinations of crystal basis functions.

We assume that the energy of a crystal can be expanded as a sum of n-body terms that depend only on pair distances.

$$V(\vec{r}) = V_0 + \sum_{\alpha}\sum_{n} V_{\alpha}^{(n)}\Phi_{\alpha}^{(n)}(\vec{q})$$

Here α runs through all clusters of the crystal, and n indexes the crystal basis functions of that cluster. We can instead rewrite the energy as a sum of distinct clusters α' and then average over all symmetrically equivalent clusters β which are part of the

cluster's orbit, $\Omega_{\alpha'}$ to arrive at the following

$$V(\vec{r}) = V_0 + \sum_{\alpha'} \sum_{n} V_{\alpha'}^{(n)} \sum_{\beta \in \Omega_{\alpha'}} \Phi_{\alpha'}^{(n)}(\vec{q}_\beta) \tag{6.1}$$

$$= V_0 + \sum_{\alpha'} \sum_{n} V_{\alpha'}^{(n)} |\Omega_{\alpha'}| \langle \Phi_{\alpha'}^{(n)}(\vec{q}_\beta) \rangle \tag{6.2}$$

where $\langle \Phi_{\alpha'}^{(n)}(\vec{q}_\beta) \rangle = \frac{1}{|\Omega_{\alpha'}|} \sum_{\beta \in \Omega_{\alpha'}} \Phi_{\alpha'}^{(n)}(\vec{q}_\beta)$, and $|\Omega_{\alpha'}|$ is the size of the orbit $\Omega_{\alpha'}$ or, in other words, the number of symmetrically equivalent copies cluster α'. Normalizing for the number of unit cells, m, such that $v = V/m$:

$$v = v_0 + \sum_{\eta=(\alpha',n)} V_{\alpha'}^{(n)} \frac{|\Omega_{\alpha'}|}{m} \langle \Phi_{\Omega_\eta}(\vec{q}_\beta) \rangle \tag{6.3}$$

$$= v_0 + \sum_{\eta=(\alpha',n)} V_{\alpha'}^{(n)} m_{\alpha'} \langle \Phi_{\Omega_\eta}(\vec{q}_\beta) \rangle \tag{6.4}$$

This is the classical expression for the cluster expansion that allows fitting of the effective cluster interactions (ECI), $V_{\alpha'}^{(n)}$, to first principles calculations (which provide the energies v, and correlations $\langle \Phi_{\Omega_\eta}(\vec{q}_\beta) \rangle$) through linear regression techniques. Note that the ECI represent an individual cluster's contribution to the total energy; therefore it is multiplied by the orbit multiplicity in the final expression.

6.2.3 Cluster-Based Neural Net

Instead of a linear combination of orbit-averaged basis functions, we can rearrange the sums from above and consider a non-linear combination of polynomial basis functions for each cluster:

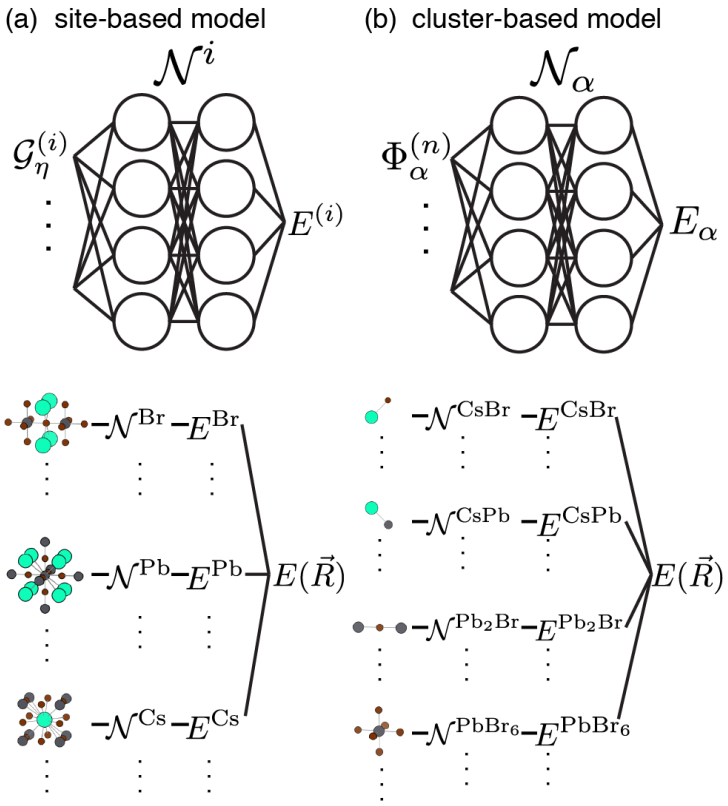

Figure 6.2: Visualization of how (a) site-based and (b) cluster-based models incorporate site-averaged basis functions or cluster-based basis functions respectively.

$$V(\vec{r}) = V_0 + \sum_{\alpha'} \sum_{\beta \in \Omega_{\alpha'}} \sum_{n} V_{\alpha'}^{(n)} \Phi_{\alpha'}^{(n)}(\vec{q}_\beta) \tag{6.5}$$

$$V \approx V_0 + \sum_{\alpha'} \sum_{\beta \in \Omega_{\alpha'}} \mathcal{N}_{\Omega_{\alpha'}} \left(\left\{ \Phi_{\alpha'}^{(n)}(\vec{q}_\beta) \right\} \right) \tag{6.6}$$

where β runs over all symmetrically equivalent copies of cluster α', and $\mathcal{N}_{\Omega_{\alpha'}} \left(\left\{ \Phi_{\alpha'}^{(n)}(\vec{q}_\beta) \right\} \right)$ represents a neural network model for cluster α' with polynomial basis function (n) as inputs and the individual cluster contribution to the crystal energy as an output. Thus the final model V is simply the sum of $|\alpha'|$ neural networks $\mathcal{N}_{\Omega_{\alpha'}}$, where $|\alpha'|$ is the number of unique clusters. A visual interpretation of the computational graph for a cluster-based

neural net model is depected in Figure 6.2(b). In this model, each distinct cluster type is associated with a distinct neural net. Then the neural net produces a per cluster energy for each cluster of that type found throughout the crystal. All cluster energy contributions are then summed throughout the crystal resulting in the total energy.

6.2.4 Site-Based Neural Net

Alternatively, we can express the energy as a sum of site contributions to the energy where we sum over all clusters that contain the current site:

$$V(\vec{r}) = V_0 + \sum_i \sum_{\Omega_\eta^i} V_{\Omega_\eta^i} \frac{1}{N_{\alpha'}} \sum_{\beta \in \Omega_\eta^i} \Phi_{\Omega_\eta^i}(\vec{q}_\beta) \tag{6.7}$$

$$= V_0 + \sum_i E^i(\{\vec{q}\}) \tag{6.8}$$

where $N_{\alpha'}$ denotes the number of sites in the cluster α'. This term is necessary to avoid over counting a cluster's contribution to the total energy. For example, a pair cluster will appear twice in this expression since it is visited once for each site; therefore we divide energy contribution by the number of sites. Ω_η^i, where $\eta = (\alpha', n)$ is a dual index for cluster α' and basis function n, denotes the site-orbit for cluster α' radiating from site i. Each basis function, labeled n, for each symmetrically equivalent cluster β of prototype α' shares the same coefficient $V_{\Omega_\eta^i}$ in the linear expansion:

$$E^i(\{\vec{q}\}) = \sum_{\Omega_\eta^i} V_{\Omega_\eta^i} \frac{1}{|\alpha'|} \sum_{\beta \in \Omega_\eta^i} \Phi_{\Omega_\eta^i}(\vec{q}_\beta) \tag{6.9}$$

However, in a more general expansion we can take non-linear combinations of the

flower-tree summed basis functions as follows:

$$E^i(\{\vec{q}\}) \approx \mathcal{N}^i \left(\left\{ \sum_{\beta \in \Omega_\eta^i} \Phi_{\Omega_\eta^i}(\vec{q}_\beta) \right\} \right) \tag{6.10}$$

$$= \mathcal{N}^i \left(\left\{ \mathcal{G}_{\Omega_\eta^i} \right\} \right) \tag{6.11}$$

where $\mathcal{N}^i$ is a non-linear functional of the summed cluster basis function radiating from the i^{th} site.

Thus we are motivated to construct an artificial neural networks that takes as inputs $\left\{ \mathcal{G}_{\Omega_\eta^i} \right\}$ and outputs the energy of a crystal. That is

$$E = \sum_i \mathcal{N}^i \left(\left\{ \mathcal{G}_{\Omega_\eta^i} \right\} \right) \tag{6.12}$$

The site-based neural net model is summarized in Figure 6.2(a). In this scheme, each asymmetric unit is associated with a distinct neural net. Site energies are calculated for each site within the crystal and the contributions are summed for the total crystal energy.

6.2.5 Artificial Neural Network

Whether working in the site-based or cluster-based cluster expansion, we make use of artificial neural network models that take as inputs $\vec{x}$ (where x_i could be either the flower-tree summed basis functions in the site-based model, or simply the evaluated basis functions in the cluster based model) and output an energy e. Artificial neural networks are hierarchical recursive functions made up of activation nodes f_i which represents a non-linear function f at node i. A one-layer neural net produces output e from inputs $\mathbf{x}$

as follows:

$$e = b^{(1)} + \sum_j w_j^{(1)} f_j(b_j^{(0)} + \sum_k x_k W_{kj}^{(0)}) \tag{6.13}$$

where $b^{(1)}$ is a bias term associated with the 1st layer, and $b_j^{(0)}$, are bias terms associated with the input layer into node j of the first hidden layer.$W_{kj}^{(0)}$ represents the weight matrix connecting the input layer to the first hidden layer, and $w_j^{(1)}$ is the weight matrix connecting the hidden layer to the output layer. The model variables are the weights and biases which are trained through optimization techniques described below. The activation function can take several forms including the hyperbolic tangent, rectified linear unit, or logistic function. In this study we used the hyperbolic tangent exclusively.

6.2.6 Objective Function

In order to train the neural network model, we must define a convex objective function to minimize. In this case it is chosen to penalize differences in energies between the model and DFT, however it can be extended to penalize differences in forces if the derivatives of the model with respect to atomic displacements are known. The extension to forces is discussed further in the appendix. In general the objective function is the sum of squared errors between the model prediction and the DFT energy for each configuration σ over the whole data set:

$$\Gamma = \sum_\sigma \left(E_{\mathrm{ANN}}(\sigma) - E_{\mathrm{DFT}}(\sigma)\right)^2 \tag{6.14}$$

The objective function is minimized with respect to the weights of the neural network. Many optimization algorithms exist to optimize the weights of the network function, and we employed the Adam algorithm in this study.

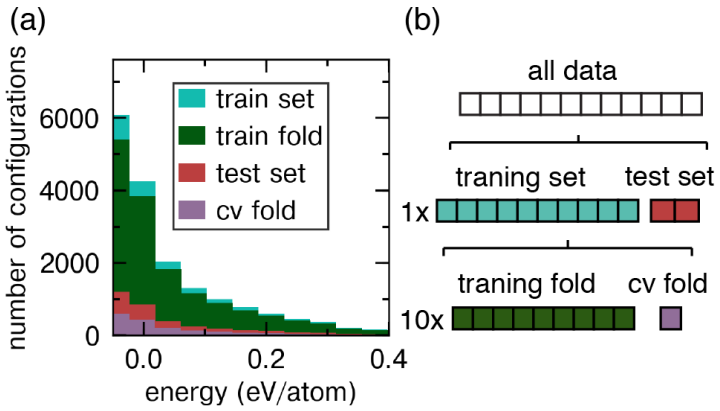

Figure 6.3: (a) Distribution of energies for all configurations in the database. (b) All data is split into a training set and test set. The training set is further subdivided into 10 training folds and 10 validation folds for use in hyperparameter tuning.

6.2.7 DFT

Density functional theory calculations were performed using the Vienna Ab Initio Simulation Package (VASP). [104, 105] A plane wave basis set with an energy cutoff of 400 eV was employed and projector augmented wave psuedopotentials (PAW). [106, 104] The GGA-PBEsol functional was used to approximate electron correlation and exchange. [166] Energies were converged to within 1 meV / atom with respect to k-point density and a 6×6×6 Γ-centered k-point mesh was used. The VESTA program suite was used to visualize crystal structures.

6.3 Training Set

The training set is a critical component in a machine learning problem. The resulting model is only as good as the training set. The most important regions of PES include the potential energy wells in which the ground state structure resides. Therefore, much effort was made to sample configurations near the ground state structure along with the structures associated with the intermediate tetragonal phase and the high temperature

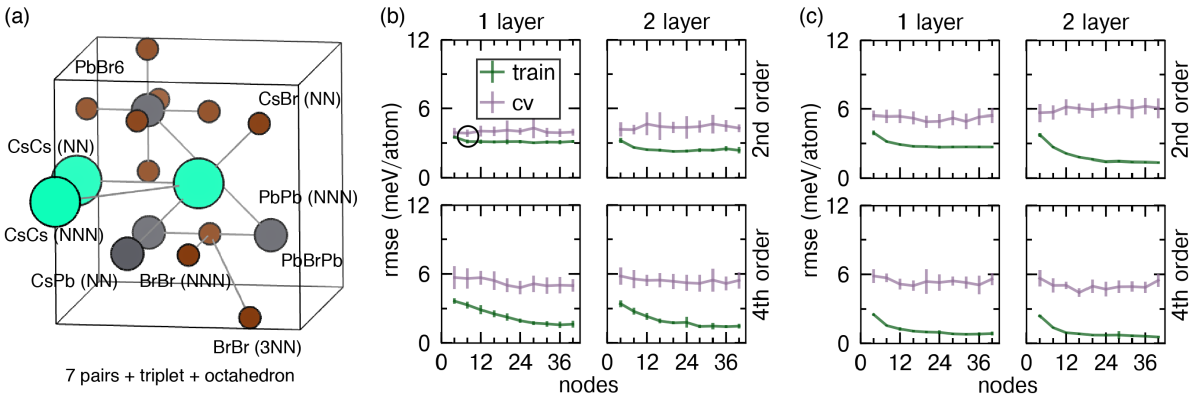

Figure 6.4: (a) Clusters used in final model which includes 7 pairs, 1 triplet, and 1 octahedron. Results of 10-fold cross validation for (b) cluster-based model and (c) site-based model. Training and validation (cv) average RMSE is plotted with error bars of 1 standard deviation. In (b,c), left columns indicate 1 hidden layer while right columns indicate 2 hidden layers and top rows indicate 2nd order models while the bottom row indicates 4th order models.

cubic phase.

Sampling the PES was done in several ways. The starting point began with the geometric relaxation of the 15 tilt systems as previously described in Bechtel2018. For each of these relaxed structures, systematic displacement enumerations were made in terms of symmetry-adapted displacement modes, i.e. the displacement fields that block diagonalize the crystal symmetry representation. The same supercell (2×2×2) was used for all of the tilt systems to avoid issues with differing k-point grids. Systematic strain enumerations were also included on the primitive perovskite structure, and the irreducible wedge of each subspace was sampled in the volume 1 cell. In addition to systematic enumerations, stochastic sampling of strains and displacements were made to generate more configurations. The strain and displacement fields were chosen at random from an n-sphere, and the correlations were compared to existing configurations to ensure uniqueness, i.e. that a very similar structure wasn't already included in the database. Also interpolations between structures were used for example between the three experimentally observed phases. In total, 31,000 configurations were calculated.

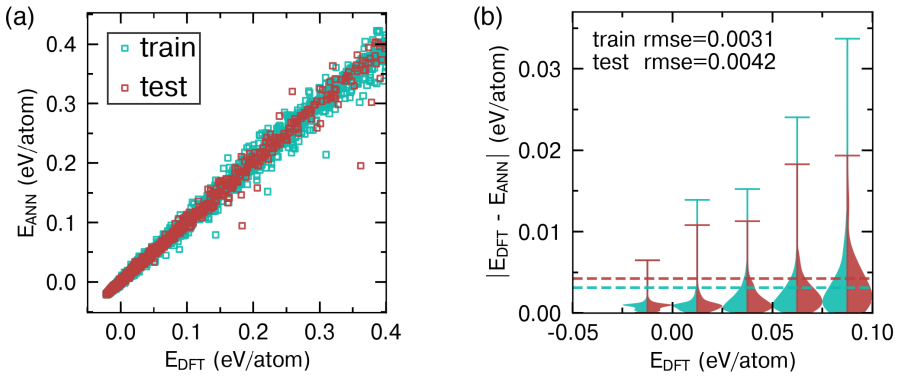

Figure 6.5: Fitting statistics for 1 layer 2nd order cluster-based model with 8 hidden nodes per layer. (a) ANN energy vs DFT energy shows that both training and test set show similar average error. (b) Distribution of errors for lowest 125 meV configurations binned into 25 meV bins. The red and green dashed lines indicate the RMSE over the entire test and training set resepectively. Low energy configurations show very low error.

6.4 Results

6.4.1 Model Training

After compiling the training database, we built a model selection pipeline as follows. Cluster selection is typically built into the model selection/cross validation schemes of cluster expansion Hamiltonians, however due to the number of hyperparameters involved in the models here, we restricted our model selection and hyperparamater tuning to 5 sets of clusters. Due to the covalent bonding of within the octahedra, octahedral cluster were included in all 5 sets that were considered. The five sets were built up as follows: (1) 4 pairs + 1 octahedron, (2) 5 pairs + 1 octahedron, (3) 8 pairs + 1 octahedron, (4) 4 pairs + 1 triplet + 1 octahedron, (5) 7 pairs + 1 triplet + 1 octahedron. For each model we tested several hyperparameters including number of hidden layers, number of nodes per hidden layer, and number of input features (up to 2nd or 4th order basis functions). This resulted in 400 different models that were tested using 10-fold cross validation resulting in over 4000 trained neural net models.

6.4.2 Hyperparameter Tuning

Validation and training sets can be used to tune the hyper parameters of the ANN. Here the total data set was split into a training set (80% of data), and a test set (20% of data). The test set was kept removed from any training iterations such that it remained an unbiased evaluator of model performance. K-fold cross validation with 10 folds was used to find the optimal hyper parameters (number of nodes, layers, and input features in the ANN model). In this training method, the training set (which makes up 80% of the total data) is further split up into a cv training set (90% of the full training set) and a cv test set (10% of the full training set). The model is trained only on the cv training set, and it is evaluated on the cv test set. This procedure is repeated 10 times such that all of the full training set data is used at least once.

Training neural nets requires an optimization routine to update the model variables and it is an important research area. We employed a batch training strategy over at least 1000 epochs per batch size, with batch sizes 2, 10, 100, and 1000, which typically yielded a well converged model in terms of the RMSE. The Adam optimization routine was used to update model weights and biases during training which incorporates momentum and per/weight learning parameters in the gradient descent.

In Figure 6.4, the training results for the best performing model is displayed. The model consists of basis functions generated from 7 pairs, 1 triplet, and 1 octahedral cluster as pictured in Figure 6.4(a). Four other combinations of clusters were tested as shown in the supporting information, but it was found that including more clusters, and especially including the triplet cluster resulted in more robust models. The neural net training results are displayed in Figures 6.4 for the (b) cluster-based model and the (c) site-based model. For each model, input features up to order 2 or order 4 basis functions were tested (rows of Figures 6.4(a,b)) as well as number of hidden layers (columns of

Figures 6.4(a,b)).

The site-based model and cluster-based perform similarly with several key differences. First, the cluster-based models generalize better to the validation set with smaller validation errors among all models tested. However, the site-based models achieve smaller errors on the training folds. Large differences between the training error and the validation error indicate that the models tend to overfit the training data and generalize poorly. However, the order 2 cluster-based model with 1 hidden layer performed the best in terms of generalizability with both the smallest validation error and the smallest difference between the training and validation errors. In particular the model with order 2 cluster-based model with 1 hidden layer and 8 nodes per hidden layer had the smallest validation error among all models and was therefore chosen as the best model according to the cross validation scheme.

6.4.3 ANN Fit Evaluation

After finding the optimal hyperparameters for our model (shown with the black circle on Figure 6.4(b) indicating the order 2 cluster-based model with 1 hidden layer of 8 nodes), we retrained the model on the full training set and calculated the error on the holdout set as shown in Figures 6.5(a,b). The training and test rmse were similar to those found in the hyperparameter tuning as expected. Additionally, we investigated the distribution of errors for different energy regions as shown in Figures 6.5(b). Interestingly, the model performs best for the lowest energies configuration, meaning that it faithfully reproduces the important ground state structures.

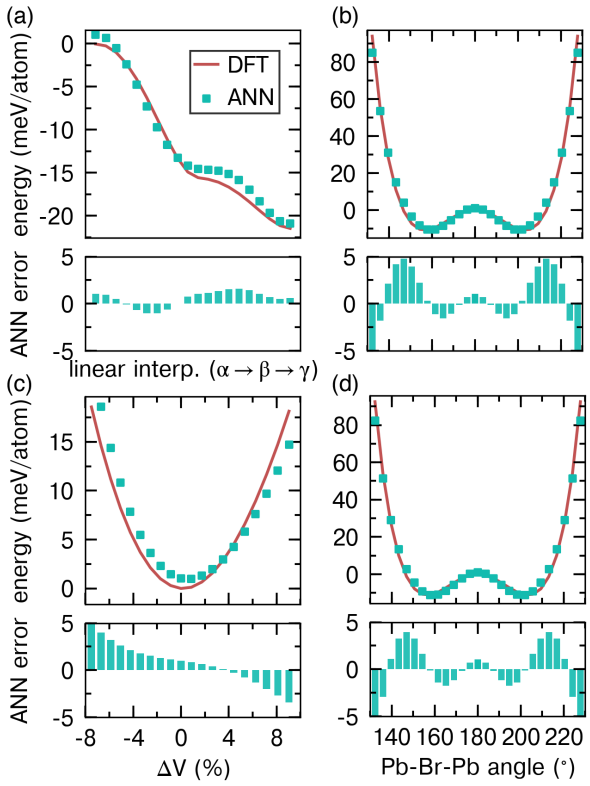

Figure 6.6: Model and DFT energies as a function of (a) a linear interpolation experimentally observed phases, (b) in-phase tilts, (c) volume, and (d) anti-phase tilts. In all cases, the ANN PES aligns well with the DFT energy surface.

6.4.4 DFT energy surfaces

Now we explore how the ANN traces the DFT potential energy surface along important paths. In Figure 6.6, we plot the energies as a function of (a) a linear interpolation experimentally observed phases, (b) in-phase tilts, (c) volume, and (d) anti-phase tilts. In all cases, the ANN PES aligns well with the DFT energy surface. Additionally,the ANN PES appears to be relatively smooth. In the supporting information we provide example fits for the overfitted models.

6.5 Discussion

The key points made by this paper are as follows:

1. We have extended the linear anharmonic vibrational cluster expansion as first detailed by Thomas and Van der Ven for the more general case of non-linear functionals of polynomial basis functions.

2. We have shown the alternative formulation for the CCD ANN, i.e. cluster-based and site-based, and have discussed the pros and cons of each.

3. We have trained CCD ANN models to a large database of DFT calculations and have achieved low errors as confirmed by cross validation.

4. We have shown how harmonic basis functions can be used to describe an anharmonic energy landscape through the use of non-linear activation functions in a neural net architecture.

6.6 Conclusions

The development of anharmonic vibrational hamiltonians is a challenging problem, however, by making use of machine learning techniques it is possible to capture a high degree of complexity that is present in the DFT energy landscape. When large DFT dataset on the order of 100,000 configurations are easily computable, there may be a point when anharmonic vibrational neural nets compete as a viable option for modeling the PES.

6.7 Appendix

The objective function can be extended to include forces as follows:

$$\Gamma = \epsilon \Delta E + (1-\epsilon)\Delta F \tag{6.15}$$

$$= \epsilon \sum_{\sigma} \left(E(\sigma) - E_{\mathrm{DFT}}(\sigma)\right)^2 \tag{6.16}$$

$$+ (1-\epsilon) \sum_{\sigma} \sum_{i} \left\| \vec{f^i}(\sigma) - \vec{f^i_{\mathrm{DFT}}}(\sigma) \right\|^2 \tag{6.17}$$

$$= \epsilon \sum_{\sigma} \left(\sum_{i} E^i(\sigma^i) - E_{\mathrm{DFT}}(\sigma) \right)^2 \tag{6.18}$$

$$+ (1-\epsilon) \sum_{\sigma} \sum_{i} \left\| \vec{f^i}(\sigma) - \vec{f^i_{\mathrm{DFT}}}(\sigma) \right\|^2 \tag{6.19}$$

which requires forces computed from the Network function. The calculation of the forces are described below. Forces can be computed from the following:

$$f^{i'}_{\alpha'} = \frac{\partial}{\partial r^{i'}_{\alpha'}} E \tag{6.20}$$

$$= \frac{\partial}{\partial r^{i'}_{\alpha'}} \sum_{i} E^i \left(\left\{ \mathcal{G}_{\Omega^i_\eta} \right\} \right) \tag{6.21}$$

$$= \sum_{j \in \mathrm{NL}} \frac{\partial}{\partial r^{i'}_{\alpha'}} E^j \left(\left\{ \mathcal{G}_{\Omega^j_\eta} \right\} \right) \tag{6.22}$$

$$= \sum_{j \in \mathrm{NL}} \frac{\partial}{\partial r^{i'}_{\alpha'}} \mathcal{N}^j \left(\left\{ \mathcal{G}_{\Omega^j_\eta} \right\}, \{w_\gamma\} \right) \tag{6.23}$$

$$= \sum_{j \in \mathrm{NL}} \sum_{\eta} \frac{\partial \mathcal{N}^j}{\partial \mathcal{G}_{\Omega^j_\eta}} \frac{\partial \mathcal{G}_{\Omega^j_\eta}}{\partial r^{i'}_{\alpha'}} \tag{6.24}$$

Hence we split the derivative into a derivative of the Network function $\mathcal{N}$ with respect to the inputs $\mathcal{G}$ which is computable from automatic differentiation schemes implemented in modern nueral network codes (TensorFlow) and the derivative of the input with respect

to position.

$$\frac{\partial \mathcal{G}_{\Omega_\eta^j}}{\partial r_{\alpha'}^{i'}} = \frac{\partial \sum_{\beta \in \Omega_\eta^j} \Phi_{\Omega_\eta^j}(\vec{q}_\beta)}{\partial r_{\alpha'}^{i'}} \tag{6.25}$$

$$= \sum_{\beta \in \Omega_\eta^j} \frac{\partial \Phi_{\Omega_\eta^j}(\vec{q}_\beta)}{\partial r_{\alpha'}^{i'}} \tag{6.26}$$

$$= \sum_{\beta \in \Omega_\eta^j} \sum_k \frac{\partial \Phi_{\Omega_\eta^j}(\vec{q}_\beta)}{\partial q_k} \frac{\partial q_k}{\partial r_{\alpha'}^{i'}} \tag{6.27}$$

$$= \sum_{\beta \in \Omega_\eta^j} \sum_k \frac{\partial \Phi_{\Omega_\eta^j}(\vec{q}_\beta)}{\partial q_k} \frac{\partial q_k}{\partial r_{\alpha'}^{i'}} \tag{6.28}$$

$$\tag{6.29}$$

Now we compute the derivatives of the CCDs with respect to position, in this case specifying the LogCCD functor.

$$\frac{\partial q_k}{\partial r_{\alpha'}^{i'}} = \frac{\partial}{\partial r_{\alpha'}^{i'}} \sum_l Q_{kl} f(d_l^2, d_{l_0}^2) \tag{6.30}$$

$$= \frac{\partial}{\partial r_{\alpha'}^{i'}} \sum_l Q_{kl} \ln(d_l^2/d_{l_0}^2)/2 \tag{6.31}$$

$$= \frac{\partial}{\partial r_{\alpha'}^{i'}} \sum_l Q_{kl} [\ln(d_l) - \ln(d_{l_0})] \tag{6.32}$$

$$= \sum_l Q_{kl} \frac{\ln(d_l)}{\partial r_{\alpha'}^{i'}} \tag{6.33}$$

$$= \sum_l Q_{kl} \frac{1}{d_l} \frac{\partial d_l}{\partial r_{\alpha'}^{i'}} \tag{6.34}$$

$$\tag{6.35}$$

The derivative of pair distances with respect to position is given as follows:

$$\frac{\partial d_l}{\partial r^{i'}_{\alpha'}} = \frac{\partial}{\partial r^{i'}_{\alpha'}} \left(\sum_{\alpha} (r^m_\alpha - r^n_\alpha)^2 \right)^{1/2} \tag{6.36}$$

$$= \frac{1}{2} \left(\sum_{\alpha} (r^m_\alpha - r^n_\alpha)^2 \right)^{-1/2} \frac{\partial}{\partial r^{i'}_{\alpha'}} \sum_{\alpha} (r^m_\alpha - r^n_\alpha)^2 \tag{6.37}$$

$$= \frac{1}{2d_l} 2(r^m_{\alpha'} - r^n_{\alpha'}) \frac{\partial}{\partial r^{i'}_{\alpha'}} (r^m_{\alpha'} - r^n_{\alpha'}) \tag{6.38}$$

$$= \frac{1}{d_l} (r^m_{\alpha'} - r^n_{\alpha'}) \begin{cases} 1 & i' = m \\ -1 & i' = n \\ 0 & \text{else} \end{cases} \tag{6.39}$$

Putting it all together, we get:

$$f^{i'}_{\alpha'} = \sum_{j \in \mathrm{NL}} \sum_{\eta} \frac{\partial \mathcal{N}^j}{\partial \mathcal{G}_{\Omega^j_\eta}} \frac{\partial \mathcal{G}_{\Omega^j_\eta}}{\partial r^{i'}_{\alpha'}} \tag{6.40}$$

$$= \sum_{j \in \mathrm{NL}} \sum_{\eta} \frac{\partial \mathcal{N}^j}{\partial \mathcal{G}_{\Omega^j_\eta}} \sum_{\beta \in \Omega^j_\eta} \sum_{k} \frac{\partial \Phi_{\Omega^j_\eta}(\vec{q}_\beta)}{\partial q_k} \frac{\partial q_k}{\partial r^{i'}_{\alpha'}} \tag{6.41}$$

$$= \sum_{j \in \mathrm{NL}} \sum_{\eta} \frac{\partial \mathcal{N}^j}{\partial \mathcal{G}_{\Omega^j_\eta}} \sum_{\beta \in \Omega^j_\eta} \sum_{k} \frac{\partial \Phi_{\Omega^j_\eta}(\vec{q}_\beta)}{\partial q_k} \sum_{l} Q_{kl} \frac{1}{d_l} \frac{\partial d_l}{\partial r^{i'}_{\alpha'}} \tag{6.42}$$

$$= \sum_{j \in \mathrm{NL}} \sum_{\eta} \frac{\partial \mathcal{N}^j}{\partial \mathcal{G}_{\Omega^j_\eta}} \sum_{\beta \in \Omega^j_\eta} \sum_{k} \frac{\partial \Phi_{\Omega^j_\eta}(\vec{q}_\beta)}{\partial q_k} \sum_{l} Q_{kl} \frac{1}{d_l^2} (r^m_{\alpha'} - r^n_{\alpha'}) \times \begin{cases} 1 & i' = m \\ -1 & i' = n \\ 0 & \text{else} \end{cases} \tag{6.43}$$

Thus we have for the energy :

$$E = \sum_i E^i \tag{6.44}$$

$$= \sum_i \mathcal{N}\left(\left\{\mathcal{G}_{\Omega_\eta^i}\right\}, \{w_\gamma\}\right) \tag{6.45}$$

$$\tag{6.46}$$

And for the forces:

$$\vec{f}^{i'} = \sum_{j \in \mathrm{NL}} \sum_\eta \frac{\partial \mathcal{N}^j}{\partial \mathcal{G}_{\Omega_\eta^j}} \nabla \mathcal{G}_{\Omega_\eta^j} \tag{6.47}$$

$$= \vec{f}^{i'}\left(\left\{\mathcal{G}_{\Omega_\eta^j}\right\}, \{w_\gamma\}, \left\{\frac{\partial \Phi_{\Omega_\eta^j}}{\partial q}\right\}\right) \tag{6.48}$$

Chapter 7

Machine-learning parameterization of an anharmonic vibrational effective Hamiltonian for octahedral tilting transitions in perovskites

7.1 Introduction

Vibrational excitations in solids play an important role in structural, thermodynamic, and electronic properties of materials. [192] First principles calculations have proven successful in reproducing the harmonic phonon dispersions for materials in their equilibrium ground state. [193] However, many technologically relevant phases exist in metastable or dynamically unstable phases stabilized by anharmonic vibrational excitations. In these cases, harmonic approximations fail, and higher order terms are necessary to capture structural instabilities. For instance, halide perovskite materials undergo successive symmetry lowering distortions upon cooling due to unstable octahedral tilt modes, cubic-

to-tetragonal phase transitions are observed in ZrH_2 [64] and Jahn-Teller distortions in layered oxide battery materials lead structural phase transitions.

Several approaches exist to model anharmonic lattice dynamics and temperature-dependent structural phase transitions. The most straightforward but computationally expensive approach is to perform ab initio molecular dynamics in order to obtain thermodynamic averages as a function of temperature. [194, 195, 196, 197] However, the computational cost of such simulations restricts supercell size which can introduce finite-size effects. Another approach involves explicitly adding terms to an effective hamiltonian that capture the relevant instabilities and then fitting the model to first principles calculations. This approach was applied to polar and octahedral tilting distortions in oxide perovksites in the early work of Rabe, Waghmare, and Zhong. [198, 199, 200, 201, 118, 119, 202, 203, 204, 205, 206, 207, 208] More recently, generalized anharmonic vibrational cluster expansion effective Hamiltonians enumerate basis functions in terms of cluster normal modes. [64, 178] Model parameters are fit to a database of first principles calculations, and Monte Carlo simulations allow for the calculation of thermodynamic averages. Using this technique, order parameters can be calculated as a function of temperature which can be used to determine structural phase transition temperatures.

While the anharmonic vibrational cluster expansion provides a general approach to vibrational effective Hamiltonians, where one allows the fitting procedure to identify which instabilities to include in the model, obtaining an appropriate fit can be extremely challenging for several reasons. First, unlike a configurational cluster expansion, a vibrational effective Hamiltonian has the additional constraint of requiring a convex energy landscape. Including this constraint in least squares fitting is a non-trivial task. Second, since vibrational cluster expansions are based on continuous atomic displacements degrees of freedom as opposed to discrete configurational variables, there is an additional approximation associated with the cut-off in the degree of the polynomial basis func-

tions. Hence, the number of fitting parameters in such models becomes very large as larger clusters and higher order basis functions are included.

To overcome the challenges in fitting the potential energy surface with generalized linear models, many recent attempts have been made to apply more sophisticated machine learning techniques to mapping the DFT potential energy surface. [73, 179, 180, 181, 182, 183, 184, 185, 186, 187, 188, 189, 190, 191]. Most of these approaches involve identifying appropriate descriptors, which are often built using pair distances and angles between atoms, and then using a machine learning regression technique ranging from linear regression to artifical neural networks. While these methods can reproduce the potential energy surface with low error, they often extrapolate poorly making them ill-suited for large scale Monte Carlo simulations.

In this work, we reparameterize a neural network model of the potential energy surface in order to guarantee a convex energy landscape which allows for Monte Carlo simulations. By focusing on reproducing low energy configurations we are able to succesfully reproduce qualitative features of the structural phase transitions in $CsPbBr_3$, an inorganic halide perovskite which undergoes phase transitions associated with octahedral tilting and A-cation displacements. Interestingly, we also show how energy barriers between the observed phases dictate regions of phase stability.

7.2 Results

7.2.1 DFT

The Vienna Ab Initio Simulation Package (VASP) was used to carry out density functional theory (DFT) calculations. [104, 105] For all calculations, the GGA-PBESol functional was employed wth projector augmented wave pseudopotentials with a 400 eV

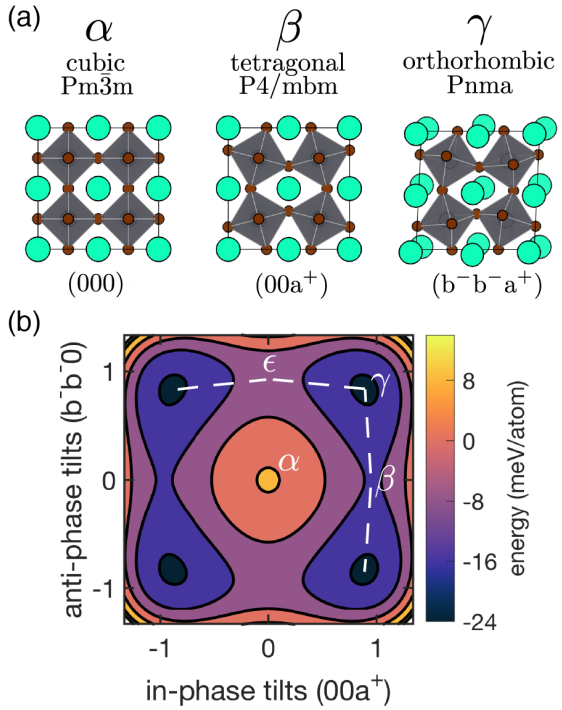

Figure 7.1: (a) DFT relaxations of the experimentally observed phases of $CsPbBr_3$. DFT energy surface for configurations with orthorhombic lattice parameters as a function of octahedral tilts. For each configuration, the $PbBr_6$ sublattice and lattice parameters were held fixed while the Cs sublattice was allowed relax. The resulting energy landscape indicates that the cubic phase exists as a local maximum, the tetragonal phase exists at a saddle point, and the ground state orthorhombic phase exists as a stable minimum.

cutoff for the plane wave basis set. [166, 106, 104] A 6×6×6 Γ-centered k-point mesh was used which resulted in energy convergence to within 1 meV / atom. Crystal structures were visualized using the VESTA program suite.

7.2.2 Perovskite Energy Surface

First we review the DFT energy landscape that captures the transition pathways between the low temperature orthorhombic γ-phase (Pnma), the tetragonal β-phase (P4/mbm), and the cubic α-phase (Pm$\bar{3}$m) as pictured in Figure 7.1. For a detailed description see Bechtel and Van der Ven 2018. Briefly, the tetragonal phase is achieved

from the cubic phase by the activation of in-phase tilt modes denoted ($00a^+$) in Glazer notation, which indicates tilts about the z-rotation axis of amplitude a. Further, the orthorhombic phase is obtained from the tetragonal phase by activating two simultaneous anti-phase tilts about the x and y rotation axes resulting in the ($b^-b^-a^+$) tilt pattern. As shown in Figure 7.1(b), the tetragonal phase exists as a saddle point between orthorhombic variants. Another phase denoted as the ϵ-phase with (b^-b^-0) tilts also resides at a saddle point between orthorhombic γ variants. However, due to the smaller energy barrier through the β-phase, the system prefers to sample orthorhombic variants via the β-phase resulting in an average tetragonal strucure upon warming. In this study we will further explore the relationship between the competing energy barrier heights and the transition temperatures at which the orthorhombic to tetragonal and tetragonal to cubic transitions occur.

7.2.3 Minimal Cluster Model

We now build upon previous work in modeling the potential energy surface using cluster-based neural network models. Cluster-based neural networks model the crystal energy as a sum of cluster energies. An energy function is trained for each type of cluster considered. Interestingly, due to the non-linear activation functions of neural networks, anharmonic energy landscapes can be reproduced using only harmonic basis function inputs. As described by Bechtel et al., cluster-based neural network models can be constructed which map the DFT potential energy surface with low error. However, it was shown that these models typically generalize poorly. In addition, neural networks can behave unpredictably in under represented regions within the feature space. In initial tests, we found that Monte Carlo simulations always found spurious ground states during equilibration of neural network effective Hamiltonians. Furthermore, neural network

models are slow to evaluate compared to polynomial models which restricts the feasbility of large scale Monte Carlo simulations. For these reasons we now develop a framework to extract a more suitable effective Hamiltonian from the neural network model with the following chracteristics: (1) fast to evaluate, (2) smooth energy surface as a function of atomic displacements, and (3) a convex energy landscape.

For fast evaluations we chose to work with polynomial functions of the neural network inputs. In other words for each cluster we find a low order polynomial approximation to the neural network energy landscape which can be expressed as follows:

$$E = \sum_{\alpha} \mathcal{N}^{\alpha} \tag{7.1}$$

$$\approx \sum_{\alpha} \sum_{i} V_i^{\alpha} \Phi_i^{\alpha}(\boldsymbol{q}) \tag{7.2}$$

where α represents a cluster in the crystal, $\mathcal{N}^{\alpha}$ is the neural network cluster model, $\Phi_i^{\alpha}(\boldsymbol{q})$ is the ith polynomial basis function for cluster α and V_i^{α} is its fitting coeffecient or effective cluster interaction (ECI). Using polynomials is both fast to evaluate and it guarantees the second criteria of smoothness. In order to meet the third criteria for a suitable effective Hamiltonian we ensure that the fitting coefficient (ECI) of the highest order term for a cluster is positive.

An example of this fitting procedure is depicted in Figure 7.2(d-h). In this work we base all of our models on the simplest cluster-based neural network models presented in Bechtel et al. which include five distinct clusters with basis functions up to second order. Furthermore, we only consider the neural network models with one hidden layer. In Figure 7.2(d-h) we see the energy landscape of each cluster as a function of the q_0 displacement mode. For pair clusters there is simply one displacement degree of freedom representing the distance between atoms. For larger clusters of N atoms there are $3N-6$

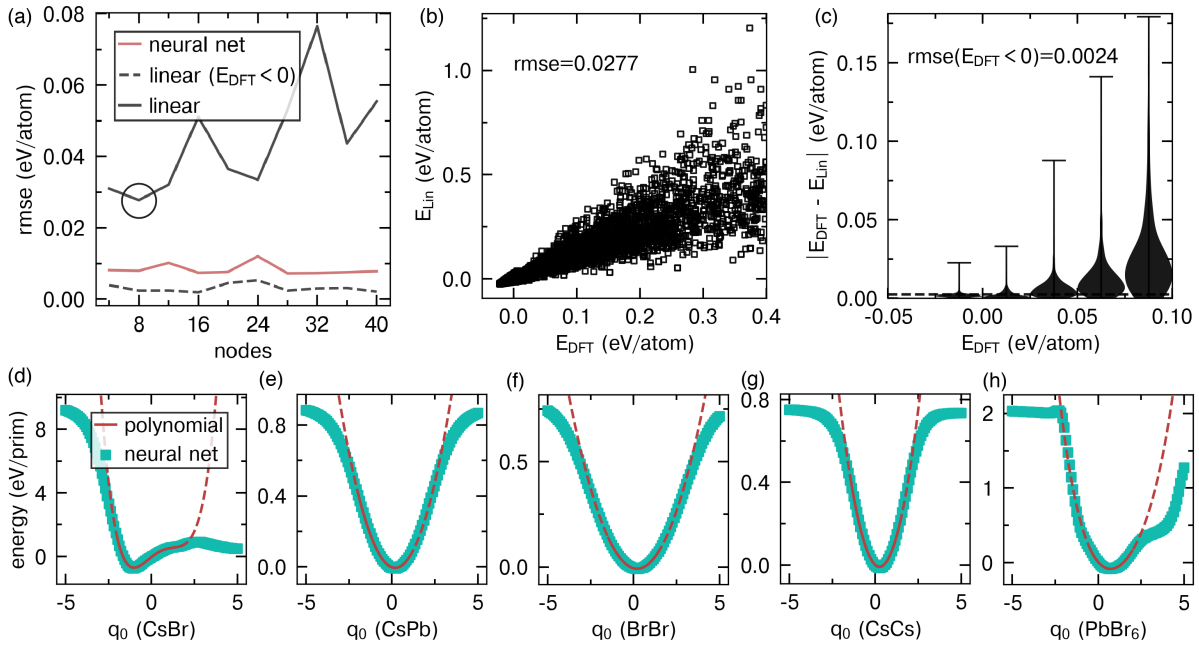

Figure 7.2: (a) Root mean square error (rmse) of 1-hidden layer neural network models with four pair clusters and one octahedral cluster plotted as a function of nodes per hidden layer. Linear models were used to reparameterize the neural net models and the total rmse (black line) and rmse for configurations with energy less than the cubic reference ($E_{\mathrm{DFT}} < 0$) (dashed black line) are plotted for each model. The circled point corresponds to the best performing linear reparameterized model, which is reffered to as E_{Lin}. (b) E_{Lin} vs E_{DFT} for all configurations. Large errors are observed for high energy configurations with a total rmse of 0.0277 eV/atom. (c) Violin plot of errors between linear model and DFT for 0.025 eV energy bins. The violins show the distribution of errors for each energy bin and the dashed dotted line represents the rmse for configurations in the lowest energy bin with $E_{\mathrm{DFT}} < 0$ which is 0.0024 eV/atom.(d-h) Energy landscapes as a function of q_0 (volumetric deformation) for each cluster considered. The teal markers indicate the energy of the neural netwokr function and the red line shows the polynomial model used as a reparameterization. The solid red region corresponds to the region which was included in the fitting procedure.

displacement degrees of freedom which separate into irreducible subspaces when building polynmial basis functions that are invariant to the crystal symmetry. For the octahedral cluster, we fit the energy contributions from each irreducible subspace separately by setting all other subspace basis functions to zero and fitting calculating the resulting energy. Depictions of these polynomial fits are shown in the Supporting Information, but here we focus on the q_0 functions which represent pair distances in the case of pair

clusters and volumetric deformations in the case of larger clusters.

As shown in Figure 7.2(d-h), the cluster energy functions as predicted by the neural network model typically have minima near $q_0 = 0$ which represents the reference distance of that cluster in the high-temperature cubic phase. For small deformations, the energy behaves mostly harmonically, but can deviate substantially at high deformation. Hence, we chose to approximate the neural network energies for CsPb, BrBr, and CsCs (Figures 7.2(e,f,g)) with a second order polynmial of the form $e = ax + bx^2$. By fitting these polynomial models only in the region near the minima we were able to gaurantee convex energy functions. For the CsBr and $PbBr_6$ clusters (Figures 7.2(d,h)), the neural network energy shows both a shift in the location of the minimum and the appearance of higher order features in the energy landcsape near the minima. Thus, for these clusters we employed a fourth order polynomial approximation to the neural network energy of the form $e = ax + bx^2 + cx^3 + dx^4$, and fit the coefficients using data near the minimum, ensuring that the resulting model had a positive coefficient for the fourth order term ($d > 0$).

This process was carried out for all second order, one-layer neural networks as described previously, and the root mean square errors for the linearized models and the neural network models are summarized in Figure 7.2(a). While the neural network models tend to have smaller overall errors around 8 meV compared to around 40 meV for the reparamaterized linear models, we see that the linearized models still perform well for low energy (i.e. energies lower than the cubic high temperature phase, $E_{\mathrm{DFT}} < 0$).

The best performing linear model was that fit to the 8 node, 1 layer, 2nd order neural network model which is circled in Figure 7.2(a). The linearized model energies are compared to DFT energies in Figure 7.2(b), and large errors are observed for high energy configurations as expected due to the fitting procedure that focuses on the minimum energy regions of the cluster functions. Intersetingly, however, the errors for low energy

configurations are relatively small, around 3 meV, as shown in Figure 7.2(c). The cluster energy functions of the 8-node, 1-layer, 2nd order neural network and the reparameterized linear model is depicted in Figure 7.2(d-h).

Next we plot how the linearized model reproduces the DFT energy landscape in Figure 7.3. The linearized model reproduces many of the qualitative featurs of the energy surface with several key discrepencies. The simplified linear model, based upon only four pairs and one octahedral cluster, remarkably reproduces minima corresponing to orthorhombic γ-phase configurations. At regions of large tilts the linearized model severely overestimates the energy. This likely comes from the fact that the cluster energy functions were only fit in small regions near the minima resulting in overstimation of a cluster's energy for large deformations. Interestingly, the linear model also overstimates the saddle point energy for the ϵ-phase.

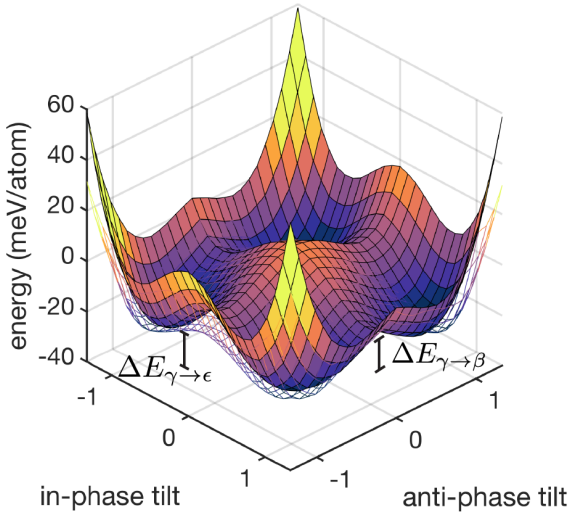

Figure 7.3: Linearized model energy landscape (surface) compared to the DFT energy landscape (mesh). Energy barriers through the ϵ-phase and β-phases are depicted and labeled $\Delta E_{\gamma\to\epsilon}$ and $\Delta E_{\gamma\to\alpha}$ resepectively. The linear model reproduces many of the qualitative features of the DFT energy landscape; however it overestimates the energy barrer $\Delta E_{\gamma\to\epsilon}$.

7.2.4 Monte Carlo

Having constructed a simplified model that reproduces the qualitative features of the DFT ground state energy landscape, we next turned to finite temperature Monte Carlo simulations in order to investigate structural phase transition as a function of temperature. Monte Carlo simulations were performed using an extension of the code developed by Thomas et al. Thermodynamic averages are computed once the system has equilibrated, typically around 2000-4000 passes, and averages are taken for 4000 passes. In order to avoid complications with differently oriented crystal variants, we first find the ground state structure in a small supercell and use it to seed simulations in larger supercells ensuring that all simulations equilibrate within the same orientational variant.

The Monte Carlo experiments are carried out by first using a simulation cell containing 1000 primitive volumes (5000 atoms) over a course temperature grid (20 K increments). Once the location of the phase transition is identified another Monte Carlo experiment is performed using a simulation cell of 4096 primitive volumes (20,480 atoms) over a fine temperature grid (1 K increments). These results are then used to estimate the tranisition temperatures.

Thermodynamic averages of the deformation tensor and atomic displacements were used to analyze the evolution of local and average structure as a function of temperature. We present the Monte Carlo results using the linearized effective Hamiltonian discussed in the previous section in Figure 7.4. The lattice parameters of the supercell are normalized by the number of primitive volumes contained in the simulation box. We also compute the cubic Hencky strain order parameters as shown in Figure 7.4(d).

Over the 20 K grid it appears that only one phase transition occurs from the orthorhombic γ-phase to the cubic α-phase as indicated by the decay of the e_3 and e_6 strain order parameters. However, when analyzed using a larger simulation cell and a

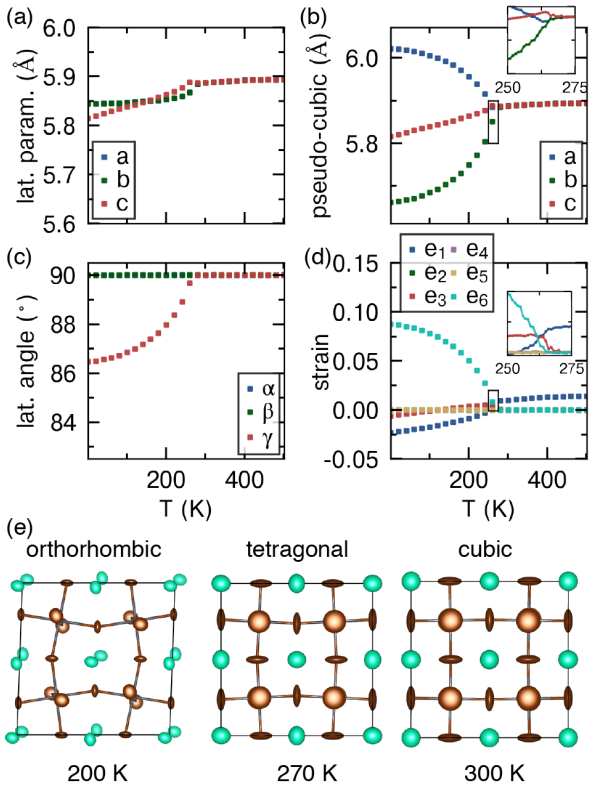

Figure 7.4: Thermodynamically averaged (a) lattice parameters, (b) lattice angles, (c) pseudo-cubic lattice parameters and strain order parameters from Monte Carlo simulations using the linearized CCD model. One phase transition from the low temperature orthorhombic phase to the high temperature cubic phase is observed, and the representative strutures are shown in (e) and (f) where thermodynamically averaged diplacement covariances were used to compute the anisotropic displacement parameters. ADP ellipsoids enclose 90% of the cumulative probability density of atomic motion.

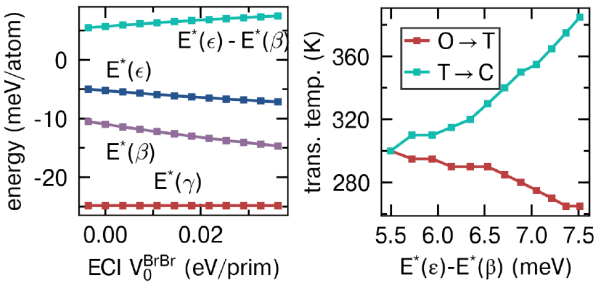

Figure 7.5: (a) Rescaled model energies of the tetragonal β-phase $E^*(\beta)$, orthorhombic ϵ-phase $E^*(\epsilon)$, orthorhombic γ-phase $E^*(\gamma)$ and the difference in energy barriers,$E^*(\beta)-E^*(\epsilon)$. The energy of the model ground state γ-phase was held fixed at the value of the DFT γ-phase in order to compare the effect of lowering the tetragonal saddle point energy ($E^*(\beta)$) and increasing the difference between energy barriers. (b) Transition temperatures as a function of barrier height difference between the γ-phase and the ϵ-phase. As the β-phase energy decreases and the difference in barriers increases, the tetragonal phase is stabilized.

finer temperature grid, two transitions were identified. First, an orthorhombic to tetragonal transition occurs as e_6 strain order parameter reaches zero at around 269 K. Then a second transition from tetragonal to cubic occurs as the e_3 strain order parameter goes to zero at about 274 K.

To visualize the crystal structures of the different phases, we average the atomic coordinates and displacement covariance matrices within a volume 8 supercell which are presented in Figure 7.4(d) for the observed orthorhombic, tetragonal and cubic phases. The structures reproduce the tilt modes and A-cation displacements of the experimentally observed γ and α phases. Remarkably the anisotropic displacement parameters also closely match those observed experimentally. In particular the high temperature cubic phase shows very large pancake-shaped Br ADPs indicating a high degree of motion in only one plane. These correspond to highly anharmonic lattice dynamics associated with octahedral tilting of the $PbBr_6$ inogranic sublattice.

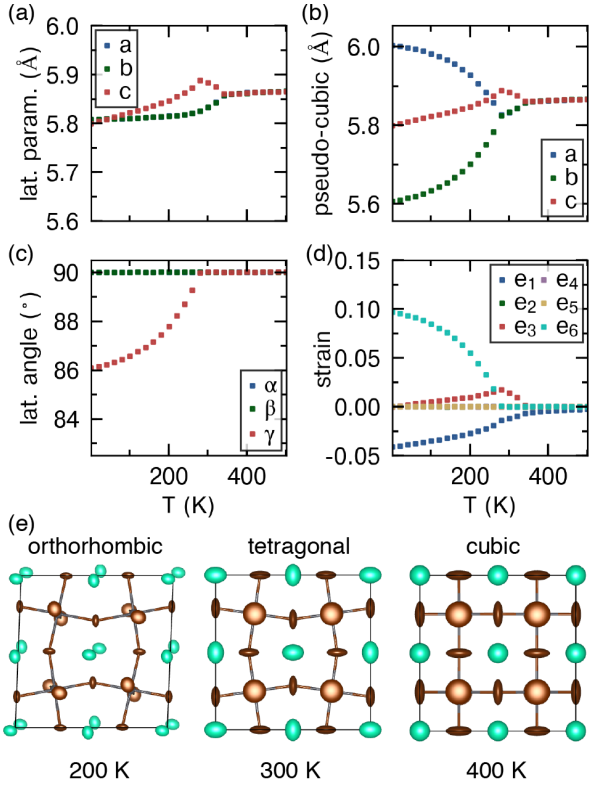

Figure 7.6: Thermodynamically averaged (a) lattice parameters, (b) lattice angles, (c) pseudo-cubic lattice parameters and strain order parameters from Monte Carlo simulations using the linearized CCD model. One phase transition from the low temperature orthorhombic phase to the high temperature cubic phase is observed, and the representative strutures are shown in (e) and (f) where thermodynamically averaged diplacement covariances were used to compute the anisotropic displacement parameters. ADP ellipsoids enclose 90% of the cumulative probability density of atomic motion.

7.2.5 Stabilizing the Tetragonal Phase

The Monte Carlo results of the linearized effective Hamiltonian qualitatively reproduced the two phase transitions observed experimentally, but showed only a small window for tetragonal phase stability. The small temperature window of stability for the tetragonal phase is even more surprising given the large overstimation of the ϵ-phase compared to DFT as shown in Figure 7.3.

In order to stabilize the tetragonal phase we explored ways to artificially decrease

the energy barrier through the tetragonal β-phase relative to the ϵ-phase. In particular, we varied the first order term, V_0^{BrBr} of the BrBr pair energy functional (i.e. a in $e = aq_0 + bq_0^2$). In order to maintain a consistent energy scale for comparing the effect of energy barrier heights we rescaled the energy of the model for each value of V_0^{BrBr} according to $E^* = E^{\mathrm{Lin}} \cdot (E^{\mathrm{DFT}}(\gamma)/E^{\mathrm{Lin}}(\gamma))$ where E^{Lin} is the model energy, $E^{\mathrm{DFT}}(\gamma)$ is the ground state DFT energy of the orthorhombic γ-phase (-24.79 meV/atom) and $E^{\mathrm{Lin}}(\gamma))$ is the model energy of the γ-phase before rescaling. This has the effect of fixing the ground state energy that the model produces for the γ-phase while allowing the energy barriers to shift relative to the ground state as pictured in Figure 7.5(a). By varying V_0^{BrBr} the energies of both the ϵ-phase and β-phase decrease in energy however the difference between their energies increases indicating that the β-phase is being stabilized relative to the ϵ-phase.

After constructing rescaled effective Hamiltonians for varying values of V_0^{BrBr}, we again performed Monte Carlo simulations for each of these models to determine the effect of shifting energy barriers relative to the γ-phase ground state. Due to computational constraints, we evaluated the rescaled models within a 1728 volume simulation cell at 5 K temperature increments which limits the resolution at which we can assign accurate transition temperature. The resulting transition temperatures are plotted against the difference in energy barrier in Figure 7.5(b). For the rescaled model with no change in energy barriers, there are two transitions, as previously pointed out, however the region of stability is too small to be uncovered at the temperature resolution used. As the difference in energy barriers increases, the tetragonal phase becomes stabilized resulting in two distinct phase transitions with diverging transition temperatures. When the β-phase decreases in energy it results in lower transition temperatures for the orthorhombic to tetragonal transition while increasing the transition temperature between the tetragonal and cubic phases.

An example of the Monte Carlo results for a tetragonally-stabilized model is given

in Figure 7.6(a), which clearly show distinct regions for the three phases. Again, we plot examples of the average structure along with the ADPs derived from the thermodynamically averaged displacement covariance matrices. Both the orthorhombic and cubic phases show the same distinctive behavior as in the unscaled model; however, the tetragonal phase shows an additional anisotropy of the Cs displacements with a football shaped thermal ellipsoid.

7.2.6 Octahedral Tilts across Transitions

With a parameteric model that stabilizes the tetragonal phase and reproduces many of the qualitative features of the anisotropic thermal displacements, we focus now on understanding the role of octahedral tilts throughout the successive phase transitions. The phase transitions in inorganic halide perovskites are often described in terms of the collective tilt modes of the halide sublattice. With our microscopic model we are in a unique position to explore the local environment due to octahedral tilts as shown in Figure 7.7(a).

Specifcally, we collected extrinsic Euler rotation angles for all octahedra in the simulation cell after every Monte Carlo pass. In order to obtain the Euler angles, first the Kabsch algorithm is applied to find the optimal rotation matrix that minimizes the squared distances between the rotated and non-rotated octahedron. The rotation matrix was then decomposed into elementary extrinsic Euler angles.

We plot histograms of the individual octahedral rotations for each phase in Figure 7.7(b). In the orthorhombic phase there exist bimodal peaks in the distribution for each Euler angle. In these simulations the in-phase rotation takes place about the z-axis, while the out-of-phase rotations occur along the a and b axes. We see the progression in octahedral rotations between the orthorhombic and tetragonal phases as the bimodal

peaks along a and b combine to a single peak centered at zero in the tetragonal phase. Likewise, the in-phase tilting peaks coalesce into one peak centered at 0 upon warming to the cubic phase. The distributions are shown as a function of temperature in Figure 7.7(e) where it is observed that the rotations serve as order parameters through the two phase transitions.

7.3 Discussion

While machine learning approaches have been shown to reproduce the DFT energy landscape with low error, they are typically not suitable for Monte Carlo simulations due to (1) high computational cost, (2) non-smooth and (3) non-convex energy landscapes. We have shown how the results of a cluster-based neural net model can be reparameterized at the cluster level using simple polynomial approximations. In this way, we are able to build an easily interpretable model that meets the three criteria enumerated above.

For example, from the polynomial reparameterization shown in Figure 7.2(d-h), we can identify certain features of the cluster energy functions that provide key physical insights. Interestingly, the CsBr bond shows a minima at low q corresponding to a tendency to prefer shorter bond lengths. This simple functional form conveys much of the intuition surrounding perovskite phase transitions as described by concepts such as the tolerance factor. That is, tilting transitions are thought to originate due to an undersized A−site cation which results in an under coordinated cation by bond valence sum arguments. Octahedral tilting occurs during cooling in order to satisfy the A-site cation's coordination environment. Therefore the minimum in the CsBr pair energy can be inuitively explained by the desire to satisfy the Cs atom's under coordination by being closer to the Br sublattice.

By fitting simple polynomials to the ANN functions, we constructed a minimal model

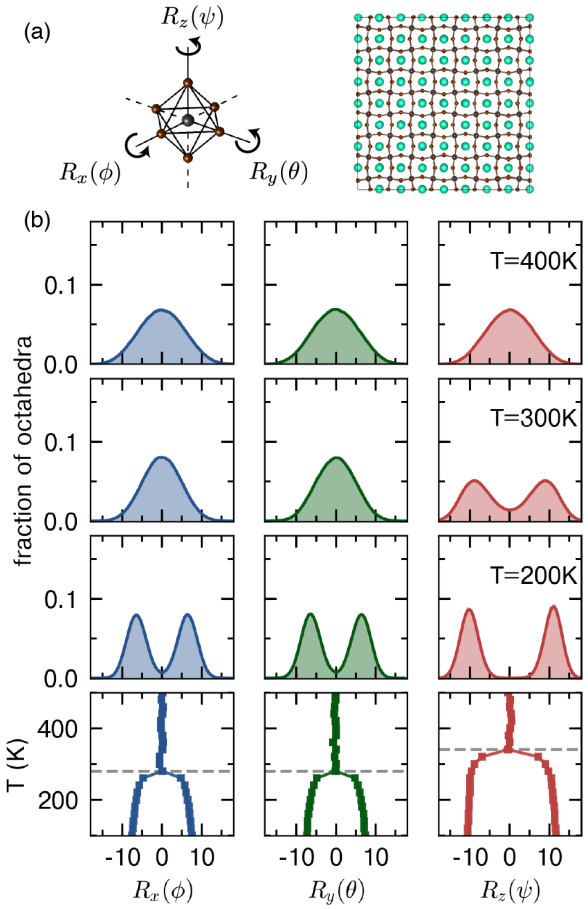

Figure 7.7: (a) Diagram of the extrinsic rotation Euler rotations about the x, y, and z rotation axes denoted by ψ, ϕ, and θ, respectively. Also pictured is the 512-volume simulation cell from which histograms of octahedral rotations were collected. Histograms of octahedral rotation angles fit with Gaussian kernel density esitmation at (b) 400 K, (c) 300 K and (c) 200 K representing the distribution of tilts in the cubic, tetragonal, and orthorhombic phase, respectively. (d) Order paramater plots of the maximums in the octahedral tilt distributions as a function of temperature. In the cubic to tetragonal transition the tils along x and y go to zero, while the tilts along z only go to zero during the tetragonal to cubic transition.

that was amenable to fast evaluations and suitable for Monte Carlo simulations. Interestingly the minimal model was able to reproduce the key features of the perovskite phase transitions, including the orthorhombic, tetragonal, to cubic phase sequence with the correct tilt sequence also observed. Moreover, the thermal ellipsoids qualitatively matched those observed in experiments. The fact that such a simple functional form of the pair energies is enough to reproduce the perovskite phase sequence demonstrates the importance of these particular pair energies.

Next, we parameterically showed the role of energy barrier differences on phase transition temperatures in $CsPbBr_3$. By varing a single ECI which corresponded to shifting the BrBr energy function to low q_0 the tetragonal phase was stabilized relative to the ϵ-phase. Interestingly small changes in the energy abrriers led to large changes in the transition temperatures observed in Monte Carlo simulations.

Lastly, the local structure due to octahedral tilting was investigated by collecting histograms of Euler angles over many Monte Carlo passes. The bimodal distribution of rotation angles coalesce into one peak upon a phase transition whereupon the mean tilt angle goes to zero. Within the cubic phase, all distributions of rotation angles are centered at zero but the distributions show large dispersion indicating large deviations from the high symmetry phase. There has been some debate as to the local structure of halide perovksite materials at high temperature, with a consensus that the material is not locally cubic. Our Monte Carlo experiments also suggest that the material is on average cubic, but large octahedral tilt modes are still present.

7.4 Conclusions

By reparameterizing a neural network model of the DFT potential energy surface we have constructed a minimal vibrational effective Hamiltonian that qualtiatively re-

produces the DFT energy surface near the ground state. Additionally, by using a simple polynomial reparameterization we overcome the traditional challenges with machine learning models that make them ill-suited for Monte Carlo simultions. Our Monte Carlo results show that simple polynomial models of cluster energies can reproduce the complex phase sequence of octahedral tilt modes in halide perovskites. Incorporating the tolerance factor perspective on perovskite tilts, we demonstrated that the octahedral tilt modes come about due to a minimum in the CsBr energy functional corresponding to shortened bond lenghts. Lastly, the local structure due to octahedral tilts showed that in the cubic phase, tilts average to zero but still show significant deviation from the cubic phase.

Chapter 8

Conclusion

The field of halide perovskite research has shown the potential of intense focus by many different communities from chemistry, to photo-physics to first-principles investigations. In only a short period of time, we have seen the efficiency of devices vastly improve, and some fundamental science has uncovered fascinating aspects of halide perovskite structural and electronic properties. In particular the coupling between structural degrees of freedom and the electronic properties is at the heart of revealing the basic properties of halide perovskites. This dissertation has taken a detailed investigation into the structural aspects of halide perovskites. First, the energy landscape of the methylammonium ion was mapped in Chapter 3 revealing that translations of the A-cation are an important degree of freedom besides orientational degrees of freedom. Although the A-cation does not contribute electronic states near the Fermi level, hydrogen-bonding between the NH_3 H atoms and the halide ions shows how the A-site cation can play a role in the structure of the octahedral sublattice, therefore affecting electronic properties.

Both hybrid perovskites and inorganic perovskites undergo structural phase transitions associated with octahedral tilting. In Chapter 4, we employed a group theoretical approach to identify primary displacement order parameters and secondary strain order

parameters associated with octahedral tilting in the perovskite crystal structure. Several results emerged from our comprehensive treatment of the structural degrees of freedom in inorganic halide perovskites. First, all 14 of the symmetry lowering tilt deformations reduce the energy from the high symmetry cubic phase inorganic halide perovskites. More importantly, the energy of the tilted variants correlates with the volume decrease from the high symmetry phase to the low symmetry phase, confirming a very general picture of tilting distortion in halide perovskites: as a system is cooled from the high symmetry cubic phase, the most energetically favorable transitions are those which most reduce the volume where the Pnma phase always exists as the most volume decreasing ground state. Additionally, a closer look at the structural distortions of the orthorhombic and tetragonal phases revealed that A-cation displacements are necessary to stabilize the experimentally observed phase.

Experimental reports of photo-induced halide segregation in halide perovskites motivated the ab initio determination of the temperature vs composition phase diagrams presented in Chapter 5. By parameterizing a cluster expansion model from DFT calculations for six different binary halide systems, we were able to investigate the finite temperature phase behavior halide perovskites from first principles. The point at which solid solutions were found to be stable correlated remarkably well with the volume difference between end-members giving a design principle for halide perovskite solid solutions: for a lower miscibility gap choose end members with similar volumes.

In Chapter 6, machine learning techniques along with basis functions of collective displacement modes were used to parameterize the DFT potential energy surface for the highly anharmonic $CsPbBr_3$ energy landscape. A detailed hyperparameter study showed how low order shallow neural net models serve as the most generalizable models while more complex models often overfit the DFT training data resulting in poor extrapolation. Interestingly, using a neural network with non-linear activation functions based upon

harmonic basis function inputs allowed full mapping of the anharmonic energy landscape.

Lastly in Chapter 7, we developed a simple, interpretable vibrational Hamiltonian based on simple pairwise and octahedral cluster interactions. Parameterizing the model with machine-learning techniques we constructed a vibrational model amenable to finite-temperature Monte Carlo simulations. The cubic-tetragonal-orthorhombic phase transitions were qualitatively reproduced using this model demonstrating that pairwise interactions are central to the physics of halide perovskite structural phase transitions. Furthermore, we showed the local structure of octahedral tilts evolves as a function of temperature. We show how the mean of rotation angle distributions tends to zero upon a phase transition, however the dispersion of the distribution increases revealing highly deformed local structure in the high temperature cubic phase.

This dissertation has explored many degrees of freedom present in the halide perovskite system including orientational degrees of freedom, displacement degrees of freedom, and configurational degrees of freedom, applying finite temperature statistical mechanics to study the phase behavior of halide perovskites due to each contribution to the free energy. With the recent development of the orientational cluster expansion, a natural progression of this work includes the parameterization of a rotational cluster expansion to study the finite temperature properties of molecular orientation predicted from first principles simulations. Moreover, due to the abstraction of the cluster expansion formalism, it is possible to construct coupled Hamiltonians, say between orientational degrees of freedom and vibrational degrees of freedom, by taking the tensor product between the site basis functions resulting in even more general models. In this vein, it is likely that developments will lead to fully generalized effective Hamiltonians that can handle rotational, vibrational, configurational and possibly electronic degrees of freedom in the near future. To the motivated researcher there is an abundance of opportunity for pushing the limits of DFT and effective Hamiltonians.

Bibliography

[1] A. Kojima, K. Teshima, Y. Shirai, and T. Miyasaka, J. Am. Chem. Soc. **131**, 6050 (2009).

[2] M. A. Green and A. Ho-Baillie, ACS Energy Letters **2**, 822 (2017).

[3] K. X. Steirer, P. Schulz, G. Teeter, V. Stevanovic, M. Yang, K. Zhu, and J. J. Berry, ACS Energy Letters **1**, 360 (2016).

[4] W.-J. Yin, T. Shi, and Y. Yan, Applied Physics Letters **104**, 063903 (2014).

[5] Q. Dong, Y. Fang, Y. Shao, P. Mulligan, J. Qiu, L. Cao, and J. Huang, Science **347**, 967 (2015).

[6] D. Shi, V. Adinolfi, R. Comin, M. Yuan, E. Alarousu, A. Buin, Y. Chen, S. Hoogland, A. Rothenberger, K. Katsiev, Y. Losovyj, X. Zhang, P. A. Dowben, O. F. Mohammed, E. H. Sargent, and O. M. Bakr, Science **347**, 519 (2015).

[7] M. Zhang, H. Yu, M. Lyu, Q. Wang, J.-H. Yun, and L. Wang, Chem. Commun. **50**, 11727 (2014).

[8] C. C. Stoumpos and M. G. Kanatzidis, Acc. Chem. Res. **48**, 2791 (2015).

[9] C. C. Stoumpos and M. G. Kanatzidis, Adv. Mater. **28**, 5778 (2016).

[10] C. Wehrenfennig, G. E. Eperon, M. B. Johnston, H. J. Snaith, and L. M. Herz, Adv. Mater. **26**, 1584 (2014).

[11] H. Oga, A. Saeki, Y. Ogomi, S. Hayase, and S. Seki, J. Am. Chem. Soc. **136**, 13818 (2014).

[12] H. Zhu, M. T. Trinh, J. Wang, Y. Fu, P. P. Joshi, K. Miyata, S. Jin, and X. Y. Zhu, Adv. Mater. **29**, 1603072 (2017).

[13] S. D. Stranks, S. D. Stranks, G. E. Eperon, G. Grancini, C. Menelaou, M. J. P. Alcocer, T. Leijtens, L. M. Herz, A. Petrozza, and H. J. Snaith, Science **342**, 341 (2014).

[14] L. M. Herz, Annu. Rev. Phys. Chem. **67**, 65 (2016).

[15] F. Zheng, L. Z. Tan, S. Liu, and A. M. Rappe, Nano Lett. **15**, 7794 (2015).

[16] T. Etienne, E. Mosconi, and F. De Angelis, J. Phys. Chem. Lett. **7**, 1638 (2016).

[17] C. Motta, F. El-Mellouhi, S. Kais, N. Tabet, F. Alharbi, and S. Sanvito, Nat. Commun. **6**, 7026 (2015).

[18] A. N. Beecher, O. E. Semonin, J. M. Skelton, J. M. Frost, M. W. Terban, H. Zhai, A. Alatas, J. S. Owen, A. Walsh, and S. J. L. Billinge, ACS Energy Lett. **1**, 880 (2016).

[19] P. Azarhoosh, S. McKechnie, J. M. Frost, A. Walsh, and M. Van Schilfgaarde, APL Mater. **4** (2016), 10.1063/1.4955028.

[20] D. Niesner, M. Wilhelm, I. Levchuk, A. Osvet, S. Shrestha, M. Batentschuk, C. Brabec, and T. Fauster, Phys. Rev. Lett. **117**, 126401 (2016).

[21] H. Zhu, K. Miyata, Y. Fu, J. Wang, P. P. Joshi, D. Niesner, K. W. Williams, S. Jin, and X.-Y. Zhu, Science **353**, 1409 (2016).

[22] X. Y. Zhu and V. Podzorov, J. Phys. Chem. Lett. **6**, 4758 (2015).

[23] C. Yi, J. Luo, S. Meloni, A. Boziki, N. Ashari-Astani, C. Gratzel, S. M. Zakeeruddin, U. Rothlisberger, and M. Gratzel, Energy Environ. Sci. **9**, 656 (2016).

[24] M. Saliba, T. Matsui, J.-Y. Seo, K. Domanski, J.-P. Correa-Baena, M. K. Nazeeruddin, S. M. Zakeeruddin, W. Tress, A. Abate, A. Hagfeldt, and M. Gratzel, Energy Environ. Sci. **9**, 1989 (2016).

[25] Z. Wang, Z. Shi, T. Li, Y. Chen, and W. Huang, Angew. Chem. Int. Ed **56**, 1190 (2017).

[26] R. G. Niemann, L. Gouda, J. Hu, S. Tirosh, R. Gottesman, P. J. Cameron, and A. Zaban, J. Mater. Chem. A **4**, 17819 (2016).

[27] W. Travis, E. N. K. Glover, H. Bronstein, D. O. Scanlon, and R. G. Palgrave, Chem. Sci. **7**, 4548 (2016).

[28] D. M. Jang, K. Park, D. H. Kim, J. Park, F. Shojaei, H. S. Kang, J.-P. Ahn, J. W. Lee, and J. K. Song, Nano Lett. **15**, 5191 (2015).

[29] Q. A. Akkerman, V. D'Innocenzo, S. Accornero, A. Scarpellini, A. Petrozza, M. Prato, and L. Manna, J. Am. Chem. Soc. **137**, 10276 (2015).

[30] J. H. Noh, S. H. Im, J. H. Heo, T. N. Mandal, and S. I. Seok, Nano Lett. **13**, 1764 (2013).

[31] L. Protesescu, S. Yakunin, M. I. Bodnarchuk, F. Krieg, R. Caputo, C. H. Hendon, R. X. Yang, A. Walsh, and M. V. Kovalenko, Nano Lett. **15**, 3692 (2015).

[32] T. Chen, B. J. Foley, B. Ipek, M. Tyagi, J. R. Copley, C. M. Brown, J. J. Choi, and S.-H. Lee, Phys. Chem. Chem. Phys. **17**, 31278 (2015).

[33] J. M. Frost, K. T. Butler, and A. Walsh, APL Mater. **2**, 081506 (2014).

[34] A. A. Bakulin, O. Selig, H. J. Bakker, Y. L. Rezus, C. Müller, T. Glaser, R. Lovrincic, Z. Sun, Z. Chen, A. Walsh, J. M. Frost, and T. L. C. Jansen, J. Phys. Chem. Lett. **6**, 3663 (2015).

[35] A. M. A. Leguy, J. M. Frost, A. P. McMahon, V. G. Sakai, W. Kochelmann, C. Law, X. Li, F. Foglia, A. Walsh, B. C. O'Regan, J. Nelson, J. T. Cabral, and P. R. F. Barnes, Nature Commun. **6**, 7124 (2015).

[36] D. H. Fabini, T. Hogan, H. A. Evans, C. C. Stoumpos, M. G. Kanatzidis, and R. Seshadri, J. Phys. Chem. Lett. **7**, 376 (2016).

[37] N. Onoda-Yamamuro, T. Matsuo, and H. Suga, J. Phys. Chem. Solids **53**, 935 (1992).

[38] L.-y. Huang and W. R. Lambrecht, Phys. Rev. B **88**, 165203 (2013).

[39] L. Y. Huang and W. R. L. Lambrecht, Phys. Rev. B **90**, 195201 (2014).

[40] Q. Lin, A. Armin, R. C. R. Nagiri, P. L. Burn, and P. Meredith, Nat. Photonics **9**, 106 (2014).

[41] M. H. Du, J. Mater. Chem. A **2**, 9091 (2014).

[42] D. H. Fabini, T. Hogan, H. A. Evans, C. C. Stoumpos, M. G. Kanatzidis, and R. Seshadri, J. Phys. Chem. Lett. **7**, 376 (2016).

[43] C. C. Stoumpos, C. D. Malliakas, and M. G. Kanatzidis, Inorg. Chem. **52**, 9019 (2013).

[44] L. Kubičár, V. Vretenár, and R. Yves, Solid State Phenom. **138**, 3 (2008).

[45] M. Rodová, J. Brožek, K. Knížek, and K. Nitsch, Journal of thermal analysis and calorimetry **71**, 667 (2003).

[46] M. Mori and H. Saito, J. Phys. C Solid State Phys. **19**, 2391 (1986).

[47] M. H. Kuok, E. L. Saw, and C. T. Yap, Phys. Status Solidi A **132**, K89 (1992).

[48] J.-C. Zheng, C. H. A. Huan, A. T. S. Wee, and M. H. Kuok, Surface and Interface Analysis **28**, 81 (1999).

[49] D. E. Scaife, P. F. Weller, and W. G. Fisher, J. Solid State Chem. **9**, 308 (1974).

[50] C. C. Stoumpos, C. D. Malliakas, and M. G. Kanatzidis, Inorg. Chem. **52**, 9019 (2013).

[51] R. M. Martin, *Electronic structure: basic theory and practical methods* (Cambridge university press, 2004).

[52] P. Hohenberg and W. Kohn, Phys. Rev. **136**, B864 (1964).

[53] W. Kohn and L. J. Sham, Phys. Rev. **140**, A1133 (1965).

[54] J. M. Sanchez, F. Ducastelle, and D. Gratias, Physica A: Statistical Mechanics and its Applications **128**, 334 (1984).

[55] J. Sanchez, Physical review B **48**, 14013 (1993).

[56] D. B. Laks, L. Ferreira, S. Froyen, and A. Zunger, Physical Review B **46**, 12587 (1992).

[57] J. Connolly and A. Williams, Physical Review B **27**, 5169 (1983).

[58] D. De Fontaine, in *Solid state physics*, Vol. 47 (Elsevier, 1994) pp. 33–176.

[59] A. Van De Walle and G. Ceder, Reviews of Modern Physics **74**, 11 (2002).

[60] G. Garbulsky and G. Ceder, Physical Review B **49**, 6327 (1994).

[61] A. Franceschetti, S. Dudiy, S. Barabash, A. Zunger, J. Xu, and M. Van Schilfgaarde, Physical review letters **97**, 047202 (2006).

[62] A. Franceschetti and A. Zunger, Nature **402**, 60 (1999).

[63] A. van de Walle, Nature materials **7**, 455 (2008).

[64] J. C. Thomas and A. Van der Ven, Phys. Rev. B **88**, 214111 (2013).

[65] J. C. Thomas, J. S. Bechtel, and A. Van der Ven, Phys. Rev. B **98**, 094105 (2018).

[66] G. L. Hart, V. Blum, M. J. Walorski, and A. Zunger, Nature materials **4**, 391 (2005).

[67] L. J. Nelson, G. L. Hart, F. Zhou, V. Ozoliņš, *et al.*, Physical Review B **87**, 035125 (2013).

[68] L. J. Nelson, V. Ozoliņš, C. S. Reese, F. Zhou, and G. L. Hart, Physical Review B **88**, 155105 (2013).

[69] W. HASTINGS, Biometrika **57**, 97 (1970).

[70] N. Metropolis, A. W. Rosenbluth, M. N. Rosenbluth, A. H. Teller, and E. Teller, The journal of chemical physics **21**, 1087 (1953).

[71] T. B. Blank, S. D. Brown, A. W. Calhoun, and D. J. Doren, The Journal of chemical physics **103**, 4129 (1995).

[72] F. V. Prudente and J. S. Neto, Chemical physics letters **287**, 585 (1998).

[73] J. Behler and M. Parrinello, Physical review letters **98**, 146401 (2007).

[74] J. Behler, Physical Chemistry Chemical Physics **13**, 17930 (2011).

[75] J. Behler, International Journal of Quantum Chemistry **115**, 1032 (2015).

[76] J. S. Bechtel, R. Seshadri, and A. Van der Ven, The Journal of Physical Chemistry C **120**, 12403 (2016).

[77] M. M. Lee, J. Teuscher, T. Miyasaka, T. N. Murakami, and H. J. Snaith, Science **338**, 643 (2012).

[78] H. Zhou, Q. Chen, G. Li, S. Luo, T.-b. Song, H.-S. Duan, Z. Hong, J. You, Y. Liu, and Y. Yang, Science **345**, 542 (2014).

[79] N. J. Jeon, J. H. Noh, Y. C. Kim, W. S. Yang, S. Ryu, and S. I. Seok, Nature Mater. **13**, 897 (2014).

[80] W. S. Yang, J. H. Noh, N. J. Jeon, Y. C. Kim, S. Ryu, J. Seo, and S. I. Seok, Science **348**, 1234 (2015).

[81] S. D. Stranks, G. E. Eperon, G. Grancini, C. Menelaou, M. J. P. Alcocer, T. Leijtens, L. M. Herz, A. Petrozza, and H. J. Snaith, Science **342**, 341 (2013).

[82] G. Xing, N. Mathews, S. Sun, S. S. Lim, Y. M. Lam, M. Grätzel, S. Mhaisalkar, and T. C. Sum, Science **342**, 344 (2013).

[83] S. De Wolf, J. Holovsky, S. J. Moon, P. Löper, B. Niesen, M. Ledinsky, F. J. Haug, J. H. Yum, and C. Ballif, J. Phys. Chem. Lett. **5**, 1035 (2014).

[84] H.-S. Kim, C.-R. Lee, J.-H. Im, K.-B. Lee, T. Moehl, A. Marchioro, S.-J. Moon, R. Humphry-Baker, J.-H. Yum, J. E. Moser, M. Grätzel, and N.-G. Park, Sci. Rep. **2**, 591 (2012).

[85] Y. Kawamura, H. Mashiyama, and K. Hasebe, J. Phys. Soc. Japan **71**, 1694 (2002).

[86] E. Mosconi, C. Quarti, T. Ivanovska, G. Ruani, and F. De Angelis, Phys. Chem. Chem. Phys. **16**, 16137 (2014).

[87] S. A. Kulkarni, T. Baikie, P. P. Boix, N. Yantara, N. Mathews, and S. Mhaisalkar, J. Mater. Chem. A **2**, 9221 (2014).

[88] A. Amat, E. Mosconi, E. Ronca, C. Quarti, P. Umari, M. K. Nazeeruddin, M. Grätzel, and F. De Angelis, Nano Lett. **14**, 3608 (2014).

[89] F. Brivio, K. T. Butler, A. Walsh, and M. Van Schilfgaarde, Phys. Rev. B **89**, 155204 (2014).

[90] P. Umari, E. Mosconi, and F. De Angelis, Sci. Rep. **4**, 4467 (2014).

[91] J. G. Labram, D. H. Fabini, E. E. Perry, A. J. Lehner, H. Wang, A. M. Glaudell, G. Wu, H. Evans, D. Buck, R. Cotta, L. Echegoyen, F. Wudl, R. Seshadri, and M. L. Chabinyc, J. Phys. Chem. Lett. **6**, 3565 (2015).

[92] A. Poglitsch and D. Weber, J. Chem. Phys. **87**, 6373 (1987).

[93] A. M. Glazer, Acta Crystallogr. Sect. B Struct. Crystallogr. Cryst. Chem. **28**, 3384 (1972).

[94] T. Baikie, Y. Fang, J. M. Kadro, M. Schreyer, F. Wei, S. G. Mhaisalkar, M. Gratzel, and T. J. White, J. Mater. Chem. A **1**, 5628 (2013).

[95] T. Baikie, N. S. Barrow, Y. Fang, P. J. Keenan, P. R. Slater, R. O. Piltz, M. Gutmann, S. G. Mhaisalkar, and T. J. White, J. Mater. Chem. A **3**, 9298 (2015).

[96] M. T. Weller, O. J. Weber, P. F. Henry, M. Di Pumpo, and T. C. Hansen, Chem. Commun. **51**, 4180 (2015).

[97] J. Even, M. Carignano, and C. Katan, Nanoscale **8**, 6222 (2015).

[98] A. Mattoni, A. Filippetti, M. I. Saba, and P. Delugas, J. Phys. Chem. C **119**, 17421 (2015).

[99] M. A. Carignano, A. Kachmar, and J. Hutter, J. Phys. Chem. C **119**, 8991 (2015).

[100] J.-H. Lee, N. C. Bristowe, P. D. Bristowe, and A. K. Cheetham, Chem. Commun. **51**, 6434 (2015).

[101] J. H. Lee, J.-H. Lee, E.-H. Kong, and H. M. Jang, Sci. Rep. **6**, 21687 (2016).

[102] F. Brivio, A. B. Walker, and A. Walsh, APL Mater. **1**, 042111 (2013).

[103] K. P. Ong, T. W. Goh, Q. Xu, and A. Huan, J. Phys. Chem. A **119**, 11033 (2015).

[104] G. Kresse and J. Furthmüller, Phys. Rev. B **54**, 11169 (1996).

[105] G. Kresse, Phys. Rev. B **59**, 1758 (1999).

[106] P. E. Blöchl, Phys. Rev. B **50**, 17953 (1994).

[107] J. P. Perdew, K. Burke, and M. Ernzerhof, Phys. Rev. Lett. **77**, 3865 (1996).

[108] S. Grimme, J. Antony, S. Ehrlich, and H. Krieg, J. Chem. Phys. **132**, 154104 (2010).

[109] K. Momma and F. Izumi, J. Appl. Crystallogr. **41**, 653 (2008).

[110] T. Umebayashi, K. Asai, T. Kondo, and A. Nakao, Phys. Rev. B **67**, 155405 (2003).

[111] J. Brgoch, A. J. Lehner, M. L. Chabinyc, and R. Seshadri, J. Phys. Chem. C **18**, 27721 (2014).

[112] U. Waghmare, N. Spaldin, H. Kandpal, and R. Seshadri, Phys. Rev. B **67**, 125111 (2003).

[113] Y. Kutes, L. Ye, Y. Zhou, S. Pang, B. D. Huey, and N. P. Padture, J. Phys. Chem. Lett. **5**, 3335 (2014).

[114] H.-W. Chen, N. Sakai, M. Ikegami, and T. Miyasaka, J. Phys. Chem. Lett. **6**, 164 (2014).

[115] B. Chen, J. Shi, X. Zheng, Y. Zhou, K. Zhu, and S. Priya, J. Mater. Chem. A **3**, 7699 (2015).

[116] J. Beilsten-Edmands, G. E. Eperon, R. D. Johnson, H. J. Snaith, and P. G. Radaelli, Appl. Phys. Lett. **106**, 173502 (2015).

[117] M. Coll, A. Gomez, E. Mas-Marza, O. Almora, G. Garcia-Belmonte, M. Campoy-Quiles, and J. Bisquert, J. Phys. Chem. Lett. **6**, 1408 (2015).

[118] K. M. Rabe and U. V. Waghmare, Phys. Rev. B **52**, 13236 (1995).

[119] W. Zhong, D. Vanderbilt, and K. M. Rabe, Phys. Rev. B **52**, 6301 (1995).

[120] T. Mueller and G. Ceder, Phys. Rev. B **74**, 134104 (2006).

[121] R. Drautz and M. Fähnle, Phys. Rev. B **69**, 104404 (2004).

[122] J. Bhattacharya and A. Van der Ven, Acta Mater. **56**, 4226 (2008).

[123] Q. Chen, N. D. Marco, Y. M. Yang, T.-B. Song, C.-C. Chen, H. Zhao, Z. Hong, H. Zhou, and Y. Yang, Nano Today **10**, 355 (2015).

[124] I. P. Swainson, C. Stock, S. F. Parker, L. Van Eijck, M. Russina, and J. W. Taylor, Phys. Rev. B **92**, 100303 (2015).

[125] A. Marronnier, H. Lee, B. Geffroy, J. Even, Y. Bonnassieux, and G. Roma, J. Phys. Chem. Lett. **8**, 2659 (2017).

[126] M. Sakata, J. Harada, M. J. Cooper, and K. D. Rouse, Acta Crystallogr. Sect. A **36**, 7 (1980).

[127] R. X. Yang, J. M. Skelton, E. L. da Silva, J. M. Frost, and A. Walsh, J. Phys. Chem. Lett. **8**, 4720 (2017).

[128] O. Yaffe, Y. Guo, L. Z. Tan, D. A. Egger, T. Hull, C. C. Stoumpos, F. Zheng, T. F. Heinz, L. Kronik, M. G. Kanatzidis, J. S. Owen, A. M. Rappe, M. A. Pimenta, and L. E. Brus, Phys. Rev. Lett. **118**, 136001 (2017).

[129] G. Laurita, D. H. Fabini, C. C. Stoumpos, M. G. Kanatzidis, and R. Seshadri, Chem. Sci. **8**, 5628 (2017).

[130] V. M. Goldschmidt, Naturwissenschaften **14**, 477 (1926).

[131] P. Whitfield, N. Herron, W. Guise, K. Page, Y. Cheng, I. Milas, and M. Crawford, Scientific Reports **6**, 35685 (2016).

[132] K. Yamada, S. Funabiki, H. Horimoto, T. Matsui, T. Okuda, and S. Ichiba, Chem. Lett. , 801 (1991).

[133] J. Kang and L.-W. Wang, J. Phys. Chem. Lett. **8**, 489 (2017).

[134] E. L. da Silva, J. M. Skelton, S. C. Parker, and A. Walsh, Phys. Rev. B **91**, 144107 (2015).

[135] I. Chung, J.-H. Song, J. Im, J. Androulakis, C. D. Malliakas, H. Li, A. J. Freeman, J. T. Kenney, and M. G. Kanatzidis, JACS **134**, 8579 (2012).

[136] C. K. Moeller, Nature **182**, 1436 (1958).

[137] D. P. McMeekin, G. Sadoughi, W. Rehman, G. E. Eperon, M. Saliba, M. T. Hörantner, A. Haghighirad, N. Sakai, L. Korte, B. Rech, M. B. Johnston, L. M. Herz, and H. J. Snaith, Science **351**, 151 (2016).

[138] H. Choi, J. Jeong, H.-B. Kim, S. Kim, B. Walker, G.-H. Kim, and J. Y. Kim, Nano Energy **7**, 80 (2014).

[139] Z. Li, M. Yang, J.-S. Park, S.-H. Wei, J. J. Berry, and K. Zhu, Chem. Mater. **28**, 284 (2016).

[140] J. C. Thomas and A. Van der Ven, Phys. Rev. B **96**, 134121 (2017).

[141] C. J. Howard and H. T. Stokes, Acta Crystallogr. Sect. B Struct. Sci. **54**, 782 (1998).

[142] J. C. Thomas and A. Van der Ven, J. Mech. Phys. Solids **107**, 76 (2017).

[143] H. T. Stokes and D. M. Hatch, Phase Transitions **34**, 53 (1991).

[144] R. D. Shannon, Acta Crystallogr. Sect. A **32**, 751 (1976).

[145] J. Young and J. M. Rondinelli, J. Phys. Chem. Lett. **7**, 918 (2016).

[146] S. Meloni, G. Palermo, N. Ashari-Astani, M. Gratzel, and U. Rothlisberger, J. Mater. Chem. A **4**, 15997 (2016).

[147] P. Garcia-Fernandez, J. Aramburu, M. Barriuso, and M. Moreno, J. Phys. Chem. Lett. **1**, 647 (2010).

[148] P. M. Woodward, Acta Crystallogr. Sect. B Struct. Sci. **53**, 32 (1997).

[149] A. Cammarata and J. M. Rondinelli, J. Chem. Phys. **141** (2014).

[150] A. Ferretti, D. Rogers, and J. Goodenough, J. Phys. Chem. Solids **26**, 2007 (1965).

[151] F. Bertolotti, L. Protesescu, M. V. Kovalenko, S. Yakunin, A. Cervellino, S. J. L. Billinge, M. W. Terban, J. S. Pedersen, N. Masciocchi, and A. Guagliardi, ACS Nano **11**, 3819 (2017).

[152] W. Zhang, G. E. Eperon, and H. J. Snaith, Nature Energy **1**, 16048 (2016).

[153] A. Buin, R. Comin, J. Xu, A. H. Ip, and E. H. Sargent, Chem. Mater. **27**, 4405 (2015).

[154] M.-H. Du, J. Phys. Chem. Lett. **6**, 1461 (2015).

[155] M. L. Agiorgousis, Y.-Y. Sun, H. Zeng, and S. Zhang, J. Am. Chem. Soc. **136**, 14570 (2014).

[156] Z.-K. Tan, R. S. Moghaddam, M. L. Lai, P. Docampo, R. Higler, F. Deschler, M. Price, A. Sadhanala, L. M. Pazos, D. Credgington, *et al.*, Nature Nanotechnology **9**, 687 (2014).

[157] R. K. Misra, S. Aharon, B. Li, D. Mogilyansky, I. Visoly-Fisher, L. Etgar, and E. A. Katz, J. Phys. Chem. Lett. **6**, 326 (2015).

[158] E. T. Hoke, D. J. Slotcavage, E. R. Dohner, A. R. Bowring, H. I. Karunadasa, and M. D. McGehee, Chem. Sci. **6**, 613 (2015).

[159] D. J. Slotcavage, H. I. Karunadasa, and M. D. McGehee, ACS Energy Letters **1**, 1199 (2016).

[160] R. E. Beal, D. J. Slotcavage, T. Leijtens, A. R. Bowring, R. A. Belisle, W. H. Nguyen, G. F. Burkhard, E. T. Hoke, and M. D. McGehee, J. Phys. Chem. Lett. **7**, 746 (2016).

[161] E. L. Unger, L. Kegelmann, K. Suchan, D. Sorell, L. Korte, and S. Albrecht, J. Mater. Chem. A **5**, 11401 (2017).

[162] S. J. Yoon, S. Draguta, J. S. Manser, O. Sharia, W. F. Schneider, M. Kuno, and P. V. Kamat, ACS Energy Letters **1**, 290 (2016).

[163] C. G. Bischak, C. L. Hetherington, H. Wu, S. Aloni, D. F. Ogletree, D. T. Limmer, and N. S. Ginsberg, Nano Letters **17**, 1028 (2017).

[164] F. Brivio, C. Caetano, and A. Walsh, J. Phys. Chem. Lett. **7**, 1083 (2016).

[165] W.-J. Yin, Y. Yan, and S.-H. Wei, J. Phys. Chem. Lett. **5**, 3625 (2014).

[166] J. P. Perdew, A. Ruzsinszky, G. I. Csonka, O. A. Vydrov, G. E. Scuseria, L. A. Constantin, X. Zhou, and K. Burke, Physical Review Letters **100**, 136406 (2008).

[167] A. Van der Ven, J. Thomas, Q. Xu, and J. Bhattacharya, Mathematics and computers in simulation **80**, 1393 (2010).

[168] B. Puchala and A. Van der Ven, Physical Review B **88**, 094108 (2013).

[169] J. S. Bechtel and A. Van der Ven, Phys. Rev. Materials **2**, 025401 (2018).

[170] X. Yang, X. Yan, W. Wang, X. Zhu, H. Li, W. Ma, and C. Sheng, Organic Electronics **34**, 79 (2016).

[171] G. Nedelcu, L. Protesescu, S. Yakunin, M. I. Bodnarchuk, M. J. Grotevent, and M. V. Kovalenko, Nano Letters **15**, 5635 (2015).

[172] S. Draguta, O. Sharia, S. J. Yoon, M. C. Brennan, Y. V. Morozov, J. M. Manser, P. V. Kamat, W. F. Schneider, and M. Kuno, Nature communications **8**, 200 (2017).

[173] N. Onoda-Yamamuro, T. Matsuo, and H. Suga, Journal of Physics and Chemistry of Solids **51**, 1383 (1990).

[174] I. Swainson, R. Hammond, C. Soulliere, O. Knop, and W. Massa, Journal of Solid State Chemistry **176**, 97 (2003).

[175] M. C. Brennan, S. Draguta, P. V. Kamat, and M. Kuno, ACS Energy Letters **3**, 204 (2018).

[176] R. J. Sutton, G. E. Eperon, L. Miranda, E. S. Parrott, B. A. Kamino, J. B. Patel, M. T. Hörantner, M. B. Johnston, A. A. Haghighirad, D. T. Moore, *et al.*, Advanced Energy Materials **6** (2016).

[177] D. Vanderbilt and W. Zhong, Ferroelectrics **206**, 181 (1998), https://doi.org/10.1080/00150199808009158 .

[178] X. Ai, Y. Chen, and C. a. Marianetti, Phys. Rev. B **90**, 014308 (2014).

[179] N. Artrith and A. Urban, Comput. Mater. Sci. **114**, 135 (2016).

[180] N. Artrith, A. Urban, and G. Ceder, Phys. Rev. B **96**, 1 (2017), arXiv:1706.06293 .

[181] V. L. Deringer and G. Csányi, Phys. Rev. B **95**, 1 (2017), arXiv:1611.03277 .

[182] A. Grisafi, D. M. Wilkins, G. Csányi, and M. Ceriotti, Phys. Rev. Lett. **120**, 036002 (2018).

[183] M. Rupp, (2018), arXiv:arXiv:1704.06439v3 .

[184] M. Rupp, Int. J. Quantum Chem. **115**, 1058 (2015), arXiv:1307.2918 .

[185] M. Rupp, A. Tkatchenko, K.-R. Müller, and O. A. von Lilienfeld, Phys. Rev. Lett. **108**, 058301 (2012).

[186] A. P. Thompson, L. P. Swiler, C. R. Trott, S. M. Foiles, and G. J. Tucker, J. Comput. Phys. **285**, 316 (2015).

[187] A. P. Bartok and G. Csányi, Int. J. Quantum Chem. **115**, 1051 (2015), arXiv:1502.01366 .

[188] A. P. Bartok, M. C. Payne, R. Kondor, and G. Csanyi, Phys. Rev. Lett. **104**, 1 (2010), arXiv:0910.1019 .

[189] D. Dragoni, T. D. Daff, G. Csányi, and N. Marzari, Phys. Rev. Materials **2**, 013808 (2018).

[190] C. M. Handley and J. Behler, Eur. Phys. J. B **87** (2014), 10.1140/epjb/e2014-50070-0.

[191] A. V. Shapeev, Multiscale Model. Simul. **14**, 1153 (2016).

[192] B. Fultz, Progress in Materials Science **55**, 247 (2010).

[193] A. Togo and I. Tanaka, Scripta Materialia **108**, 1 (2015).

[194] O. Sugino and R. Car, Phys. Rev. Lett. **74**, 1823 (1995).

[195] X. Wang, S. Scandolo, and R. Car, Phys. Rev. Lett. **95**, 185701 (2005).

[196] M. Kaczmarski, O. N. Bedoya-Martínez, and E. R. Hernández, Phys. Rev. Lett. **94**, 095701 (2005).

[197] M. A. Carignano, S. A. Aravindh, I. S. Roqan, J. Even, and C. Katan, The Journal of Physical Chemistry C **121**, 20729 (2017), https://doi.org/10.1021/acs.jpcc.7b08220 .

[198] K. M. Rabe and J. D. Joannopoulos, Phys. Rev. Lett. **59**, 570 (1987).

[199] K. M. Rabe and U. V. Waghmare, Ferroelectrics **136**, 147 (1992).

[200] W. Zhong, D. Vanderbilt, and K. M. Rabe, Phys. Rev. Lett. **73**, 1861 (1994).

[201] K. Rabe and U. Waghmare, Journal of Physics and Chemistry of Solids **57**, 1397 (1996), proceeding of the 3rd Williamsburg Workshop on Fundamental Experiments on Ferroelectrics.

[202] K. M. Rabe and U. V. Waghmare, Phys. Rev. B **52**, 13236 (1995).

[203] W. Zhong, D. Vanderbilt, and K. M. Rabe, Phys. Rev. B **52**, 6301 (1995).

[204] K. M. Rabe and W. U. V., Philosophical Transactions of the Royal Society of London A: Mathematical, Physical and Engineering Sciences **354**, 2897 (1996), http://rsta.royalsocietypublishing.org/content/354/1720/2897.full.pdf .

[205] U. V. Waghmare and K. M. Rabe, Phys. Rev. B **55**, 6161 (1997).

[206] E. Cockayne and K. M. Rabe, Phys. Rev. B **56**, 7947 (1997).

[207] U. V. Waghmare and K. M. Rabe, Ferroelectrics **194**, 135 (1997), https://doi.org/10.1080/00150199708016088 .

[208] K. M. Rabe and U. V. Waghmare, Ferroelectrics **194**, 119 (1997).